THE STARSPOTS AND MAGNETIC FIELDS OF YOUNG LATE-F STARS

A Thesis submitted by

James Edward Hughes

B.S. Electrical Engineering
Master of Astronomy

For the Award of
Doctor of Philosophy

2025

ABSTRACT

Observations of the magnetic activity of young solar-type stars offer insights into the early history of our Sun, its dynamo activity and planetary impacts. The warmest of solar-type stars, of F spectral type, have been shown to represent a transition from dynamo driven cool stars to fossil field dominated hot stars due to their thin convective zones, however, there are few detailed observations of the surface magnetic fields and cycles of these stars. This study thus presents multiple-epoch star spot and surface magnetic field maps of three young late-F solar-type stars, namely VXR 77A (V380 Vel, F8V, ~27 Myr), HD 43989 (V1358 Ori, F9V, ~26 Myr) and HIP 71933 (HD 128181, F8V, ~15 Myr). Those images were produced using the technique of Doppler and Zeeman-Doppler Imaging using spectroscopic and spectropolarimetric data, and derived from observations made across fourteen different epochs and multiple telescopes between 2003 and 2019. The resulting star spot brightness maps and the implied underlying dynamos for two of the stars (HD 43989 and VXR 77A) are consistent with those of other solar-type stars including polar spots, but there is a persistent lack of a polar spot on the third star, HIP 71933. Differential rotation measurements performed using these images for all three stars, were found to be slightly higher than that for young G-type stars, a stellar mass dependence consistent with dynamo theory and previous observations. However, in terms of the appearance and temporal evolution of the magnetic fields observed for two of the stars, HD 43989 shows complex magnetic fields apparently evolving over a timescale of two years, but in contrast, HIP 71933 shows a more stable magnetic field configuration, with a dominant and apparently unchanging poloidal field topology over a similar timescale, that warrants further investigation to look for any potential evolution. The radial velocities measured for two of the stars (VXR 77A and HIP 71933) indicate the possibility of a binary, but this is not expected to affect the star spot and magnetic fields results due to the wide separation of any companion, if it exists. In overall terms, this study provides evidence for magnetic dynamos in warm young solar-type showing similarities to those of other young solar-type stars, but with some unusual but not unique features on HIP 71933.

Certification of Thesis

I, Jim Hughes, declare that the PhD Thesis entitled *The Starspots and Magnetic Fields of Young Late-F Stars* is not more than 100,000 words in length including quotes and exclusive of tables, figures, appendices, bibliography, references, and footnotes. The thesis contains no material that has been submitted previously, in whole or in part, for the award of any other academic degree or diploma. Except where otherwise indicated, this thesis is my own work.

Endorsed by:

Associate Professor Stephen Marsden
Principal Supervisor

Professor Brad Carter
Associate Supervisor

Student and supervisors' signatures of endorsement are held at the University.

Acknowledgments

In addition to my supervisors, Dr. Stephan Marsden, and Dr. Brad Carter, I would like to acknowledge the nation of Australia; for giving me the opportunity to meet numerous Australian scientists and finally dispense with the ridiculous stereotypes we Americans have of Australians, for the efforts Australian universities are making to provide advanced online scientific training, and for the concept of open skies embraced by the Australian community of astronomers. G'day mate.

Contents

List of Tables

List of Figures

Acronyms

AAO	Anglo-Australian Observatory
AAT	Anglo-Australian Telescope
CFHT	Canada France Hawaii Telescope
DR	Differential Rotation
EWR	Equivalent Width Ratio
ESpRIT	Echelle Spectra Reduction and Interactive Tool
FEAT	Flux Emergence and Transport Simulation
FIRS	Facility InfraRed Spectropolarimeter
FITS	Flexible Image Transport System
FORTRAN	Formula Translator
GONG	Global Oscillations Network Group
GPR	Gaussian Process Regression
HARPSpol	High Accuracy Radial Velocity Planet Searcher with Polarimeter
HR	Hertzsprung-Russell (Diagram)
LBT	Large Binocular Telescope
LCF	Light Curve File
LDR	Line Depth Ratio
LRIS	Low Resolution Imaging Spectropolarimeter
LSD	Least Squares Deconvolution
MAST	Mikulski Archive Space Telescopes
MHD	Magnetohydrodynamic
MRI	Magneto-Rotational Instability

MS	Main Sequence
NASA	National Aeronautics and Space Administration
NSSL	Near Surface Shear Layer
PEPSI	Postham Echelle Polarimetric and Spectroscopic Instrument
RV	Radial Velocity
SB	Spectroscopic Binary
SBORBITCAT	Spectroscopic Binary Orbits Ninth Catalog
SOHO-SOI	Solar Heliospheric Observer Solar Oscillations Investigation
SIMBAD	Set of Identifications, Measurements and Bibliography for Astronomical Data
SOLIS	Synoptic Long Term Investigations of the Sun
SPIRou	Spectropolarimétre Infrarouge
STSCI	Space Telescope Science Institute
TBL	Télescope Bernard Lyot
TESS	Transiting Exoplanet Survey Satellite
TIC	TESS Identification Catalog
THEMIS	Téléscope Heliographique pur l’Étude du Magnetisme et des Instabilités Solaries spectropolarimeter
TIP II	Tenerife Infrared Polarimeter
TSSC	NASA TESS Science Support Center
TTS	T Tauri Stars
UCLES	University College London Echelle Spectrograph
ZAMS	Zero Age Main Sequence

1 INTRODUCTION

The magnetic field of the Sun has a direct effect on the magnetosphere and atmosphere of the Earth as well as likely its biosphere (Babcock, 1961; Glassmeier et al., 2009; Charbonneau, 2014; Ragulskaya, 2018; Perryman, 2018). More broadly, the area of a star's habitable zone is affected by the star's temperature, as well as its magnetic field, activity and stellar wind (Rósen, 2016). Therefore, studies of the magnetic fields of young and more mature age solar-type stars in our Galaxy can support efforts to better understand stellar evolution, our Sun's past, present and future, and the resulting impacts on the planet.

1.1 The Internal Structure of the Sun

Astronomers determine the internal structure of stars and planets by making theoretical predictions as to the physics of hot ionized gases. For this purpose spectroscopy has been utilized since the 19th century to attempt to determine the chemical composition of the Sun and other stars. Using this method, the discovery of hydrogen as the principal constituent element in the Sun was first reported by Cecilia Payne in 1925 in her PhD thesis (Payne, 1925), under some resistance from the predominantly male astronomers of the time (Perkowitz, 2022). This discovery supported an earlier claim by Arthur Eddington that energy from the Sun was produced by the fusion of hydrogen into helium (Eddintgon, 1920), with further explanation of this process given by Hans Bethe in 1939 (Bethe, 1939). Later evidence from the detection of neutrinos coming from the Sun as a result of the fusion process has supported this assertion (Holmgren & Davis, 1959; Bahcall & Davis, 2000; Haxton, 2008).

In the 1960s and 1970s astronomers realized that more detail about the interior of the Sun could be obtained by observing oscillations on the Sun's surface, in a manner similar to that used by geologists to determine the internal structure of the Earth by analysing seismic waves (Leighton et al., 1961; Ulrich, 1970). This process, referred to as helioseismology, has been used by the Solar Heliospheric Observer Solar Oscillations Investigation (SOHO-SOI) satellite (NASA, 2020a) and the Global Oscillation Network Group (GONG) to help understand the internal structure of our Sun. GONG utilizes six telescopes distributed around the Earth so that the Sun can be observed continuously (Gough et al., 1996; GONG, 2023). Based upon all of these methods and resources, a picture of the interior of the Sun has emerged as shown in Figure 1.1.1.

The core of the Sun lies in its center out to a distance of approximately 150,000 km. This is where the pressure and gravity of the Sun have compressed the hydrogen to where it is fusing into helium, occurring at temperatures of approximately 15 million K at the center. Here the process of fusion is converting four hydrogen atoms into a single helium atom with a gamma ray photon and a neutrino emitted as leftovers. Extending another 300,000 km is the radiative zone, where photons generated in the core by fusion can take tens of thousands of years to reach the next layer because of collisions within this zone. The temperatures here are 7 million K near the core to about 2 million K at the outer edge. The next region is the convection zone where the energy in the core is transported to the Sun's surface via convection. The temperature range here is from approximately 2 million K at a temperature of approximately 5800 K at the Sun's surface, or photosphere. The Sun's convection zone makes up approximately 26% of the solar radius. The photosphere is where the activity that creates sunspots, flares and prominences are seen. The photosphere, the chromosphere and the corona then make up what are referred to as the atmosphere of the Sun. Above the

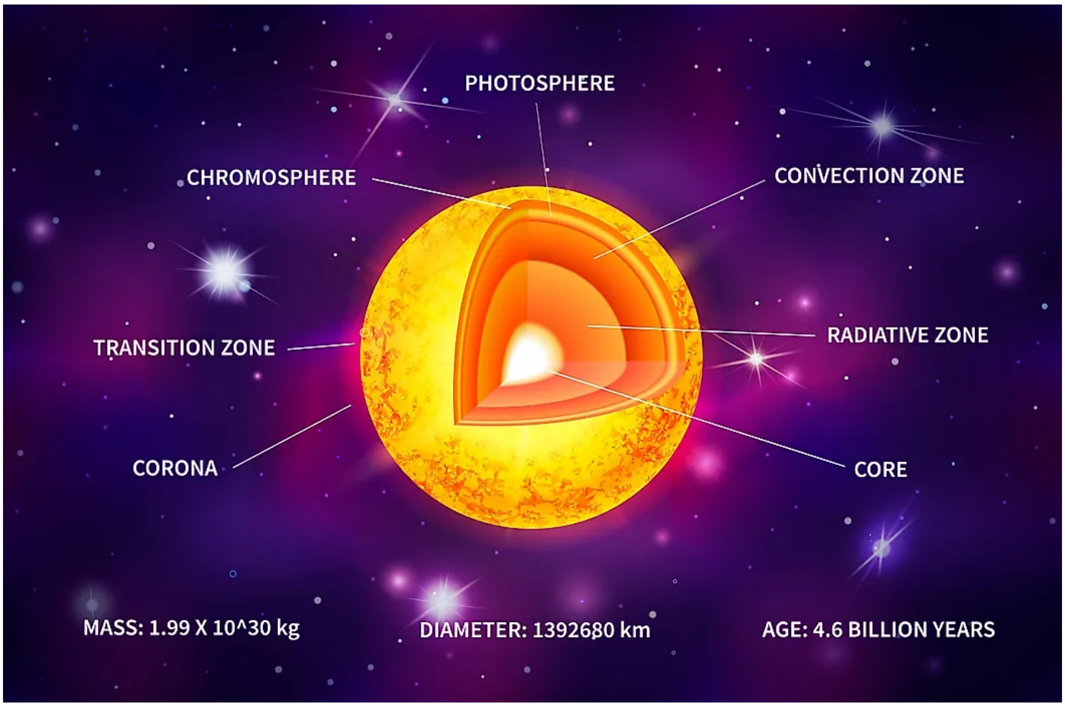

Figure 1.1.1: Interior of the Sun (WorldAtlas, 2020).

photosphere the temperatures increase from 4000 K to 8000 K in the chromosphere and up to 1 million K at the outer range of the corona, temperatures much higher than the Sun's photosphere (Erdélyi & Ballai, 2007; NASA, 2012, 2013a,b).

The study of rapid fluctuations of light on nearby stars is called asteroseismology, similar to the measurement of oscillations on the Sun's surface. This process has been successfully used to measure physical properties of other solar-type stars (Bazot et al., 2018; Bhalotia et al., Bhalotia et al.; Li et al., 2024). This data has added to the hypothesis that the interiors of other solar-type stars should be at least similar to the Sun.

1.2 Sunspots

Sunspots can be seen with the naked eye, and were first recorded by Chinese astronomers in ancient times (Temple, 1988). Although many history books credit Galileo with the first observations of sunspots with a telescope, there is evidence that Thomas Harriot recorded their existence ahead of Galileo from his notebooks that have survived (NCAR, 2023).

Sunspots are seen to appear in cyclic patterns of approximately 11 years each, with the spots appearing at about 30°above and below the solar equator and slowly emerging through the cycle further toward the equator. The solar minimum is when the sunspots are congregated at or near the equator. At the end of each 11 year cycle, the Sun's magnetic field reverses its polarity so that we have an approximately 22 year solar cycle. The sunspots often appear in groups and we know today that sunspots are low temperature regions in the Sun's photosphere making them appear dark in contrast to the bright surface of the Sun. Magnetic flux lines or "loops" push through the photosphere of the Sun, supressing convection, with a north polarity at one end and a south polarity at the other. For this reason, sunspots often appear in pairs, with opposite polarity, causing the light emitted in those regions to have

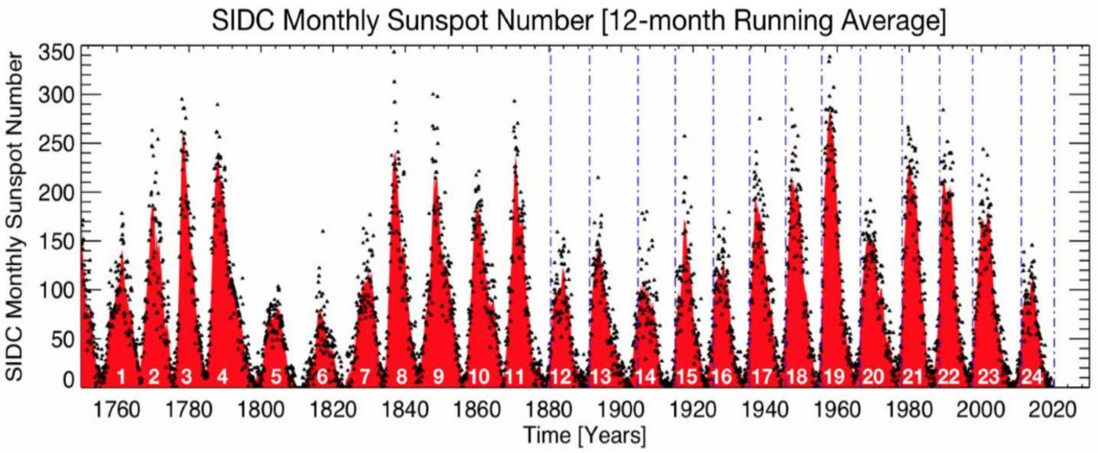

Figure 1.2.1: 11 year sunspot cycle showing peak values for sunspot numbers at the top of each cycle.

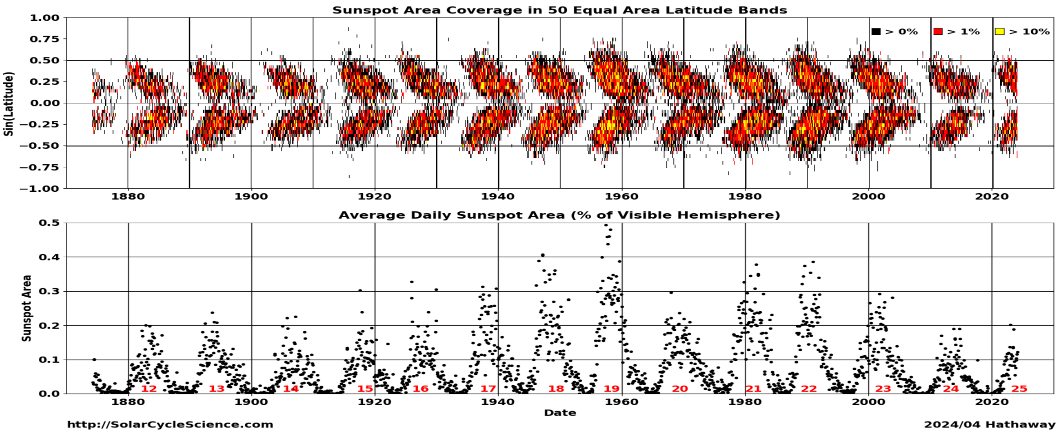

Figure 1.2.2: Sunspot butterfly diagram showing the location of the sunspots on the Sun's surface throughout the 11 year cycles (Hathaway, 2024).

opposite polarity (Babcock, 1961).

Solar cycles have been observed since 1755 and as of the writing of this thesis, 24 cycles have been recorded. We are currently in the midst of cycle 25. These cycles are tracked by the National Weather Service in the United States (NWS, 2024), however the World Data Center provides the official count of sunspots using long-term solar observations at the Royal Observatory in Belgium (NOAA, 2024).

Figure 1.2.1 is a graph of the number of sunspots observed on the Sun from 1750 until 2020 and shows the 11 year cycle. Figure 1.2.2 is a diagram showing the location on the Sun's surface where the sunspots appear during the cycle.

1.3 The Sun's Internal Dynamo

George Ellory Hale recorded that spectral lines in the Sun in the vicinity of sunspots were split into several lines. This phenomena is called the "Zeeman Effect" because it was first noticed in spectral lines by Pieter Zeeman in 1896 (Zeeman, 1897). The Sun's surface is hot enough to ionize hydrogen atoms, and any electrically charged particle can be deflected

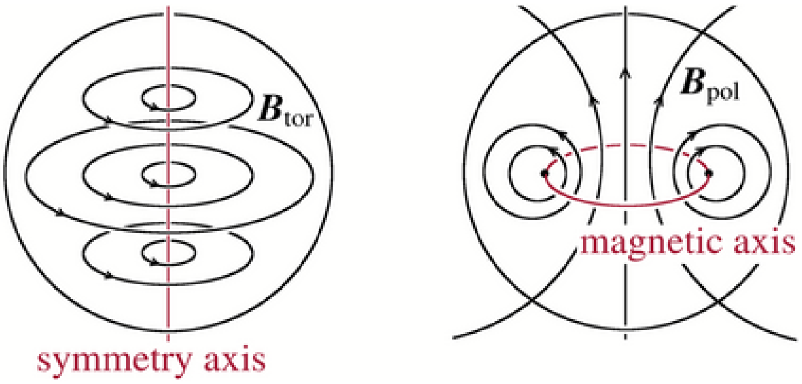

Figure 1.3.1: On the left shows the direction of toroidal field and on the right poloidal. Image taken from (Herbrick & Kokkotas, 2017).

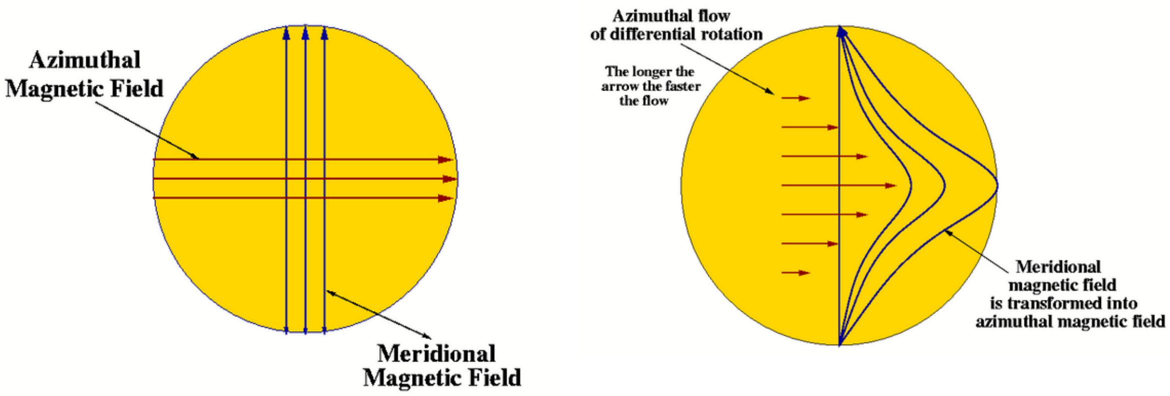

Figure 1.3.2: The effect of the Sun's differential rotation on the poloidal field, pushing it into toroidal, and the effect on the azimuthal and meridonal fields as seen on the surface. Image taken from (NWRA, 2024).

by a magnetic field. Hale thought that sunspots might be associated with rotating "storms" of hydrogen gas as electrons emitted from atoms on the Sun's surface get caught in these storms creating magnetic fields in the proximity of the spots. Spot configurations might be an indicator of a magnetic field on the Sun's surface (Hale, 1908). A regular pattern of sunspot cycles however, indicates that some process much deeper in the Sun may be causing the magnetic activity we see on the surface.

The early drawings on the Sun's surface in the 17th century have left records of the positions of sunspot groups which revealed that the Sun was rotating in a differential manner and not as a solid ball (Casas & Vaquero, 2014, and references therein). Today it is understood that differential rotation (DR) extending into the Sun's interior winds up the poloidal field generated to form a toroidal field configuration, in a process called the *omega* effect (Hathaway, 2014). These fields emerge at the surface after being twisted as they rise through the convective zone (the *alpha* effect, See for example https://solarscience.msfc.nasa.gov/dynamo.shtml). Together this cycle in the Sun occurs approximately every 11 years each time reversing the polarity in what is called an α-Ω dynamo (Hathaway, 2014; NWRA, 2024). This has the effect of pushing the sun spots from the mid latitudes toward the equator as the sunspot cycle moves toward a minimum.

Helioseismic studies of the Sun's surface indicate the existence of a very thin layer (less than 5% of the Sun's diameter, called the *tacholine*) between the Sun's radiative zone and the convection zone. The shear forces between the almost solid rotation of the radiative zone and the differentially rotating convection zone results in the creation of the azimuthal magnetic field that rises on the Sun's surface. The tacholine therefore is thought to be where the Sun's poloidal field is converted into toroidal (Parker, 1993; Choudhuri, 2017). Exactly how the Sun's toroidal field can be generated at this location is not fully agreed upon, however dynamic calculations indicate that magnetic fields can be stored in this somewhat stable location in the Sun, and driven to the surface by buoyancy forces in the convection zone. This buoyancy gives rise to twisted bipolar magnetic regions (BMR) near the Sun's surface which appear as sunspots (Ossendrijver, 2003).

From this analysis, it might be predicted that younger faster rotating stars, with a larger DR than the Sun will exhibit a dynamo dominated more by a turbulent convection zone over the star's DR (an α^2 or α^2-Ω dynamo). This is because the differential rotation introduces shear layers which create turbulence in the convection zone. Over time the magnetic braking of the star will result in mass loss in the star, a reduced DR and convert this kind of dynamo into an α-Ω cycle seen in the Sun today (Brandenburg et al., 1989; Moss et al., 1995; Noraz et al., 2024).

It is still not clear how the Sun converts this toroidal field back into poloidal although Babcock (1961) and Leighton (1969) produced the leading theory as to how this might happen. The decay of sunspots of different polarities at opposite ends of a flux tube could spread out and eventually produce a poloidal field (Charbonneau, 2005). This theory is knows as the *flux transport dynamo model*, or *Babcock-Leighton model*, also knows as the BL model (Choudhuri, 2017).

There are alternate theories concerning the Sun's magnetic dynamo in that it is created throughout the convection zone or even the near-surface shear layer (NSSL) (Brandenburg, 2005; Charbonneau, 2014), contrary to the above-described picture of the dynamo created in the Sun's tacholine. Vasil et al. (2024) argue that recent breakthroughs in the field of large-scale Magneto-Rotational Instability (MRI) have so far not been applied to the Sun. An MRI driven solar dynamo can create a toroidal field near the solar surface. Magnetohydrodynamic (MDH) instabilities can then contribute to recreate the poloidal field and the entire Babcock-Leighton process. This theory is consistent with the observed "torsional oscillations" which follow sunspot migration (Snodgrass, 1987) and the lack of high latitude shear disruptions which are predicted by tacholine-induced dynamo theories (Howe, 2020).

1.4 Late-F Stars

Late-F stars are important because they represent a transition from solar-type stars to intermediate mass stars with implication for stellar magnetic fields (Breton et al., 2020). F-type stars are believed to have a specific position on the Hertzsprung-Russel (HR) diagram somewhere in the F spectral region, where the changeover from fossil magnetic fields in hot stars to dynamo-driven fields in cool stars occurs (Simon & Landsman, 1991; Wolff & Simon, 1997;

Mizusawa et al., 2012; Seach et al., 2020). It is well known that the surface temperature of a star has a direct effect on the size of its convection zone with thin convection zones for the hotter stars and the coolest stars being fully convective (Böhm-Vitense, 1992). Late-F stars are expected to be more massive and hotter, with thinner convection zones, than the other solar-type stars on the HR diagram.

To learn more about the Sun's magnetic field, we need examples from similar stars at different places in the evolutionary cycle. Direct measurements of magnetic fields on the surface of other solar-type stars in the galaxy is difficult or nearly impossible due to their great distance. However, methods have been developed in the last few decades to infer magnetic topologies from an in-depth analysis of a distant star's spectra. This involves the study of the polarisation state of star light and the application of reverse methods to produce brightness and magnetic maps of stellar surfaces from the effect a star's magnetic field has on its spectra.

(Waite et al., 2011) observed the spectra of a number of stars to build a candidate list to be used for futher study using ZDI. The three stars in this thesis, VXR 77A, HD 43989 and HIP 71933 were found to be late-F stars with little previous observation and strong indications of a magnetic field. All three are young, have a reasonable brightness and a rotation rate sufficient for ZDI. Subsequent observations of these stars (outlined in this thesis) produced data sets which were used in this thesis for both DI and ZDI analysis.

1.5 Observations and Analysis of Solar-type Stars

A technique called Doppler Imaging (DI) was developed in the early 1980s to resolve surface characteristics on distant stars by measuring the distortion dark spots create on the spectral lines of a star's surface. By observing the deviation of spectral lines from a star as it rotates it is now possible to map the passage of spots across the surface (Vogt & Penrod, 1983; Rice, 2002). A variation of DI called Zeeman Doppler Imaging (ZDI) measures the polarisation of a star's light in addition to intensity to map magnetic field configurations across the star's surface (Semel, 1989). A detailed explanation of these techniques and how they are used is provided in Methodologies Section 3.

Solar-type stars are usually defined as having a near solar mass and surface temperature. For purposes of this thesis a solar-type star will be defined as one existing on the HR diagram between late-F and early-K (de Strobel, 1996; Soderblom & King, 1997). Among solar-type stars, F-type stars occupy a place on the HR diagram representing a transition from high-mass stars with thin convection zones to low mass cool stars with thicker convection zones. Thinner convection zones in high-mass stars are believed to have weaker or non-existent dynamos and their magnetic fields are therefore fossil. Thicker convection zones are believed to be needed to produce a dynamo effect which will create more dynamic magnetic fields. The transition between these states is somewhere in the middle of the F classification (Landstreet, 1991; Mestel, 2012; Seach et al., 2022). Data sets for F class stars are currently few, especially for young late-F stars. Mature F stars are seen to have rapid magnetic cycles (Takeda et al., 2007; Borsa et al., 2015; Mengel et al., 2016; Jeffers et al., 2018; Brown et al., 2021), with less data for young late-F stars (Hackman et al., 2016). The objective of this study is to add to the small database of young late-F stars and their magnetic structure.

1.6 Research Goal

As previously mentioned among DI and ZDI studies of solar-type stars, there is a dearth of late-F stars in the literature. How do these stars compare with early and mid -G stars (like the Sun) and what can they tell us about the magnetic characteristics and internal dynamos of such stars? Are there any patterns leading into G-type stars? Therefore, this thesis aims to pursue the research goal of studying the star spot and magnetic fields of three solar-type stars of spectral class to F, to make comparisons of their dynamos, time-dependent changes in their field configurations, and explore what should be the boundary between dynamo fields in thin stellar convective layer and the need to invoke a fossil magnetic field. Therefore, this thesis will analyze the surface brightness and magnetic characteristics of the following three late-F stars, namely VXR77A (F8V), HD 43989 (V1358Ori) (F9V) and HIP 71933 (F8V), using data obtained at the 2.3-m telescope and the Anglo-Australian Telescope (AAT) at Siding Spring Observatory, the Telescope Bernard Lyot (TBL) at Pic du Midi observatory, and the 3.6-m telescope at La Silla observatory over the course of several years of observation between December 2003 and June 2019.

2 LITERATURE REVIEW

Since the development of DI and ZDI a number of surveys identified candidate stars for study using these techniques. There is only a small number late-F type stars so far observed. These include HR 1817 (F8V , ~27 Myr) (Budding et al., 2002; Marsden et al., 2006a), HD 35296 (F8V, ~39 Myr) (Waite et al., 2015), and HD 43989 (F9V, ~24-28 Myr). (Hackman et al., 2016; Kriskovics et al., 2019), see Table 2.0.1. This thesis will include early-G class stars in this review. These stars are shown in Figure 2.0.1.

Table 2.0.1 displays the stellar parameters for the stars examined in this review, including DR measurements where calculated. Using photospheric temperatures and luminosity values obtained from the Gaia releases (Gaia et al., 2018) these stars can be placed on a grid of stellar atmospheric models developed by Baraffe et al. (2015) in Figure 2.0.1. From this the masses and ages of the stars can be estimated.

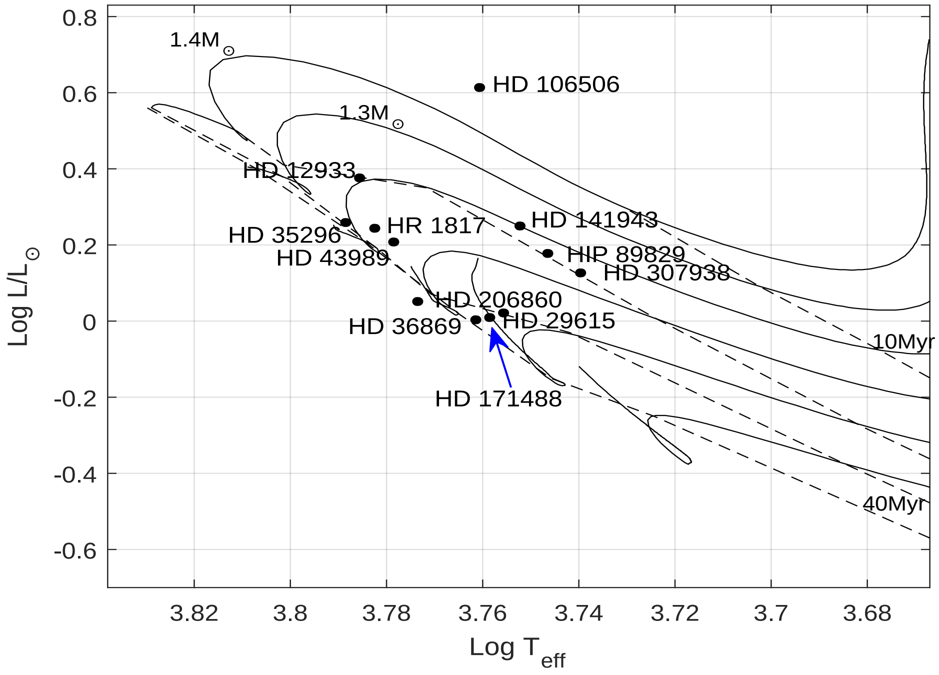

Figure 2.0.1: Stellar Ages and Masses. Surface temperatures and luminosity values for each star described in the review were obtained from the Gaia release (Gaia et al., 2018) and are plotted in an HR diagram of 0.9 to 1.4 M$_\odot$ in 0.1 M$_\odot$ increments against evolutionary track models provided by Baraffe et al. (2015). Stellar ages of 10, 20, 30 and 40 Myr are overlayed as isochrones. Ages in this plot differ slightly from some of the ages from previous research in Table 2.0.1 as they are derived from the more recent Baraffe models and Gaia DR2. These stars were chosen because they represent a near total set of young late-F and early-G stars studied with DI/ZDI closest to the target stars selected for this thesis. There are more early G stars than late-F due to the rarity of the latter stars so far in the literature.

Table 2.0.1: Stellar Parameters for potential target stars

Star	Spectral	Age	$T_{\rm eff}$	vsini	rotation	dΩ	References
HD 171488 (V889 Her)	G2V	~30-50 Myr	5830 ±50 K	38 ± 0.5 km s^{-1}	~1.34 days	Stokes *I* data 0.383 ± 0.042 rad d^{-1} 0.4 ±0.15 0.41 ±0.02 Stokes *V* data 0.45 ±0.053 0.415 ±0.016	(Strassmeier et al., 2003) (Marsden et al., 2006a) (Jeffers & Donati, 2011) (Willamo et al., 2019)
HD 307938 (R58)	G2V	~35Myr	5800 ± 100 K	92 ± 0.5 km s^{-1}	~0.56 days	Stokes *I* data 0.025 rad d^{-1}	(Marsden et al., 2005)
HR 1817	F8V	~27 Myr	6080 ± 50 K	~52 ±0.5 km s^{-1}	~1.0 days	Stokes *I* data – Stokes *V* data 0.259 ± 0.019 rad d^{-1}	(Budding et al., 2002) (Marsden et al., 2006a)
HD 106506	G1V	~5 Myr	5900 ± 50 K	79.4 ± 0.5 km s^{-1}	1.39 ± 0.01 days	Stokes *I* data $0.21^{+0.02}_{-0.03}$ rad d^{-1} Stokes *V* data 0.24±0.03 rad d^{-1}	(Waite et al., 2011)
HD 141943	G2 C	~15 Myr	5850 ±100 K	35 ± 0.5 km s^{-1}	~2.18 days	Stokes *I* data 0.24 ± 0.03 rad d^{-1} Stokes *V* data 0.40 ± 0.13 rad d^{-1}	(Marsden et al., 2011a)
HD 206860 (HN Pegasi)	G0V	~200 Myr	5974 K	~10.6 km s^{-1}	4.6 days	Stokes *I* data 0.22 ±0.03 rad d^{-1}	(Boro Saikia et al., 2015)
HD 35296	F8V	~39 Myr	6170 K	15.9 ±0.01 km s^{-1}	3.48 ± 0.01days	$0.22^{+0.04}_{-0.02}$ rad d^{-1}	(Waite et al., 2015)
HD 29615	G3V	~38 Myr	5820 ± 50 K	19.5 ± 0.01 km s^{-1}	~2.34 days	Stokes *I* data $0.07\ ^{+0.10}_{-0.03}$ rad d^{-1} Stokes *V* data $0.48\ ^{+0.11}_{-0.12}$ rad d^{-1}	(Waite et al., 2015)
HD 36869 (AH Lep)	G3V	~39 Myr	5798 ± 60 K	26.3 km s^{-1}	~1.31 days	–	(Hackman et al., 2016) (Gaia et al., 2018)
HD 12933 (EK Dra)	G1.5V	~30 Myr	5561 K	16.4 ± 0.1 km s^{-1}	2.766 ± 0.002 days	Stokes *I* data – Stokes *V* data $\sim 0.27\ ^{+0.12}_{-0.14}$ rad d^{-1}	(Waite et al., 2017)
HD 43989 (V1358 Ori)	F9V	~24-28 Myr	6050 ± 25 K	41.3 km s^{-1}	1.16 days	–	(Hackman et al., 2016) (Kriskovics et al., 2019)

2.1 Star spots

HD 12933 (EK Draconis) (G1.5V, ~30 Myr) is one of the most observed solar-type stars using DI, because of its brightness and spectral type close to the Sun. It is a member of the Pleiades group (Montes et al., 2001) and is an important proxy for the young Sun. The first Doppler images of EK Draconis (EK Dra) were made by Strassmeier & Rice (1998) using the Canada France Hawaii Telescope (CFHT) from March 12 to March 17 1995. It was the first Doppler image of a solar-type star. Large high-latitude features are seen in most of the maps which include polar "cap-like" spots in most of the maps, although two maps show the high-latitude features without a polar spot (Strassmeier & Rice, 1998). The temperature maps revealed a high-latitude feature at approximately 45° latitude and a possibility of a smaller polar spot between 60°and 80°latitude.

At the time of this observation, polar spots had been observed on more evolved stars such as RS CVn stars and did not fit current flux tube models for younger rapidly rotating stars such as EK Dra (Schüssler et al., 1996). Strassmeier & Rice (1998) speculated that the existence therefore of these polar spots on solar-type stars will require modification of flux tube transportation models of that time that will allow for movement of toroidal flux tubes to higher stellar latitudes. The discovery of further polar spots on solar-type and non-solar type stars revealed a relationship between rotation speeds and the existence of high-latitude spots requiring models with non-solar differential laws (Strassmeier et al., 2000), in addition to the assumption of poleward meriodinal circulation with more frequent magnetic spot reconnections near the pole than near the equator (Strassmeier & Bartus, 2000) and a poleward "slip" of the anchored part of the flux tubes caused by a Coriolis effect (Granzer et al., 2000).

Waite et al. (2017) observed EK Dra from late 2006 until early 2012 for a total of five epochs, the longest lasting over a month with nearly consecutive nightly observations. This is the most extensive DI and ZDI images recorded of EK Dra up to that time. High latitude spots are observed between 2006 and 2008 and a distinctive polar spot is observed in the 2012 observation, indicating significant spot evolution over this period. Järvinen et al. (2018) observed EK Dra for ten nights in 2015. Mid to high latitude spots were observed in both epochs, but no polar spots were seen. Additional photometric observations made add to the 40+ years of photometric data available for EK Dra to refine a spot cycle to 8.9 ± 0.2 years. Senavci et al. (2021) observed EK Dra in 2015 and 2016. A strong polar spot along with high to mid-latitude spots were observed, which compares to an off-center polar spot with a high-latitude ring predicted by flux emergence and transport (FEAT) simulations (Isik et al., 2018). From these comparisons, the authors suggest that the polar spot is produced by activity in the convection zone and rotational effects of flux tubes rising in the zone.

Among late-F stars, Marsden et al. (2006a) observed HR 1817 in late 2001 and late 2004. In both epochs a strong polar spot was seen with little spots at lower latitudes. HD 43989 (one of the stars studied in this thesis) was observed by Hackman et al. (2016) in late 2013. An off-center dark spot is seen at the pole with with other spots concentrated at high latitudes. HD 43989 was again observed by Kriskovics et al. (2019) between early 1997 and early 2015. A large dominant polar spot was observed with lesser features observed at lower latitudes down to the equator.

Dominant polar spots have been observed on other cooler solar-type stars. HD 171488 (G2V, ~30-50 Myr) has been observed extensively for decades, using DI observations made between 1999 and 2017. A dominant asymmetric polar spot, varying in size is seen in all observations, with none showing the visible pole with no spots (Marsden et al., 2006a; Jeffers & Donati, 2011; Willamo et al., 2019). HD 307938 (G2V, ~35 Myr) was observed in 2000 with a fragmented spot extending from the pole down to ~60° latitude (Marsden et al., 2005). HR 1817 was observed in 2001 and 2004 with a large dominant polar spot (Marsden et al., 2006a). HD 29615 (G3V ~38 Myr) was observed in 2009 and HD 106506 (G1V, ~5 Myr) in 2011, both with a large dominate polar spot (Waite et al., 2011). HD 43989 (F9V, ~24-28 Myr) was observed for four nights in 2013 with high and mid-latitude spots and an off-center polar spot (Hackman et al., 2016; Kriskovics et al., 2019).

It is not certain if the large spotted areas in the DI brightess maps are actually groups of smaller spots due to a lack of sufficient resolution (Willamo et al., 2019). During the initial development of DI, polar spots were thought to be caused by inversions or "flat bottoms" in the spectral profiles and thus computational artifacts (Kürster et al., 1994; Rice, 2002). Later observations of an expanding list of stars indicates that large polar spots are real and are common on young solar-type stars (Carter et al., 2015; Choudhuri, 2017). Polar spots may occur because lower-latitude spots are pushed to higher latitudes by a Coriolis effect, or by spots moving poleward because of meridional flows beneath the star's surface (Waite et al., 2011).

2.2 Ring-like features

In addition to polar spots, several solar-type stars have exhibited wreath or ring-like structures in areas near the visible pole. A dominant azimuthal positive field was observed surrounding the visible pole of HD 171488 and HR 1817 in early 2002 and late 2004 (Marsden et al., 2006a). A ring of azimuthal field seen at the pole was observed on HD 141943 in 2007, 2009 and 2010 (Marsden et al., 2011a). A ring in the radial magnetic field component is seen around the pole on HD 206860 in late 2013 (Boro Saikia et al., 2015). A positive azimuthal ring-like structure was observed around the pole of HD 29615 in late 2009, although the structure was not a complete ring (Waite et al., 2015). Azimuthal field rings were observed on HD 129333 betwen 2006 until early 2012 (Waite et al., 2017). Jeffers & Donati (2011) observed HD 171488 with a large number of exposures between early 2007 and early 2008. A permanent ring of azimuthal field was observed surrounding the visible pole and was seen to evolve over the data sets. HR 1817 (F8V) was seen to have a positive azimuthal ring around the visible pole (Mengel, 2005; Marsden et al., 2006a), the only late-F star observed prior to this thesis with such a structure.

Several models have been developed that predict the existence of wreath-like structures on rapid-rotating solar-type stars. Schrijver & Title (2001) produced a model using a random-walk flux dispersal that produces a ring-like structure at high latitudes that is opposite polarity to a polar spot. A model proposed by Granzer et al. (2000) is based upon starspots shifting toward the poles due to rapid rotation and produces similar wreath-like structures. Holzwarth & Schüssler (2002) conducted simulations for binary systems, finding that preferred longitudes for spot clusters can be caused by tidal effects of a secondary resulting in spot clusters 180 degrees apart in a ring of high latitudes. The flux tubes in these simulations occur at the base of the convection zone (Holzwarth, 2004).

2.3 Active Longitudes and Flip-Flops

Other active stars have been observed to form concentrations of spots which are 180°apart in what are termed "active longitudes" (Korhonen & Järvinen, 2006). Spots in active longitudes separated by 180°were reported on EK Draconis by Järvinen et al. (2005). These concentrations appear to jump from one active longitude to another in a period of about 4 to 4.5 years (Järvinen et al., 2005). Kriskovics et al. (2019) reports weak active longitudes on HD 43989 that reverse in a time period of ~6 years.

Jetsu et al. (1993) coined the term "flip-flop" in 1993 for a phenomenon observed on the giant star FK Comae Berencies, in which spot activity on two active longitudes 180 degrees apart switches over a short period of time. Berdyugina (2005) reports similar activity on three solar-analogs, LQ Hya, AB Dor and EK Dra (listed in this review). Korhonen & Järvinen (2006) report similar phenomenon observed in giant binary stars XX Tri and UZ Lib in archived data sets. This behavior was also described by Järvinen et al. (2005) for EK Dra and by Kriskovics et al. (2019) with a flip-flop period of ~6 years on HD 43989. There are not many stars where flip-flops are described, approximately 10 total according to Korhonen & Järvinen (2006), and they are all based upon photometry, not DI. So far there is no statistically significant correlation between flip-flops and stellar parameters.

Jetsu (2018) argues that this phenomenon is illusory and caused by the interference of light-curves of spots that are long-lived (i.e. active longitudes). This explains a number of mysteries associated with these flip-flops, including why DI images show different rotation periods than light curves, and why there is a scarceness of observations. This leads to the possibility that flip-flops of spots in active longitutes reported in other papers are erroneous and that the phenomenon does not exist (Jetsu et al., 1993; Hackman et al., 2013; Wang et al., 2015; Özdarcan et al., 2016; Jetsu, 2018; Savanov et al., 2019).

2.4 Differential Rotation

The DR of a solar-type star results in a strong toroidal field being generated from an initial poloidal field, in the α-Ω dynamo. Stars with a low surface DR are more likely to have an α^2 dynamo.

Barnes et al. (2005) observed ten solar-type stars where DR was obtained from the DI observations and found that the DR decreases with decreasing effective temperature. Distefano et al. (2016) observed 111 stars in 11 associations and obtained DR from long-term photometry. They attempted to establish a lower limit to surface DR to understand how it relates to global stellar parameters in stars from 4 to 95 Myr age. These authors find that dΩ increases with effective temperature $\mathrm{T_{eff}}$, however not at the rate observed by dΩ increases with decreasing convective turnover, and dΩ increases with stellar age in the first 30 Myr. This is in agreement with models that predict that stars with large convective zones will experience lesser DR.

Figure 2.4.1 shows surface diffential shear $d\Omega$ versus convective zone depth as a function of solar radius for the stars in this review. Convective zone depth was calculated from the radius and radiative core sizes for the star's mass and radius from models in (Baraffe et al., 2015). Figure 2.4.2 shows surface differential shear versus surface temperature.

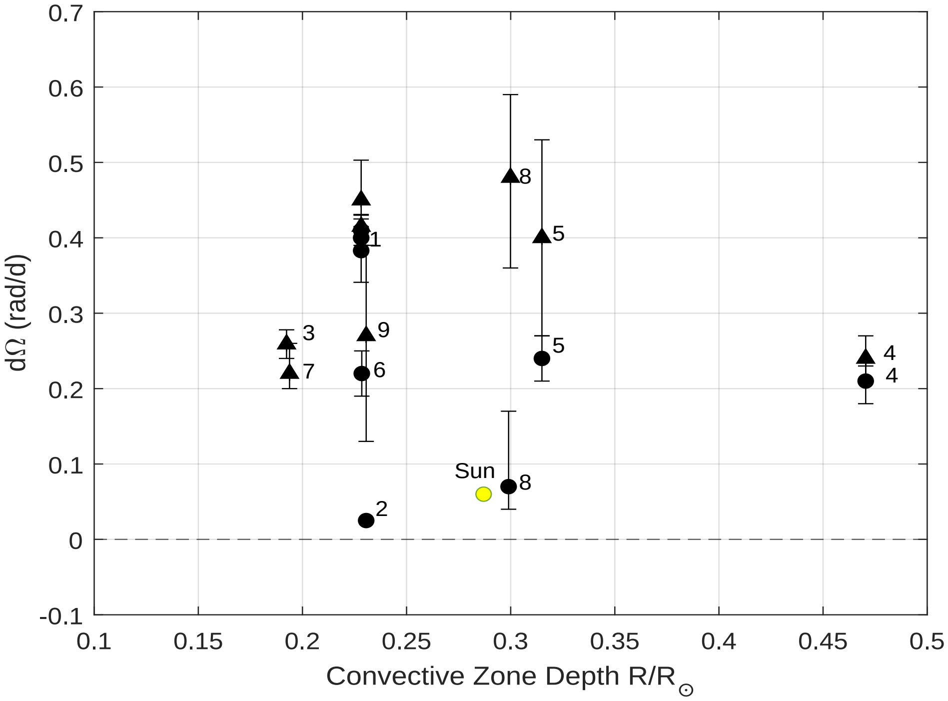

Figure 2.4.1: Surface differential shear $d\Omega$ versus convective zone depth as a function of solar radius for the stars in this review. Dots show surface differential shear from surface brightness analysis and triangles from surface magnetic analysis. The convective zone depth was calculated from evolutionary models in Baraffe et al. (2015). References cited are for the dΩ values. Errors are plotted where published. The value for the Sun's dΩ is taken from Küker & Rüdiger (2008). The value for the Sun's convective zone depth is taken from Hathaway (2022).

[1] HD 171488 (V889 Her), G2V (Marsden et al., 2006a), (Jeffers & Donati, 2011)
[2] HD 307938 (R58), G2V (Marsden et al., 2005)
[3] HR 1817, F8V (Marsden et al., 2006a)
[4] HD 106506, G1V (Waite et al., 2011)
[5] HD 141943, G2 C (Marsden et al., 2011a)
[6] HD 206860 (HN Pegasi), G0V (Boro Saikia et al., 2015)
[7] HD 35296, F8V (Waite et al., 2015)
[8] HD 29615, G3V (Waite et al., 2015)
[9] HD 12933 (EK Dra) , G1.5V (Waite et al., 2017)

2.5 Fossil Fields

The concept of fossil magnetic fields was proposed by (Cowling, 1945) who showed that the ohmic dissipation of a star's magnetic field could exceed the lifetime of the star (Dudorov & Khaibrakhmanov, 2015). Such fossil fields may be remnant magnetic fields from the primordial cloud (Desch & Mouschovias, 2001) or fields generated by a dynamo process early in the star's formation (Kunz & Mouschovias, 2010; Marsden et al., 2023, and references therein). The switch from dominant fossil magnetic field is thought to occur somewhere in the range of F-type stars, with estimates from early- to mid-F (Seach et al., 2022; Marsden et al., 2023) to solar-type activity firmly established at around F7 (see Berdyugina (2005,

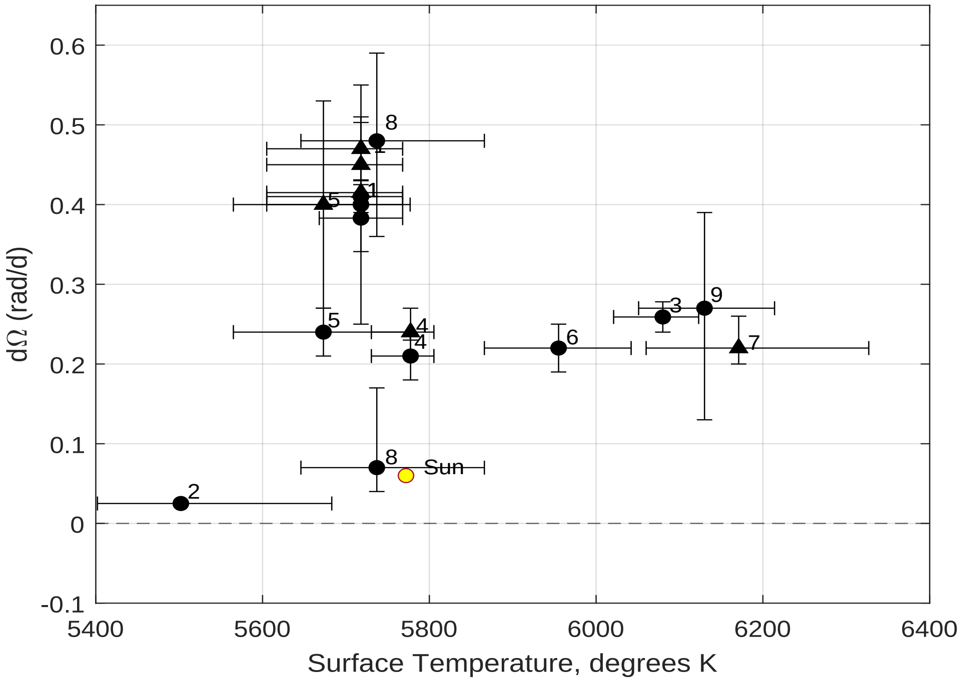

Figure 2.4.2: Surface differential shear $d\Omega$ versus photospheric temperature for the stars in this review. Dots show surface differential shear from surface brightness analysis and triangles from surface magnetic analysis. Values for differential shear are taken from the references below. Values for photospheric temperature are taken from Gaia DR 2 (Gaia et al., 2018). The value for the Sun's dΩ is taken from Küker & Rüdiger (2008). The value for the Sun's surface temperature is taken from Hathaway (2022).

[1] HD 171488 (V889 Her), G2V (Marsden et al., 2006a; Jeffers & Donati, 2011)
[2] HD 307938 (R58), G2V (Marsden et al., 2005)
[3] HR 1817, F8V (Marsden et al., 2006a)
[4] HD 106506, G1V (Waite et al., 2011)
[5] HD 141943, G2 C (Marsden et al., 2011a)
[6] HD 206860 (HN Pegasi), G0V (Boro Saikia et al., 2015)
age estimate for this star is from (Gaia et al., 2018)
[7] HD 35296, F8V (Waite et al., 2015)
[8] HD 29615, G3V (Waite et al., 2015)
[9] HD 12933 (EK Dra) , G1.5V (Waite et al., 2017)

and references therein)).

2.6 Dynamo Magnetic Fields and Cycles

Since the time Hale realized the spots on the Sun were caused by magnetic flux lines, magnetic activity on distant stars has been inferred by an analysis of chromospheric emission (Wilson, 1966, 1978) (as one method for detection of magnetic fields on stars). The Mt Wilson survey has accumulated data of chromospheric activity from over 2000 stars between 1966 and 2002 from their Ca II H and K lines (referred to as the "S-index") (Duncan et al., 1991; Baliunas et al., 1995; NSO, 2023). A large number of magnetic cycles have been inferred from these analysis on the order of two to six years (Wilson, 1978; Kriskovics et al., 2019; Boro Saikia et al., 2015, 2022).

Järvinen et al. (2005) compiled and analyzed photometric data for EK Dra spanning a time period of 21 years from observations taken between 1984 and 2004, in order to search for persistent long-lasting spot formations and activity cycles using a technique of light-curve inversion. Estimates of cycle range from 9 to 30 years, and combined with long-term brightness values obtained from observations previous to this period, they conclude that EK Dra has decreased in brightness steadily for a period of 45 years (Järvinen et al., 2005). This might imply that the small cycles seen in other stars are within cycles of much longer duration, and that there are no as yet definitive records of such cycles because of the very long observational periods required.

In our Sun, the radiative zone is believed to rotate as an almost solid body and the convection zone rotates differentially. The difference between these zones drives the dynamo. The Sun is known to operate in two 11 year cycles, in which an initial poloidal field is twisted into a dominant toroidal field and then regenerates back to poloidal, the system by which is first proposed by (Parker, 1955). The process repeats with the Sun's magnetic poles reversed, and then realigned. How this field reverses from dominant toroidal to dominant poloidal is not yet known (Petit et al., 2008, and references therein).

Magnetic fields of young solar-analogues are easier to analyze than stars more similar to our Sun because they rotate more rapidly, creating broader line profiles with the circularly polarized lines better separated. The results of these analyses is that young solar-type stars appear to have a more chaotic magnetic field with little evidence of solar-like cycles (Baliunas et al., 1995; Jeffers & Donati, 2011; Waite et al., 2011, 2015; Perugini et al., 2021; Marsden et al., 2021). In these stars, the toroidal component may appear as strong azimuthal fields near the surface of the star (see Waite et al. (2015, and references therein)).

Nine of the stars listed in Table 2.0.1 were observed with spectropolarimeters collecting Stokes V data. Two epochs of observations of HD 171488 show a dominant toroidal field energy of 56% which evolved to 70% over a 6 month period (Jeffers & Donati, 2011). HD 106506 was observed in one epoch to have a dominant toroidal field of ~70% (Waite et al., 2011). HD 141943 displayed a shift from a balanced poloidal-toroidal configuration with the poloidal field becoming more dominant in two years (Marsden et al., 2011a). HD 43989 shows a dominant toroidal field of ~69% in one epoch. HD 35296 shifted from a low toroidal percentage of ~18% to a 50-50% configuration in one year (Marsden et al., 2011a). Other stars exhibit a dominant poloidal field including HD 29615 and HD 43989 (Waite et al., 2015; Hackman et al., 2016). High-latitude azimuthal field rings are seen in HD 171488, HD 106506 and HD141943. Dipole fields were dominant in all except HD 106506 which had a dominant octopole field. All were axisymmetric in the toroidal field. Figure 2.7.1 shows percent of toroidal magnetic field energy for the review stars versus rotational period. There is a roughly even distribution of poloidal versus toroidal percentages versus rotation period. In summary, there is a mix of complex field configurations with the roughly even distribution of poloidal versus toroidal field percentages somewhat unexpected (Petit et al., 2008).

Unlike the Sun, cycles in stars previously observed from photometric and spectroscopic data do not always correspond directly to cycles observed with spectropolarimeters. Boro Saikia et al. (2022) observed κ Ceti (G5V), a young solar-analogue star using the Mt Wilson survey data and six months of spectro-polarimetric observations and observed a lack of correlation between the chromospheric activity data and magnetic cycle obtained from the Stokes V data.

Overall there are only a small number of magnetic reversals observed in stars from the Stokes V data. Magnetic reversals have been observed on 61 Cyg A (K5V), τ Boo (F8V) and HD 75332 (F7V). These stars are not young solar-analogues but mature main-sequence (MS) stars. Willamo et al. (2022) reports a complete magnetic reversal from their observations and earlier ones for HD 43989 (F9V) and a possible magnetic reversal for HD 35296 (F8V). Perugini et al. (2021) reports a possible field migration that might be the early stages of a reversal for HIP 89829 (G5V). These are all young solar-analogues.

Petit et al. (2008) studied four mature solar-type stars and observed that the magnetic fields were mostly poloidal for slow rotation rates. More rapid rotators exhibit a stronger toroidal component. From this they conclude a rotation period lower than ~12 d is required for the toroidal magnetic energy to dominate. Figure 2.7.1 shows percent toroidal magnetic energy versus rotation period for the stars in this review. This chart from research later than Petit et al. (2008) does not support the rotation limit of ~12 d they predict for toroidal energy to dominate, with a number of stars rotating more rapidly than 12 days showing epochs where the toroidal magnetic field component dominates over the poloidal.

2.7 Recovery of spots and magnetic fields via Doppler Imaging and Zeeman-Doppler Imaging

Our ability to view spots on a distant star's surface depends upon our line of sight and the latitude of the spot on the star. The magnetic field signatures on the star are recovered from the circularly polarised light, which is a small percentage of the unpolarised light. This results in a lesser recovery of the Stokes V signature in the region of dark spots(Donati et al., 1992; Donati & Cameron, 1997).

Hackman et al. (2024) tested the magnetic characteristics recovered by ZDI against simulated data in order to test the extent that the stellar parameters affect the magnetic reconstruction and how well the magnetic surface field data is preserved. They used magnetohydrodynamic (MHD) simulations near the surface of the simulated star to test the ZDI process. They found that the recovered field strength will be less than the "real" value (from the MHD simulations) because opposite field polarities will be blurred in the inversion. They also find that the axisymmetry of the surface field was overestimated, especially for simulated fields that are non-axisymmetric. The best comparisons resulted from an inclination i ~ 60°and $v\sin i$ > 40 km s^{-1}, with increasing parts of the surface invisible below $v\sin i$ < 40km s^{-1}. The magnetic field energy strength in specific l values (see Section 3.2.2 for a definition of l values) is thought to be unreliable, although the percentage of poloidal versus toroidal energies and the ratio of axisymmetric versus non-axisymmetric were well reproduced. Not surprisingly the quality of the data was important; high spectral resolution, high SNR and dense rotational phase coverage improves the recovery of the magnetic images.

Comparisons between the measurement of magnetic field strength measured from ZDI versus measurements of Zeeman broadening have found that the Zeeman broadening recovers a much higher level of magnetic field strength because it is not affected by the cancellation of opposite field polarities (See et al., 2019; Kochukhov et al., 2020). The new spectropolarimeter SPIRou at the CFHT has the capability of simultaneous ZDI and Zeeman broadening measurements in order to provide an accurate measurement of both the small scale field components as well as the overall field strength (Moutou et al., 2017).

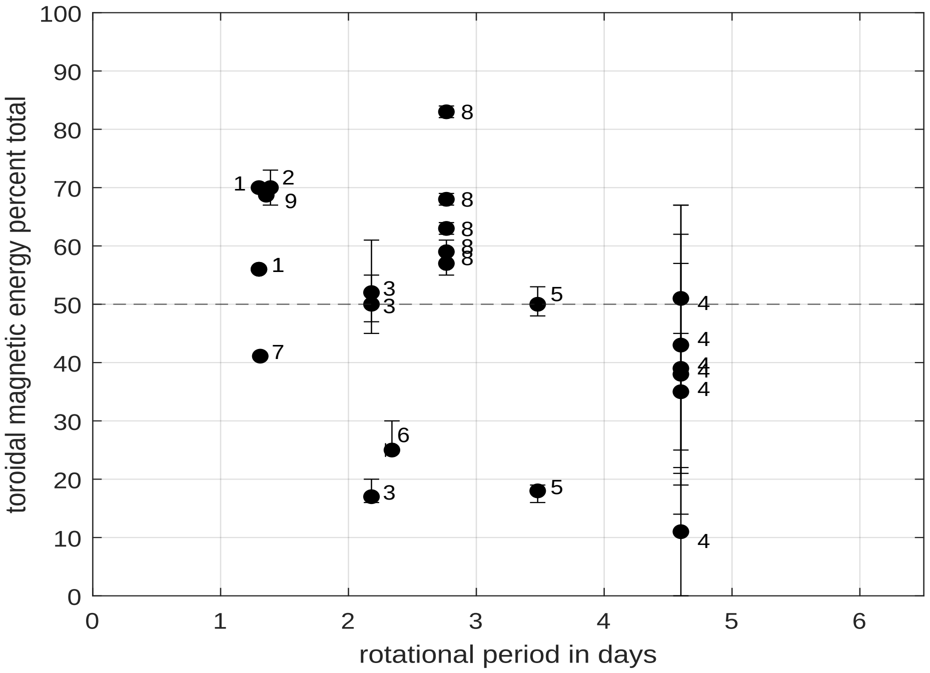

Figure 2.7.1: Percent of toroidal magnetic field energy for the review stars with Stokes *V* data versus rotational period. Poloidal and toroidal percentages were calculated for each of the stars from the referenced studies. Stars with multiple epochs of ZDI observations are plotted as individual points. Errors are plotted where published.

[1] HD 171488 (V889 Her), G2V (Jeffers & Donati, 2011) Epochs 2007.39 and 2007.77

[2] HD 106506, G1V, (Waite et al., 2011), Epoch 2007.24

[3] HD 141943, G2V, (Marsden et al., 2011a), Epochs 2007.26, 2009.27, 2010.24

[4] HD 206860 (HN Pegasi), G0V, (Boro Saikia et al., 2015), Epochs 2007.67, 2008.71, 2009.54, 2010.62, 2011.67, 2013.68

[5] HD 35296, F8V, (Waite et al., 2015), Epochs 2007.06, 2008.05

[6] HD 29615, G3V, (Waite et al., 2015), Epoch 2009.90

[7] HD 36869 (AH Lep), G3V, (Hackman et al., 2016), Epoch 2009.69

[8] HD 129333 (AH Lep), G1.5V, (Waite et al., 2017), Epochs 2006.99, 2007.07, 2007.08, 2008.06, 2012.03

[9] HD 43989 (V1358 Ori), F8V, (Hackman et al., 2016), Epoch 2013.09

2.8 Summary

Spots are observed from near the equator to higher latitudes with large spots visible at the pole, especially for the faster rotating stars. Evolution of what are either large spots or clusters of spots can be seen when multiple epochs of observations are available. The presence of high latitude and polar spots is different from the present Sun. The interplay between buoyancy and coriolis forces from the rapid rotations of the younger stars may be moving magnetic activity poleward. Large azimuthal fields are seen in ring-like structures surrounding the visible pole with associated spot features. These features also evolve over multiple data sets. DR varies from near solid body rotation to rates significantly higher than the Sun. The percentages of poloidal vs toroidal magnetic field strengths are seen to be roughly evenly divided from rotation rates of one to several solar days. Few confirmed complete magnetic reversals have been seen so far on young solar-type stars, with the exception of a cycle reversal on HD 43989 and a possible reversal on HD 35296.

3 METHODOLOGY

3.1 Polarisation of Light and Stokes Parameters

In 1851 Jules Poincaré proposed a sphere to represent polarised light. (Cox & Rosales-Guzmán, 2023). Completely polarised light is represented on the sphere's surface, which is a radius of one. As the fraction of light becomes more unpolarised, the radius decreases. The top of the sphere represents right-hand polarised light and the bottom left-hand polarised light. Linearly-polarised light from circularly to vertical is represented on the circularly equator.

Stokes parameters are a set of numbers in vector format that describe the characteristics of the polarisation of electromagnetic radiation. This mathematical representation was developed in 1852 by George Stokes in reference to the Poincaré sphere because it is more organised and succinct than previous mathematical methods to analyze and describe the polarisation of light. There are four Stokes parameters, S_0, S_1, S_2 and S_3 where:

$$\begin{aligned}
S_0 &= \text{Polarisation state value } I \\
S_1 &= I \cos 2\psi \cos 2\chi \\
S_2 &= I \sin 2\psi \cos 2\chi \\
S_3 &= I \sin 2\chi
\end{aligned}$$

where I = $\sqrt{S_1^2 + S_2^2 + S_3^2}$

This coordinate system was not preferred by mathematicians of Stoke's time but were created because the values can be more easily measured and calculated. This advantage continues into the present where astronomers use Stokes parameters to analyze stellar magnetic fields using modern computers and algorithms. The Stokes parameters are represented as a vector:

$$\vec{S} = \begin{pmatrix} S_0 \\ S_1 \\ S_2 \\ S_3 \end{pmatrix} = \begin{pmatrix} I \\ Q \\ U \\ V \end{pmatrix} \tag{3.1.1}$$

The Q parameter describes the degree of the vertical linearly polarised light, the parameter U describes the degree of the linearly polarised light at ±45°to the linearly polarised light, and the V parameter describes the degree of the circularly polarised light. The values inside the matrices represent flux density. Based on this vector representation and referencing Figure 3.1.1 the most common Stokes vectors are:

$\begin{pmatrix} 1 \\ 1 \\ 0 \\ 0 \end{pmatrix}$ Horizontally linearly polarised light

$\begin{pmatrix}1\\-1\\0\\0\end{pmatrix}$ Vertically linearly polarised light

$\begin{pmatrix}1\\0\\0\\-1\end{pmatrix}$ Left hand circularly polarised light

$\begin{pmatrix}1\\0\\0\\1\end{pmatrix}$ Right hand circularly polarised light

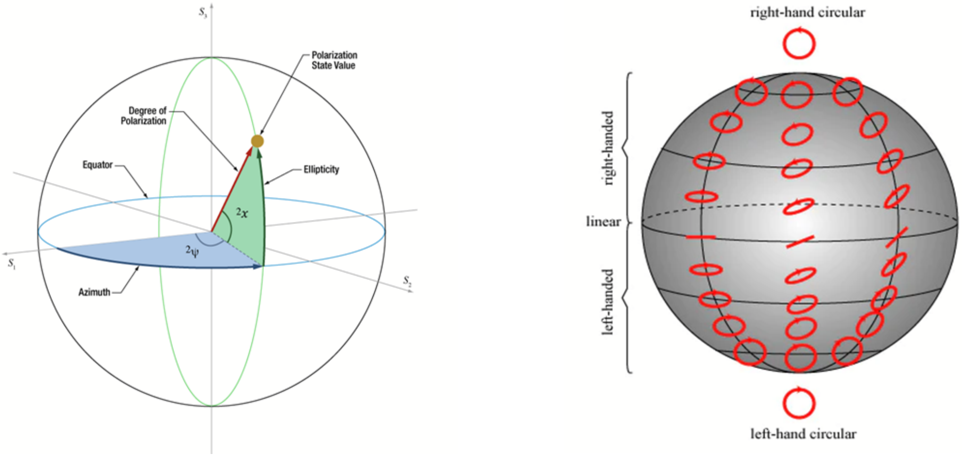

Figure 3.1.1: Poincaré Sphere in spherical and cartesian coordinates. Azimuthal and ellipticity angles are used to map the polarisation states upon the sphere. At places where the light is completely polarised is the largest radius. The image on the left is taken from ThorLabs (2020). The image on the right is taken from FOSCO (2024).

3.1.1 Measurement of Stokes Parameters

The Stokes I parameter is measured by recording the intensity of the spectral lines from a star. The Stokes V parameter will involve placing a wave plate in front of the spectrograph which will convert the right and left hand circular light into vertical and horizontal linearly polarised light. These beams are separated by a beam splitter and form two images of the star at the focal plane. A spectrograph modified or configured in this manner is called a *spectropolarimeter* (Semel et al., 1993), see Figure 3.1.2. Four sub-exposures are taken with the quarter-wave plate rotated 90°between each sub-exposure. This creates Fa "null" spectrum which should be free of any spurious signal (Donati et al., 1997) .

There are a limited number of spectropolarimeters at observatories in the world. Such instruments are highly specialized and oriented almost exclusively towards ZDI. One of these is the High Accuracy Radial Velocity Planet Searcher (HARPS) at La Silla observatory in Chile. When configured with a front-end polarimeter, this instrument is referred to as

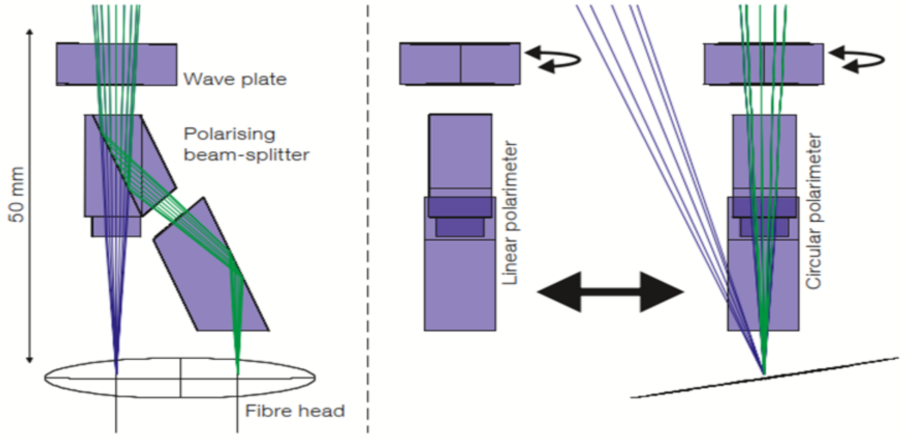

Figure 3.1.2: Schematic of the HARPSpol optical design Left: the view in the sliding direction. Right: side view of the two polarimeters. Image and caption taken from (Piskunov et al., 2011).

HARPSpol (Piskunov et al., 2011). The high-resolution HARPS spectrograph at La Silla observatory was ideal for conversion into a spectropolarimeter, but a permanent configuration of this type would have to eliminate the highly successful transit observations that HARPS was originally designed for. A design was implemented that allowed for the polarimeter configuration to slide a table with two polarisation optics, one for linear polarisation and one for circular in front of the spectrograph. In this manner The HARPS spectrograph could be quickly configured to support spectro-polarimetric observations and can be reconfigured with a linear polariser to support radial velocity measurements for exoplanet detection. Figure 3.1.2 provides a diagram of this setup.

Table 3.1.1: List of observatories with high-resolution spectropolarimeters of varying configurations.

Observatory	Telescope	Notes
Siding Spring Observatory, Australia	Anglo-Australian Telescope (AAT)	UCLES spectrograph connected to SEMEL polarimeter creating a spectropolarimeter configuration. This instrument was decommissioned in 2011 and has been replaced with a higher resolution spectrograph HERMES
Pic du Midi Observatory, France	Telescope Bernard Lyot (TBL)	Spectropolarimeter NARVAL
La Silla Observatory, Chile	3.6-m Telescope	Spectrograph HARPS with a polarimeter that can be lowered into position to create a spectropolarimeter HARPSPol
Mauna Kea Observatory, Hawaii	Canada-France-Hawaii-Telescope	Spectropolarimétre Infrarouge (SPIRou)
Mount Graham International Observatory, Arizona	Large Binocular Telescope (LBT)	Postham Echelle Polarimetric and Spectroscopic Instrument

3.1.2 Least Squares Deconvolution

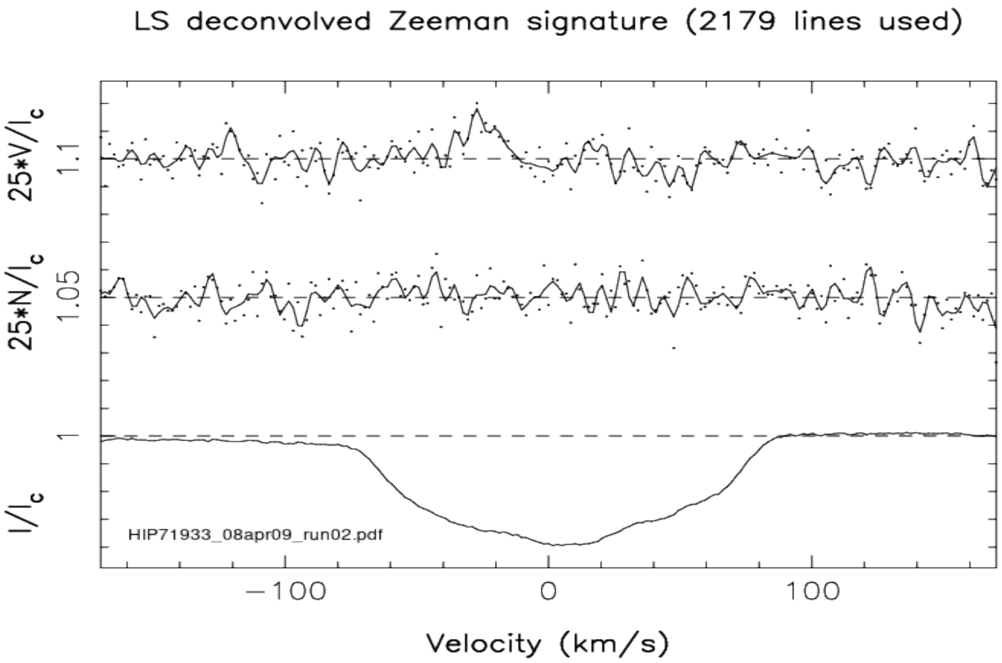

Figure 3.1.3: LSD profile for HIP 71933 epoch 2009.26 observation taken at the AAT on April 08, 2009 used in this study. The top plot is the Stokes *V* profile, the middle plot is a null profile generated by rotating the quarter wave plate at the spectropolarimeter. The bottom plot is the Stokes *I* profile. These profiles were generated from a total of four sub-exposures taken on that date.

Spectro-polarimetric signals associated with distant stars are very weak, and there will be few stars in all observations with spectral lines strong enough to extract Stokes signatures. It is assumed that in any sample of stellar spectra that surface activity on the star will more or less affect all of the spectral lines equally. It is also assumed that these spectral lines will overlap. Because of this a mean of the absorption lines will distorted by the blended lines and a convolution method is used instead.

The entire spectrum of the star is considered to be the sum of scaled and shifted individual spectral lines. The residual intensity of this profile would be a convolution of the summed mean profile with a pre-existing list of line strengths and wavelengths associated with the spectral type of the star (called a *line mask*). The value of a single line profile Z is then a deconvolution of the other terms. This results in a single line profile of high SNR of the Stokes $\frac{I}{Ic}$ or $\frac{V}{Ic}$. It is from these profiles (referred to as "LSD") from each observing run of a star that the DI and ZDI process will perform the reverse calculation to produce brightness and magnetic maps (Donati & Brown, 1997).

This can be expressed:

$$Y = M \star Z \tag{3.1.2}$$

where Y is the observed spectrum
M is the line mask

Z is the estimated mean single line profile

A few additional inputs are required to create the LSD profile. A velocity domain is input to cover the broadening of the spectral line by the star's rotation as well as its radial velocity. This domain must include some continuum on either side of the profile. This value is approximated and adjusted until the domain of the LSD profile is adequately covered. The distance between each pixel in the profile (the "velocity step" in km s^{-1}) is estimated and adjusted to provide the best resolution of the profile. The codes used in this thesis are described in Donati et al. (1997).

The line mask used to create the LSD profiles for all three stars in this thesis was created from the ATLAS 9 Kurucz atomic data base (Kurucz & Bell, 1995). The line mask was created for an F8 star using lines with at least 40% line depth and excluding very broad lines such as Ca HK and Hα lines. Figure 3.1.3 is an LSD profile of a set of observations taken for HIP 71933 at Epoch 2009.26. The three graphs in the figure are produced from a set of four exposures which recover thousands of absorption lines from the star's photosphere. The top graph is the Stokes V profile of these exposure. The middle graph is the null profile and the bottom graph is the Stokes I intensity profile.

3.2 Doppler and Zeeman Doppler Imaging

Dark spots on the surface of a star distort spectral lines in a way that can be recorded with a high-resolution spectrograph. Doppler Imaging (DI) is a method to record this distortion and through reverse analysis map the surface brightness of a star as it rotates (Vogt & Penrod, 1983). Zeeman-Doppler Imaging (ZDI) is a variation of DI in which the telescope measures the intensity and polarisation of the light to create the magnetic field topology on the star's surface (Semel, 1989).

3.2.1 Doppler Imaging

The basis of DI is to take a predicted spectrum of a star of a specific spectral type calculated as a gaussian function of the spotless star created from a published spectral line reference. This is compared to the spectra obtained from an observation of the star. The change in the predicted spectrum is iteratively reduced as close as can be done within the error margins of the observation.

This can be represented mathematically as:

$$E = \sum_{\phi} \sum_{\lambda} \frac{1}{\sigma^2{}_{\lambda,\phi}} [R_{calc}(\lambda, \phi) - R_{obs}(\lambda, \phi)]^2 + \alpha f \tag{3.2.1}$$

Where R_{calc} represents the calculated line spectrum and R_{obs} is the observed spectrum. The squared difference is summed over all wavelengths λ and the observations are spaced throughout the full set of phases ϕ of the star's rotation (Rice, 2002). The last term αf is the Lagragian multiplier α multiplied against a function f represents a regulating function designed to prevent the error "E" from calculating a match between the projected spectral fits against the observed spectra to a level below any measured errors or noise in the observation process. Without such a regulating function brightness images can be produced with more detail than can be justified from the observational data.

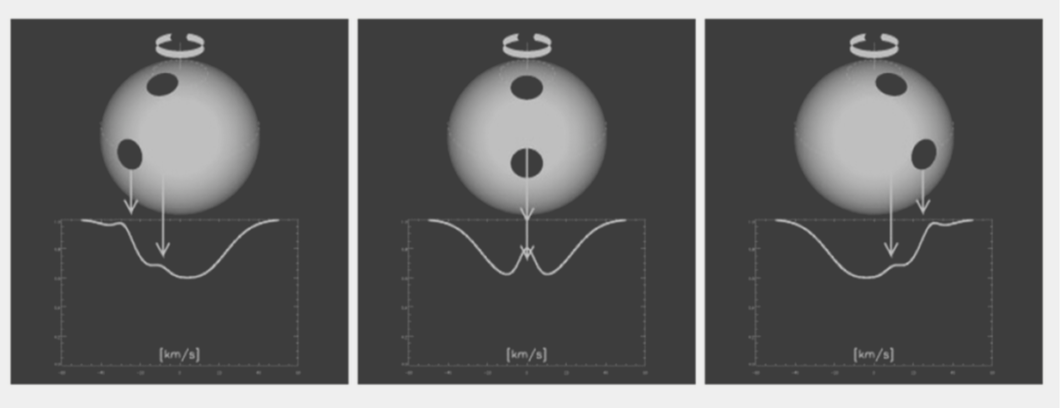

Figure 3.2.1: The spots on the surface of a star will create a "bump" in the spectra. The exact shape of this distortion is different depending upon where the spot is latitudinally or longitudinally on the surface. Image taken from Rice (2002).

Equation 3.2.1 can be seen as a χ^2 minimization with an added regulation function to prevent overfitting the observed data. It can therefore be simplified as:

$$E = \chi^2 + \alpha f \tag{3.2.2}$$

The regulating function f is often a maximum entropy function designed to drive the solution to a value by ignoring information in the observation that would push the solution away from the mean. This results in selecting a model which contains the maximum entropy and thus resist overfitting the model to the available data (our spectral line observations). This function is modulated by a Lagrangian multipler α to push the regulating function to just fit to the error in the data (error coming from photon noise and any other instrumental error) (Rice, 2002). The quality of the resulting model is reduced by a measure of the entropy in the data, which results in a model that is more likely to be truthful. If the quality of the data is very high, such as observations of a bright star with a high signal to noise ratio (SNR) then the regulating function becomes less influential and the DI process is essentially a χ^2 minimization of the data to a proposed model. There have been other regulating functions used in the DI and ZDI process, some of which simply work to smooth the χ^2 minimization (Kochukhov et al., 2010). Berdyugina (1998) discusses the Occamian approach developed by Terebizh & Biryukov (1994), which is based upon the idea of Occam's razor and involves determining a Fisher matrix to define an error ellipsoid of the inverse calculations. This technique has been used to generate surface images for several stars (Berdyugina, 1998; Järvinen et al., 2008, 2015). One problem with this is that any procedure based upon Occam's razor might smooth or eliminate genuine features of a system, simply because the correct solution is not always the easiest one (Einstein, 1921; Le Cunnf, 2004). Rice (2002) states that the choice of regulating function becomes less important as the quality of the data improves and believes that the maximum entropy method is superior for small cool stars because of the sometimes sparse and noisy data. The maximum entropy regulation is used for this thesis and the algorithm is detailed in (Skilling & Bryan, 1984).

3.2.2 Zeeman-Doppler Imaging

Early efforts to measure stellar magnetic fields using Zeeman analyzers resulted in the detection of the magnetic fields across longitudinal strips of the stellar disk. This is because the line of sight of a star's magnetic field is in the direction of the field, we see the longitudinal Zeeman effect on the spectra (Borra et al., 1984). This technique does not allow for the recovery of any horizontal component of the magnetic field. There are also multiple contributions to a Zeeman effect on individual spectra which are difficult to separate. In order to correct this problem, Zeeman Doppler Imaging (ZDI) techniques developed starting in the late 1980s focus on the detection of polarised light (Semel, 1989; Brown et al., 1991; Donati et al., 1992). The effect of this light on the individual spectral lines can be a signature of the presence of the magnetic field. This technique requires high resolution spectrographic data of polarised light. From this light we can construct the magnetic field distribution on the star's surface due to the different Doppler shifts of the line profiles that are split by the Zeeman effect (Berdyugina, 2005). This provides the motivation to develop instrumentation that can detect the circularly polarised light from a star as described in Section 3.1.1. Once this is accomplished, how can the data sets of this circular polarised light recorded during observations be interpreted?

The reconstruction of the field assumes that the circular polarisation of each end of a flux line emerging from the photosphere of a star is opposite each other in polarity and separated from within the Stokes V profile by the Doppler effect caused by the rotation of the star (see Figure 3.2.2). The difference between the spots at each end produces an easily recognizable shape on the Stokes V line profile (see Figure 3.2.2 where the V_1 and the V_2 are shifted on the surface due to the Doppler effect and are at opposite polarity). This differential measurement can give us information about the line of sight component of the magnetic field in any of the spots on the star's surface (Semel, 1989). A reverse analysis of this distortion of the star's spectral lines will require an estimate of the star's rotation, and because of this will make it difficult to separate differences between nearby spots. However it should be possible to recover details about the large-scale topology of the magnetic field. This is the sum of the poloidal, toroidal and meridional component of the magnetic field on the sphere of the star.

The combined effects of dipolar spot pairs on a star's surface will be the strongest data used to recover the magnetic field topology. However, not all of the magnetic features on a star's surface will be dipodal pairs. Young fast rotating stars in particular will be expected to include complex magnetic features including multipole and mixed polarity regions. ZDI techniques must be able to recover magnetic field values by including interpretation of subtle features in the Stokes V spectral lines (Donati & Brown, 1997).

With DI, the brightness components on the star are directly modeled, however with ZDI the magnetic field will be modeled with spherical harmonic expansion coefficients $\alpha_{l,m}$, $\beta_{l,m}$ and $\gamma_{l,m}$ calculated for a fixed number of elements of the stellar disk where the field components are:

α = the radial poloidal component
β = the horizontal poloidal component
γ = the horizontal toroidal component

The l shell is the angular degree of the magnetic field and m-shell is the azimuthal order

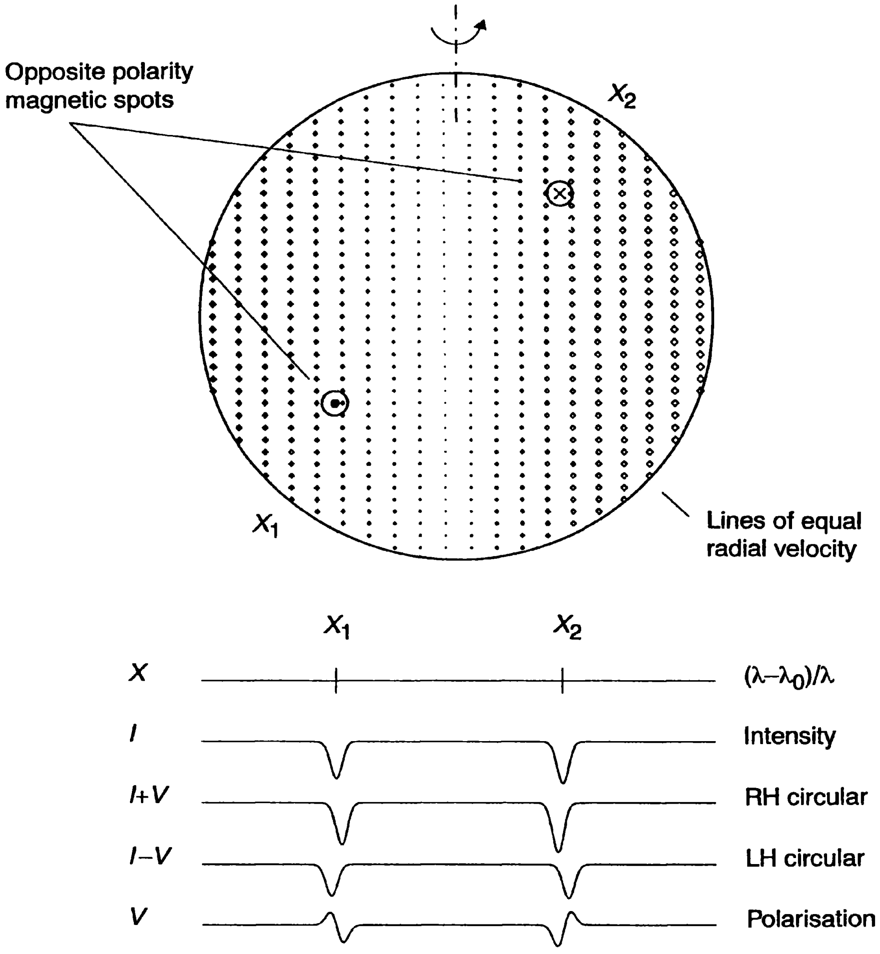

Figure 3.2.2: Principles of Zeeman Doppler Imaging taken from Carter et al. (1996). The dipolar pair of spots on the surface causes the Stokes V signature to be shifted due to the Doppler effect caused by the star's rotation. The observed spectral line profiles are different at different places on the star's surface because they are Doppler shifted due to the star's rotation.

of the mode. The magnetic field strength of the star is stored in different l shells at different scales; $l = 1$ dipole, $l = 2$ quadrupole and $l = 3$ octopole and so on. Several ZDI observations have been performed using this method and found that most of the star's field energy is stored in l values ≤ 6 (Hackman et al., 2016; Lehtinen et al., 2019; Willamo et al., 2022). It has long been known that the Sun's magnetic field strength is mostly dipolar, with the magnetic field strength stored in the lower l shells, with more complexity appearing during solar maximums (Babcock et al., 1955; Sanderson et al., 2003; Wang, 2005).

These complex coefficents for the magnetic field are calculated from an iterative fit to the observed LSD profiles. This procedure is described in more detail in (Donati et al., 2006). This technique of recovering the magnetic field components from specific points on the stellar surface combined with a Maximum Entropy regulation is how it is possible to produce the magnetic field topology from a complex Stokes V signature that was recorded using a spectropolarimeter.

The codes used in this thesis to perform the DI and ZDI computations were developed by J. -F Donati and P. Petit. The methodology is described in (Donati & Brown, 1997).

3.3 Instrumental resolution, seeing conditions and phase coverage

The recovery of star spots using DI is affected by the latitude of the spots and the star's inclination. The key factors that affect the recovery of spot features is the spectrograph resolution, the SNR and the $v\sin i$ of the star as well as the phase coverage of the observations.

For a best image of a star, line profiles should be evenly spaced. A minimum of 8-10 observations should be spaced proportionally as possible around the star through its rotational phase (Vogt et al., 1987). For high-inclination stars, limited phase coverage will result in poorer recovery of lower-latitude features.

Finally overall seeing conditions, especially the existence of cloud cover will degrade the quality of the spectral lines that are the basis for all DI and ZDI calculations. For the three stars analysed in this thesis, there is a range of data, with the least data for VXR 77A and the best data for HIP 71933.

3.3.1 Differential Rotation

The discovery that the Sun rotates differentially is often credited to Robert Carrington who recorded the suns rotation based upon latitude in 1853. He recorded the first known solar rotation which is defined as solar cycle 1 starting in November 1853 (Carrington, 2021). Later research by Arlt et al. (2016) and others reveals that Christoph Scheiner noticed the Sun's DR much earlier in a series of observations from 1611 to 1631 (Scheinero, 1651). The Scheiner data consists of sketches of sunspots just prior to the first known Maunder minimum.

From the NASA SOHO satellite data we know that the Sun rotates approximately once every 25 days at the equator and longer at the poles, approximately once every 35 days (NASA, 2020b). This DR can be modelled with the following simplified equation:

$$\Omega(\theta) = \Omega_{eq} - d\Omega sin^2\theta \tag{3.3.1}$$

where $\Omega(\theta)$ is the rotation rate at latitude θ in rad d^{-1}, Ω_{eq} is the equatorial rotation rate in rad $d^{-1}$and dΩ is the rotational shear between the equator and the poles (the DR in rad d^{-1}).

The DR of young solar-type stars is an important parameter to determine because it is thought to play a critical role in the formation of a star's magnetic field. The comparison of DR values for different stars becomes a key factor to understand how the dynamo processes evolve. DR is difficult to measure because the accuracy of the data collected is dependent upon several parameters, including the number of observations, phase coverage and the resolution of the spectra. There must be a good distribution of spots from the observable pole down to the stellar equator along with a sufficient observation period to see how the spot movement evolves over time. Without a high quality of this data it will be difficult for the analysis to converge on a set of values.

Several methods have been used to attempt to measure DR of distant stars, including precision photometry (Frölich et al., 2012), analysis of the shape and amplitude of light curves (Messina & Guinan, 2003), spectroscopy (Reiners & Schmitt, 2003; Reiners, 2006; Ammler-von Eiff & Reiners, 2012), and analysis of successive DI brightness maps (Donati & Cameron, 1997; Petit et al., 2002; Barnes et al., 2005) (see discussion (Waite, 2013)).

The technique used in this study was developed by Donati et al. (2000a) and utilizes the solar-like differential law from Equation 3.3.1 and the χ^2 minimization technique in the imaging process. This method was found to produce a DR magnitude to within reasonable agreement with the other methods. It produces a paraboloid of Ω_{eq} vs dΩ values with the best χ^2 at the center. The DR is considered in the Doppler imaging inversion and maximum entropy process. The technique is described in (Petit et al., 2002). This approach can be done using Stokes *I* brightness features or Stokes *V* magnetic features. The resolution of a star's DR from these two sources does not always result in equal or even similar values. This difference is interpreted as representation of an important property of the surface feature of a star; namely that the magnetic regions of a star are not anchored at the same depth in the convection zone as the brightness features, and do not experience the same shear values (Donat et al., 2003; Waite, 2013).

The codes to perform this calculation were provided by the authors of the technique in (Petit et al., 2002). A map is created for each combination of Ω_{eq} and dΩ. A paraboloid is produced with the best χ^2 values in the center. An even distribution of spots from the equator to pole is needed to produce a distinct paraboloid. Observations should be evenly space throughout the star's rotational phase, and with high resolution sufficient to show shifts in spot movement. This process was run in parallel on the computer with multiple cores by subdividing the longitudinal strips where the Ω_{eq} and dΩ are calculated and then adding the outputs together in sequence to produce a final map file. As with the DI-ZDI computational scripts, a series of PERL scripts to automate this process were also created and are described in Appendix C.3.

4 OBSERVATIONS

Three young late-F stars were selected for study by this thesis. VXR 77A (V380 Vel)(~27 Myr) is in the cluster IC 2391 in the Vela constellation (Randich et al., 2001). It is classfied as an F8V (Torres et al., 2006). HD 43989 (V1358Ori) (~28 Myr) is in the Columba association (Zuckerman et al., 2011; Kriskovics et al., 2019) and is classifed as F9V (Montes et al., 2001; McDonald et al., 2012). (Torres et al., 2006). HIP 71933 (HD 129181)(~15 Myr) is classified F8V (Torres et al., 2006). Of the three stars, HD 43989 has the most prior DI and ZDI observations in the literature, with less observational data for the other two. HD 43989 is the only young late -F star known to have a magnetic cycle.

4.1 Instrumentation

The data sets for the stars in this thesis were collected from four telescopes. Two of these are at Siding Spring Observatory located near Coonabarabaran, New South Wales in Australia. Epochs 2012.04, 2018.07 and 2018.72 for VXR 77A, epochs 2009.34, 2010.33, 2012.26, 2018.07 and epoch 2019.46 for HIP 71933 were collected using the 2.3-meter telescope owned by the Australian National University (ANU). The echelle spectrograph attached to this telescope has a resolution R of ~24,000. This spectrograph is mounted on the telescope at the Nasymuth focus and moves while the telescope is tracking (see (Burton, 2013) for a description). Stokes *I* data only was recorded. Epochs 2003.92 and 2005.09 for VXR 77A, epoch 2008.94 for HD 43989 and epoch 2009.26 for HIP 71933 were recorded at the AAT using the University College London Echelle Spectrograph (UCLES) combined with a visiting instrument (SEMPOL) named after one of the founders of ZDI, the late Dr. Meir Semel (Semel, 1989). This combination produced a spectropolarimeter with a resolution of ~70,000. The UCLES spectrograph has been decommissioned at the AAT since January 2018 and replaced with spectrographs, HERMES and Veloce. These observations were made by various astronomers, including graduate students under supervision, for the purpose of collecting data for future analysis. The observers (where known) who collected the data for each observing run are listed in Tables with the observing log data (Tables 4.2.1, 4.3.1 and 4.4.1).

Epoch 2019.06 for HD 43989 was recorded at the Télescope Bernard Lyot (TBL) located at the Pic du Midi observatory in France. This telescope is managed by the Observatoire Midi Pyrénées. Observations for this thesis were made with a spectropolarimeter Narval, with a resolution of ~65,000, which has been subsequently upgraded to Neo-Narval with the same resolution.

Epoch 2011.37 for HIP 71933 was recorded by the 3.6-meter telescope at La Silla observatory near La Serena, Coquimbo, Chile, using the spectropolarimeter HARPSpol. This instrument includes a demountable polarimeter to produce a spectropolarimeter with a resolution of ~115,000.

4.2 VXR77A

4.2.1 Observations Overview

Two telescopes were used to obtain five epochs of VXR 77A observations over a period of 15 years, from 2003 to 2018 (see Table 4.2.1). Epochs 2003.92 and 2005.09 were recorded using the AAT and UCLES/SEMPOL spectropolarimeter during December 2003

Table 4.2.1: Log of spectroscopic observations for all epochs for VXR 77A (V380 Vel). Column 1 lists the observation epoch and column 2 lists the telescope. Column 3 lists the telescope's instrument resolution. Date, start time and end time for exposures are in columns 4, 5 and 6, with the number of usable exposures in column 7. The last column lists the rotational cycles starting with the first exposure of the first epoch to the last exposure of the last epoch.

Epoch	Telescope	Instrument Resolution	Date	UT Start	UT End	No. of Stokes I exposures	Observer(s)	Rotational Cycle
2003.92	AAT	~70,000	2003 Dec 07	13:54	17:08	15	B. Carter, S. Marsden, M. Semel	-1.700 to 1.734
			2003 Dec 08	13:09	14:38	8	J. Barnes, B. Carter, S. Marsden, D. Reese, M. Semel	
			2003 Dec 09	12:05	17:47	16	B. Carter, S. Marsden, M. Semel	
2005.09	AAT	~70,000	2005 Feb 04	09:53	18:38	42	C. Brown, B. Carter, S. Marsden ,	-6.307 to 3.438
			2005 Feb 05	10:04	18:37	43	C. Brown, B. Carter, S. Marsden	
			2005 Feb 08	12:34	15:35	17	B. Carter, J. -F. Donati, S. Jeffers, S. Marsden, I. Waite	
			2005 Feb 09	14:47	18:07	16	B. Carter, J. -F. Donati, S. Jeffers, S. Marsden, I. Waite	
			2005 Feb 10	14:36	18:33	14	B. Carter, J. -F. Donati, S. Jeffers, S. Marsden, I. Waite	
2012.04	2.3-m	~24,000	2012 Jan 11	15:10	16:19	2	D. Burton	-1.45 to 2.27
			2012 Jan 12	13:31	17:34	6	D. Burton	
2018.07	2.3-m	~24,000	2018 Jan 25	14:40	17:42	6	I. Waite	-4.687 to 4.473
			2018 Jan26	11:48	17:58	7	I. Waite	
			2018 Jan28	15:50	18:25	5	I. Waite	
			2018 Jan29	10:23	18:25	10	I. Waite	
			2018 Jan31	12:26	114:04	4	I. Waite	
2018.72	2.3-m	~24,000	2018 Sep 19	17:34	19:05	6	S. Marsden	-0.0814 to 1.537
			2018 Sep 20	18:53	19:08	8	S. Marsden	

and February 2005. During epoch 2003.92 seeing conditions were poor due to overcast skies and although observations were taken in polarimetric mode no magnetic detections were obtained. Stokes *I* data were able to be recovered during this epoch. The step size of the LSD profile had to be increased to reduce the noise. The remaining epochs were observed using the 2.3-m telescope where only Stokes *I* data was recorded. VXR 77A has a V magnitude of approximately 9.65 (Gaia et al., 2020) which makes the recovery of magnetic information more difficult.

The observation epochs in Table 4.2.1 cover sufficient time to provide full-phase coverage of VXR 77A given the rotation period of 0.653 d (see Table 4.2.2).

The rotational phase was computed using the ephemeris:

$$\mathrm{JD} = 2453982.1069 + 0.653\phi \tag{4.2.1}$$

where JD is the julian date of the observation and ϕ is the rotational phase. The zero point of the first epoch was arbitrarily chosen to be the middle of the epoch. An integer number of rotations are added to this zero point to estimate the zero point of the next epoch The zero point chosen for that epoch is the JD which is closest to the previously calculated value.

4.2.2 Stellar Parameters

Table 4.2.2: Fundamental parameters for VXR 77A (V380 Vel, Gaia DR2 5905397139423601792).

Parameter	Value
Classification[4]	F8V
Right Ascension[1]	$8^h\ 45^m\ 39^s$
Declination[1]	$-52°25^m\ 59.16^s$
Distance[1]	153 ± 0.99 pc
Luminosity[1]	$2.139 \pm 0.021\ L_\odot$
Radius (R)[1]	$1.28 \pm 1.33\ R_\odot$
V magnitude [1]	9.65
Mass [2]	$\sim 1.21\ M_\odot$
Age[2]	~27 Myr
Photospheric temperature (T_P)[1]	6163 ± 160 K
Spot temperature (T_S)[3]	3883 ± 50 K
Photosphere-Spot difference[3]	2280 ± 50 K
$v$sin$i$[5]	$92^{+2.5}_{-1.3}$ km s^{-1}
Inclination angle[5]	60°± 10°
Calculated Inclination angle[5]	67.95°
Rotational period[5]	0.653 ± 0.05 days
Rotation rate at equator (Ω)[5]	10.19 ± 0.05 rad d^{-1}
Rotational shear ($d\Omega$)[5]	$0.645^{+0.02}_{-0.1}$ rad d^{-1}

[1] Gaia et al. (2016, 2018, 2020)
[2] Baraffe et al. (2015) (see Figure 4.2.1)
[3] Berdyugina (2005)
[4] Torres et al. (2006)
[5] This study

Fundamental parameters for VXR 77A are listed in Table 4.2.2. The spectral classification is taken from (Torres et al., 2006). Most of the other parameters were obtained from the ESA's Gaia space mission and the remaining were derived from this study as described in Sections 3.2.1 and 3.2.2.

A distance of 153 ± 0.99 pc was calculated from a Gaia measured parallax 6.53 ± 0.03 mas (Gaia et al., 2020), which also measured luminosity to be $2.139 \pm 0.021\ L_\odot$. and photospheric temperature of 6163 ± 160 K (Gaia et al., 2018). Data from Berdyugina (2005) is used to obtain photospheric-spot temperature difference of different spectral types (see Figure 7 in (Berdyugina, 2005)). From this plot is estimated a photospheric-spot difference of 2280 ± 50 K for VXR 77A . This produces a spot temperature of 3883 ± 50 K. The Gaia DR2 release reports of radius of $1.28 \pm 1.33\ R_\odot$ (Gaia et al., 2018). Where multiple values of a parameter have been recorded Gaia values have been listed as Gaia measurements are more recent and arguably using better instrumentation.

Using the above values of luminosity and surface temperature, VXR 77A can be placed on a plot of stellar atmospheric models developed by (Baraffe et al., 2015) (see Figure 4.2.1). From this plot a mass of $\sim 1.21\ M_\odot$ and an age of ~27 Myr are estimated. This fits within an estimated age of IC 2391 at ~36 Myr reported by (Hirshfeld et al., 2000) and ~46 Myr reported by (Barrado et al., 2001).

Stellar parameters for VXR 77A were derived by varying them to achieve a minimum χ^2 , using the Stokes I data as described in Section 3.2.1. These include $v$sin$i$, radial velocity

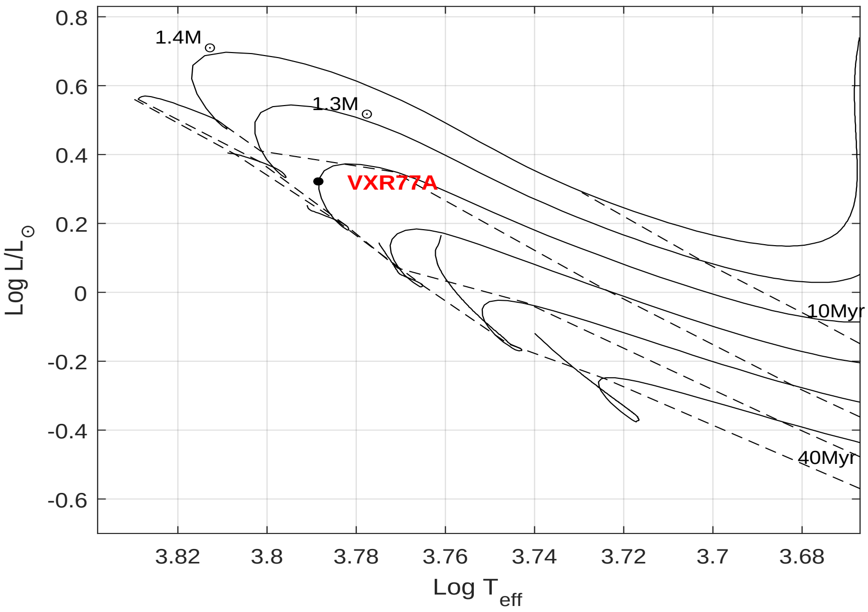

Figure 4.2.1: Age and Mass of VXR 77A. Surface temperature and luminosity for VXR 77A were obtained from the Gaia DR 2 release (Gaia et al., 2018) and are plotted in an HR diagram of 0.9 to 1.4 M$_\odot$ in 0.1 M$_\odot$ increments against evolutionary track models provided by Baraffe et al. (2015). Stellar ages of 10, 20, 30 and 40 Myr are overlayed as isochrones. From this plot an age of ~27 Myr and a mass of ~1.21 M$_\odot$ for VXR 77A is obtained.

(RV), inclination, and rotational period (P$_{rot}$). The $v\sin i$ derived in this study is 92 $^{+2.5}_{-1.3}$ km s^{-1}, very close to a value of 95 km s^{-1} reported by Marsden et al. (2005). Figure 4.2.2 shows three plots of the inclination angle varied by one degree increments and the χ^2 value determined. Only three of the five epochs were charted this way because the phase coverage of the excluded two epochs (2012.04 and 2018.72) was considered insufficient. Even with the best phase coverage, the three results are not in close agreement probably because of the limited number of exposures for all but the best observation, which is Epoch 2005.09. The inclination value derived for this epoch has been chosen as the best likely value, because of the superior quality and quantity of data and because it is the closest match to a calculated value of 67.95°based upon Gaia radius and the measured $v\sin i$. The rotational period determined is 0.653 ± 0.05 days, close to the value of 0.65 days reported by (Yamashita et al., 2022). RV values derived are shown in Table 4.2.3. They are slightly lower than a value of 16.46 km s^{-1} reported in the Gaia DR3 early release (Gaia et al., 2022). Error margins are higher for the 2.3-m telescope than the AAT.

The ATLAS 9 Kurucz atomic data base was used for the line mask (Kurucz & Bell, 1995). Step sizes used to create the LSD profiles varied with the telescope instrumentation. For all observations at the AAT a step value of 1.7 km s^{-1}is normally used. Exceptions were made for the AAT Epoch 2003.92 observation where the step size was increased to double the value (3.4 km s^{-1}) in order to smooth over noisy data. A value of 3.36 km s^{-1}was used for the AAT Epoch 2005.09 because the CCD pixels were binned by two in the spectral direction. A value of 4.2 km s^{-1}was used for all observations using the 2.3-m telescope (Epochs 2012.04, 2018.07 and 2018.72). The total number of spectral lines in each exposure used to create an LSD profile was between 2076 and 2195 for the AAT and between 3065

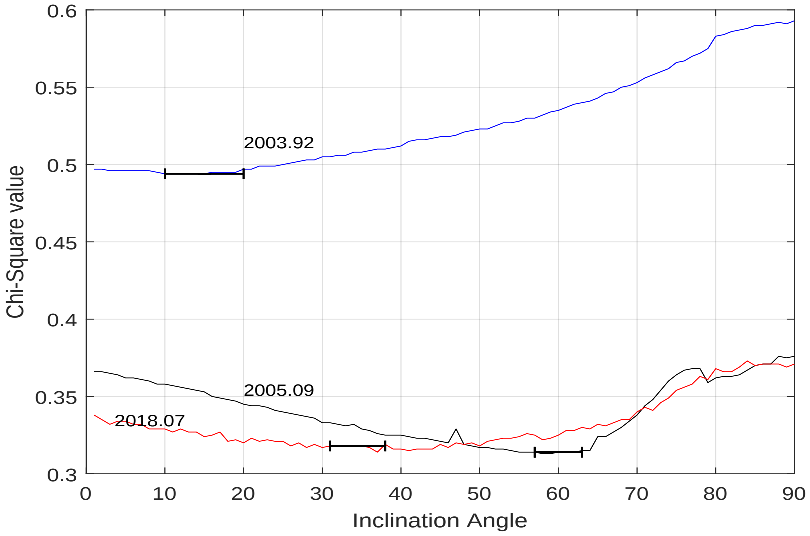

Figure 4.2.2: Inclination angle analysis for VXR 77A. A minimum χ^2 value was obtained by changing the inclination angle by 10° increments for each epoch. Epochs 2012.04 and 2018.72 were not plotted due to poor phase coverage. An error bar is placed in each graph to show where the inclination value starts to change for higher χ^2 values. The inclination angles for each epoch are not consistent and Epoch 2005.09 is selected as the most probable true inclination because of the higher quality of the data set. From this plot an inclination of ~60° is observed. This value is also closest to a calculated value of inclination from the Gaia radius and $v\sin i$ value derived in this study as discussed in Section 4.2.2.

and 3096 for the 2.3-m telescope..

4.2.3 Results

Stokes *I* Image Reconstruction Using the LSD profiles created from procedures described in Section 3.1.2 (see maximum entropy fit maps in Figures A.1.1 through A.1.5) surface brightness maps are created using procedures described in Section 3.2.1 (see Figure 4.2.3). Stokes *V* data was collected for epoch 2003.92, however the seeing conditions for this epoch were so poor that any magnetic information derived was considered unrelable. There are therefore no magnetic maps shown for any of the epochs of VXR 77A. All remaining epochs are Stokes *I* data only. In all of these observations the largest density of spots are seen in the polar region. This is most evident in the epoch 2005.09 data. The data from the other epochs is not as reliable but continue to show the majority of spots at the visible pole down to the +30°latitude. The density of the polar spots in all the epochs and especially the best data set (Epoch 2005.09) is consistent with other results of young solar-like stars (see overview in Section 2). Mapping codes used to create these maps are described in Section 3.2.

Spots and Latitude Distribution Distribution of spots across the latitudes of the stellar surface can be expressed in terms of fractional spottedness and displayed per the equation:

$$F(\theta) = \frac{S(\theta)cos(\theta)d\theta}{2} \tag{4.2.2}$$

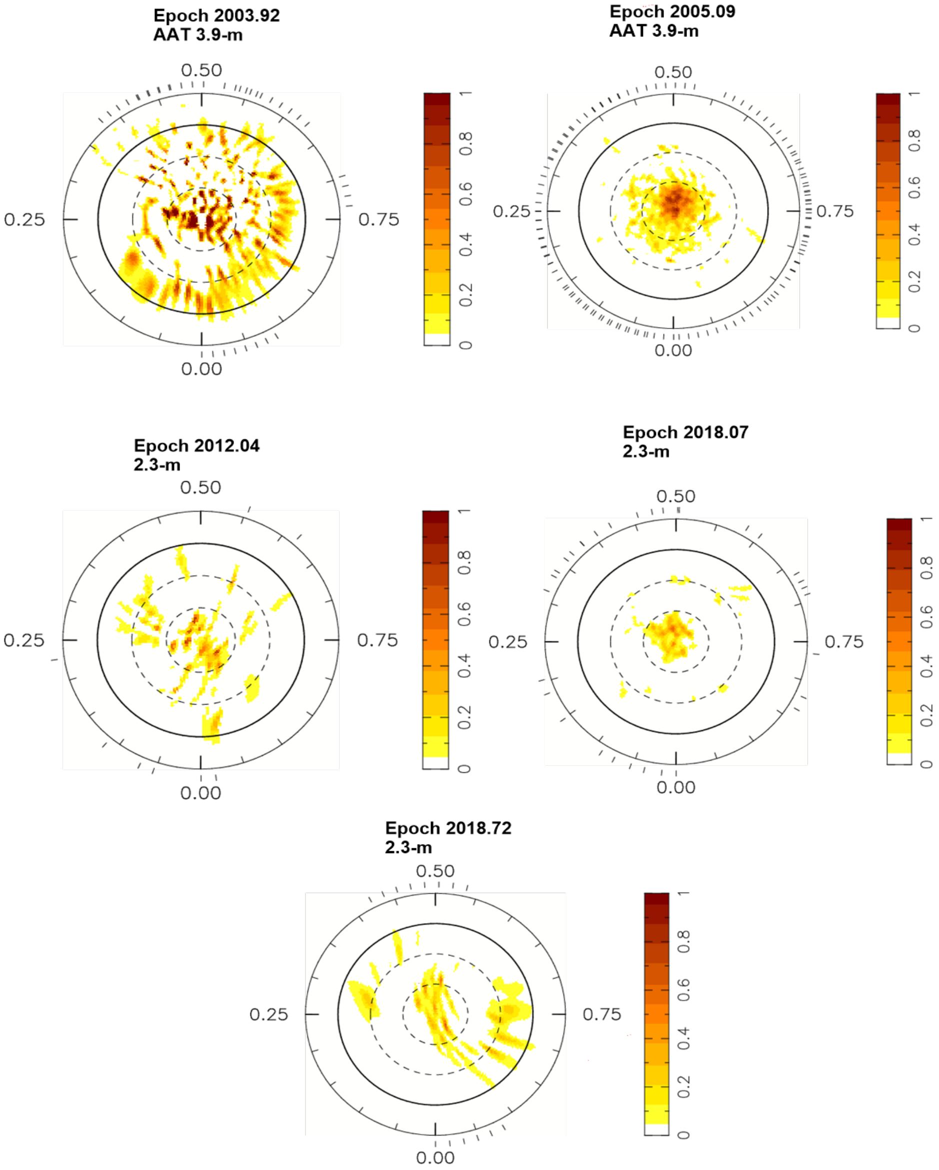

Figure 4.2.3: DI brightness maps for VXR 77A for all epochs. The images are flattened polar projections extending down to a latitude of -30°. The dashed lines are +30°and +60°latitudes and the bold line is the equator. The radial ticks are the rotational phases at which VXR 77A was observed. The scale bar on the right represents a normalized weight of spot density with zero representing no spots and 1 representing highest spot density. All maps were calculated including DR values derived from the DI analysis. The epochs with the best rotational phase coverage are 2005.09 and 2018.07. These images show denser spot coverage at the visible pole consistent with observations of other young solar-type stars. The other three epochs (2003.92, 2012.04 and 2018.72) were created under poorer seeing conditions and rotational phase coverage but also show denser spot coverage at the pole.

where S(θ) is the average spot occupancy at a given latitude θ and dθ is the width of each latitude ring. This is graphically shown in Figure 4.2.4. This diagram a quantitative measure of the spot coverage on the star's surface. Similar plots have been made for other stars including HD 307938 (G2V) (Marsden et al., 2005), HD 35296 (F8V) and HD 29615 (G3V) (Waite et al., 2015), HIP 89829 (G5V) (Perugini et al., 2021) and HD 171488 (Brown et al., 2024). This plot is useful to see the distribution of spots across epochs against each other and provides more visual information concerning evolution of spots. For VXR 77A, all epochs show an increase in spots at high latitude with the most spots in the polar region. This is consistent with the previously mentioned solar-type stars which show high latitude spots and prominent spot features at the poles. This plot also shows the highest polar spot density for Epoch 2005.09 which is the epoch with the best observational data.

Differential Rotation DR parameters were derived per procedures and limitations discussed in Section 5.2. This resulted in a χ^2 convergence of the differential shear for the 2005.09 epoch only and resulted in a less than perfect paraboloid (see Figure 4.2.5). The values obtained from this plot are Ω_{eq} = 10.19 ± 0.05 rad d^{-1}and dΩ = 0.645 ± 0.03 rad d^{-1}. These values when incorporated into the DI analysis reduced the χ^2 value only slightly. The variance crosses fit reasonably close to the centered values except for the upper and lower values for $v\sin i$, which are more sensitive to change than the other parameters in the DI analysis. These crosses appear off the paraboloid in the upper part of the ellipse enclosing the variances. The poor shape of the paraboloid in Figure 4.2.5 make the DR values recovered tentative at best.

The differential shear derived for VXR 77A (if correct) place it in the higher realms of the young solar-type stars discussed in the Literature Review Section 2. This comparison along with the other two stars in this thesis are discussed in more detail in the discussion Section 5.

Radial Velocity Radial velocity values resulting from the DI analysis result in a variation between 13.5 ± 0.1 km s^{-1}to 14.7 ± 1.0 km s^{-1}(see Table 4.2.3). This compares to a value of 16.46 km s^{-1}from the Gaia DR 3 release (Gaia et al., 2022). The observations show a variation in RV values, but are too separated in time to confirm the existence of a companion. Provided that the LSD signature is large enough and there is sufficient velocity space, secondary stars can be seen in the LSD profiles (Marsden et al., 2005; Lavail et al., 2020; Lehmann et al., 2020; Marsden et al., 2023). There is no evidence of a secondary in the LSD profiles for VXR 77A (see appendix Figures A.1.2 through A.1.5) although a small secondary might exist but undetectable in the LSD profile. RV values versus observation epoch are plotted in Figure 4.2.6. Despite the lack of a visible companion in the LSD profiles, these values might still indicate a stellar reflex caused by a companion. Even if this is the case, this is not expected to affect the mapping results in any significant way.

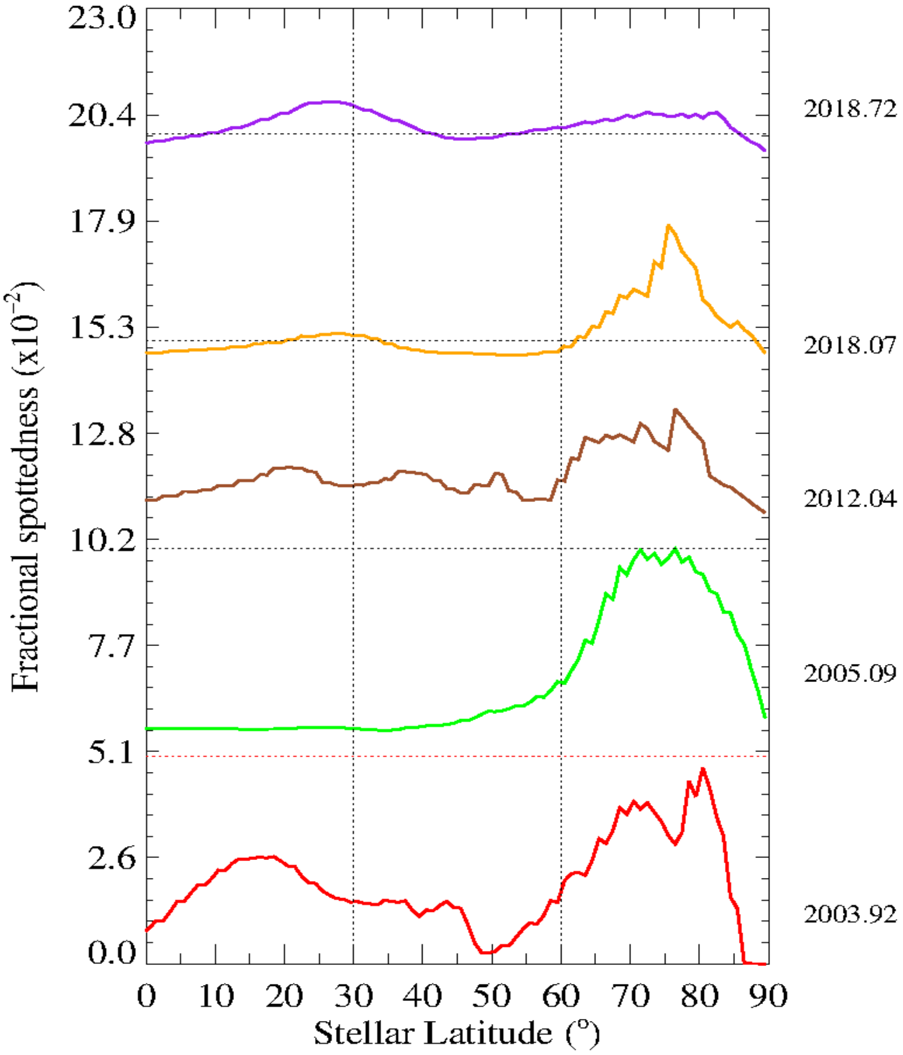

Figure 4.2.4: VXR 77A fractional spottedness by latitude for all epochs. Fractional spottedness is defined by Equation 4.2.2 and is the average instance of spots at each latitude. Each epoch is shifted up for graphing purposes. Each epoch shows a peak at near 90°latitude where the most spots occurs with the heaviest spots at polar or near-polar region. This feature is prominent throughout the epochs even though data quality and phase coverage vary for each epoch. These features are consistent with spot latitude distributions seen in other young solar-type stars.

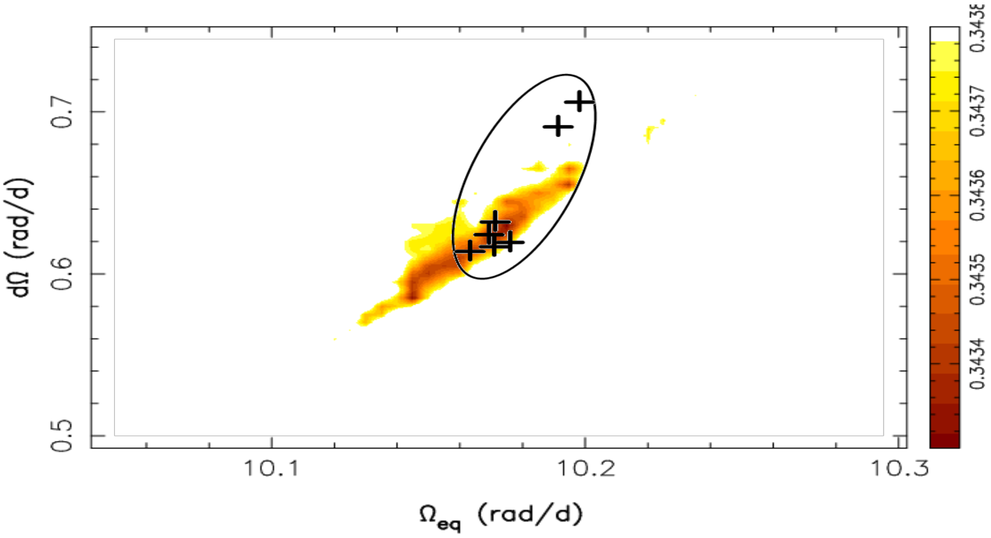

Figure 4.2.5: DR measurement for VXR 77A epoch 2005.09. Values of $d\Omega$ versus Ω_{eq} are plotted to form a paraboloid (yellow-brown area of the plot) with the best χ^2 value at the darkest area in the center. 1σ variances are generated by changing the inclination by 10°, $v\sin i$ by -1.3 km $s^{-1}$to 2.5 km $s^{-1}$and the maximum entropy spot aim by ± 5 percent. The values shown are crosses which are within the ellipse.

Table 4.2.3: Data derived from the DI analysis for VXR 77A. The observation epoch is in column 1. The total number of usable Stokes *I* exposures is in column 2. Column 3 is the SNR for each exposure. Percent spot coverage across the stellar surface is in column 4. RV values are in column 5. By plotting RV values against decreasing χ^2 values an error of 0.1 km $s^{-1}$is estimated for the AAT and 1.0 km $s^{-1}$for the 2.3-m telescope.

Epoch	No. of Exposures	LSD SNR	Spot Percentage	RV (km s^{-1}) Values
2003.92	39	725	5.8	13.5 ± 0.1
2005.09	132	1023	2.6	14.1 ± 0.1
2012.04	8	750	1.43	14.7 ± 1.0
2018.07	32	749	0.83	13.2 ± 1.0
2018.72	14	764	1.6	14.1 ± 1.0

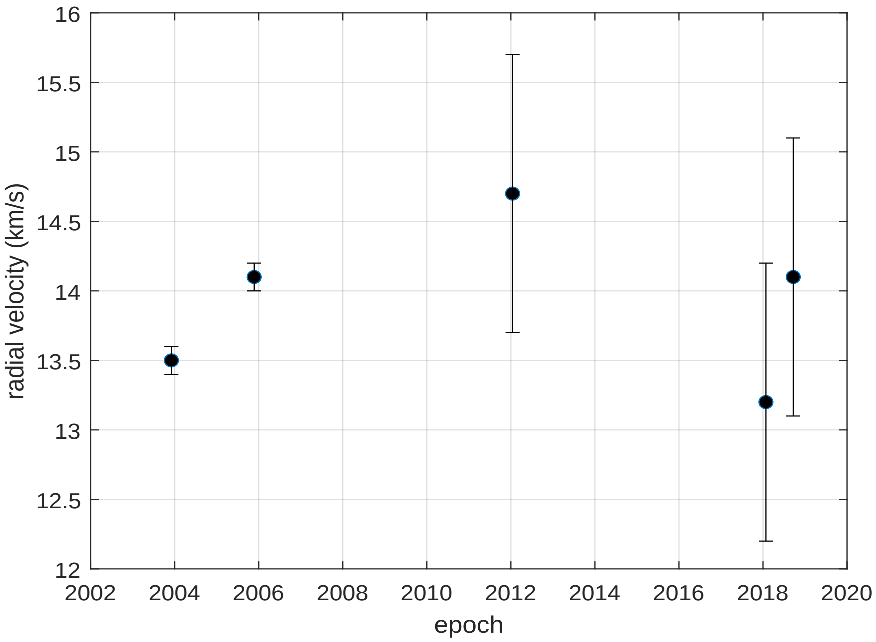

Figure 4.2.6: Radial Velocity (RV) values plotted over time for all epochs for VXR 77A. Error bars were obtained from RV values derived with decreasing χ^2. RV errors for Epoch 2003.92 and 2005.09 are less because of the superior resolution of the AAT versus the 2.3-m telescope. The number of data points is insufficient to identify a companion but the variations in RV values could indicate a stellar reflex caused by a companion.

4.2.4 VXR 77A TESS Photometric Comparisons

Additional photometric data for VXR 77A was obtained from the Transiting Exoplanet Survey Satellite (TESS) observations using the data portal at the Mukulski Archive for Space Telescopes (MAST) (STSCI, 2024). This data is shown in Figure 4.2.7. These are light curve files for three observations made in 2019 and 2023 using Simple Aperture Photometry (SAP) by summing pixel brightness from a pre-selected aperture (TSSC, 2024). A periodogram of each curve shows a period of ~0.652 d for the top graph, sector 09, ~0.640 d for the middle graph, sector 62 and ~0.644 d for the bottom graph, sector 63. These values compare to ~0.653 d derived from the DI analysis (see Table 4.2.2). The rotation period calculated from the periodogram of the photometric curves below will be more heavily weighted at higher latitudes than the equatorial rotation period. It has been assumed that the differential rotation of young solar-type stars will be consistent with a solar-type rotation rate give in Equation 3.3.1, which predicts that the rotation periods at higher latitudes will be longer than that at the equator which is what has been estimated in the DI analysis. While this is not seen from these photometric curves for VXR 77A, the values obtained are still somewhat close to the rotation period previously derived. Further discussion of this is found in Section 5.1. Construction of the light curves as well as the analysis of the periodogram was done using the TESS data analysis tool lightkurve (Lightkurve Collaboration et al., 2018).

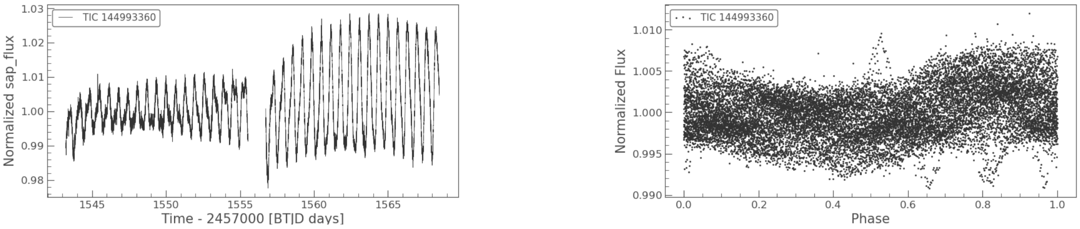

(a) Sector 09 2019 Light Curve, period ~0.652 d

(b) Sector 09 2019 Folded Light Curve

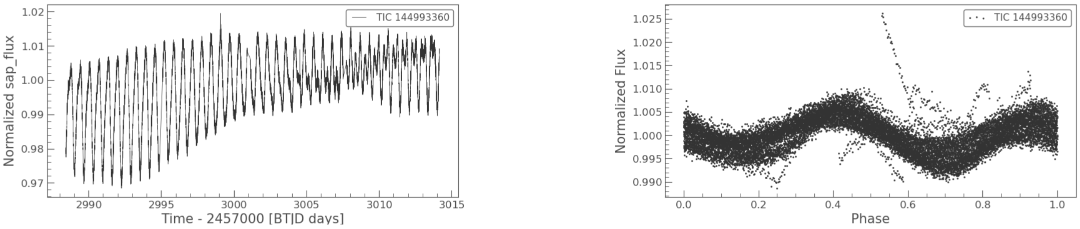

(c) Sector 62 2023 Light Curve, period ~0.640 d

(d) Sector 62 2023 Folded Light Curve

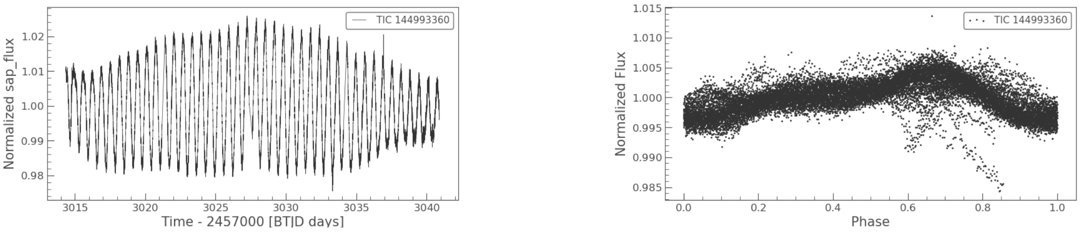

(e) Sector 63 2023 Light Curve, period ~0.653 d

(f) Sector 63 2023 Folded Light Curve

Figure 4.2.7: TESS photometric observations of VXR 77A made in 2019 and 2023. The period of these plots compares to a rotation period of 0.653 days derived from the DI analysis (see Table 4.2.2. The data described here may be obtained from the MAST portal. The TESS Identification Catalog ID is shown for each graph (see discussion in Section 4.2.4).

4.3 HD 43989 (V1358 Ori)

4.3.1 Observations Overview

Two telescopes were used to obtain two epochs of HD 43989 observations over a period of 10 years from late 2008 to 2019. Epoch 2008.94 was observed using the AAT, using the UCLES spectrograph and the SEMPOL polarimeter. Seeing conditions were good however the phase coverage for Epoch 2008.94 was poor. Stokes *I* and Stokes *V* data were recorded.

Epoch 2019.06 was recorded at the TBL telescope with the NARVAL spectropolarimeter. Stokes *I* and Stokes *V* data were recorded. Here also the seeing conditions were nominal with good phase coverage.

As with VXR 77A the observation epochs recorded in Table 4.3.1 are sufficient to provide full-phase coverage of HD 43989 given the rotation period of 1.167 d (see Table 4.3.2). As with VXR 77A, the zero point for all epochs are calculated as an integer number of rotations starting with the zerio point of the first epoch. The zero point chosen for the epoch is the JD which is closest to the previously calculated value.

The rotational phase was computed using the ephemeris:

$$JD = 2454814.155 + 1.167\phi \tag{4.3.1}$$

where JD is the observational data and ϕ is the rotational phase.

Table 4.3.1: Log of spectroscopic observations for all epochs for HD 43989. The first column lists the epoch of the observation and the second column lists the telescope. Columns arrangements are the same as for VXR 77A in Table 4.2.3.

Epoch	Telescope	Instrument Resolution	Date	UT Start	UT End	No. of Stokes I exposures	Observer(s)	Rotational Cycle
2008.94	AAT	~70,000	2008 Dec 08	15:29	17:53	8	D. Burton, B. Carter, E. Guggenberger, S. Marsden, K. Treschman, I. Waite	-5.005 to 3.574
			2008 Dec 09	14:23	18:00	7	D. Burton, B. Carter, E. Guggenberger, S. Marsden, K. Treschman, I. Waite	
			2008 Dec 10	13:47	18:08	8	D. Burton, B. Carter, E. Guggenberger, S. Marsden, K.. Treschman, I. Waite	
			2008 Dec 14	13:36	16:35	8	D. Burton, S. Marsden, M. Mengel, I. Waite	
			2008 Dec 15	12:34	17:30	12	S. Marsden, M. Mengel, I. Waite	
			2008 Dec 16	13:11	17:44	12	S. Marsden, M. Mengel, I. Waite	
			2008 Dec 17	11:18	16:42	11	S. Marsden, M. Mengel, I. Waite	
			2008 Dec 18	12:30	15:58	11	S. Marsden, M. Mengel, I. Waite	
2019.06	TBL	~65,000	2019 Jan 03	22:01	01:47	8	Service Observing TBL Staff	-3.60 to 8.61
			2019 Jan 04	21:32	02:06	8	Service Observing TBL Staff	
			2019 Jan 05	21:23	01:39	8	Service Observing TBL Staff	
			2019 Jan 06	21:44	01:58	8	Service Observing TBL Staff	
			2019 Jan 07	20:40	02:52	8	Service Observing TBL Staff	
			2019 Jan 12	20:41	02:09	8	Service Observing TBL Staff	
			2019 Jan 14	20:27	01:16	8	Service Observing TBL Staff	
			2019 Jan 05	19:49	01:31	8	Service Observing TBL Staff	

4.3.2 Stellar Parameters

Table 4.3.2: Fundamental parameters for HD 43989 (V1358Ori, Gaia DR2 3116883781327753216)

Parameter	Value
Classification[4]	F9V
Right Ascension[1]	$6^h\ 19^m\ 8.15^s$
Declination[1]	$3°26^m\ 20.4^s$
Distance[1]	51.67 ± 0.02 pc
Luminosity[1]	1.652 ± 0.016 $L_\odot$
Radius (R)[1]	1.18 ± 1.21 $R_\odot$
V magnitude [1]	7.57
Mass [2]	~1.15 $M_\odot$
Age[2]	~28 Myrs
Photospheric temperature (T_P)[1]	6027 ± 69 K
Spot temperature (T_S)[3]	3877 ± 50 K
Photosphere-Spot difference[3]	2150 ± 50 K
$v\sin i$[5]	$42.0^{+0.6}_{-0.2}$ km s^{-1}
Inclination angle[5]	68°± 5°
Calculated Inclination angle[5]	55.32°
Rotational period[5]	1.167 ± 0.3 days
Rotation rate at equator (Ω)[5]	4.69 $^{+0.02}_{-0.08}$ rad d^{-1}
Rotational shear ($d\Omega$)[5]	$0.435^{+0.055}_{-0.035}$ rad d^{-1}

[1] Gaia et al. (2016, 2018, 2020)
[2] Baraffe et al. (2015) (see Figure 4.3.1)
[3] Berdyugina (2005)
[4] Torres et al. (2006)
[5] This study

Table 4.3.2 lists the fundamental parameters for HD 43989. As with VXR 77A parameters described in Section 4.2.2 many of the parameters for HD 43989 are also obtained from the Gaia space mission, with the remaining parameters derived during the DI calculations in this study. Figure 4.3.1 shows the position of HD 43989 on an HR diagram using the Gaia values for surface temperature and luminosity. From this figure a mass of ~ 1.15 $M_\odot$ an age of ~28 Myrs is estimated. This falls somewhat short of an estimate of the Columba association age of 42 Myrs (Cameron et al., 2015). The Gaia parallax measurement of 19.352 ± 0.022 mas converts to approximately 51.67 ± 0.02 pc. Luminosity was measured to be 1.652 ± 0.016 $L_\odot$ and photospheric temperature of 6027 ± 69 K. Using the same plot in Berdyugina (2005) as in Section 4.2.2 a spot temperature of 3877 ± 50 K is obtained for a difference of 2150 ± 50 K. The Gaia DR2 release reports a radius of 1.18 ± 1.21 $R_\odot$. This compares to a radius of 1.17 ± 0.03 $R_\odot$ computed by Kriskovics et al. (2019) by methodology using $v\sin i$ and other observed astrophysical parameters. DI analysis from this study derives a $v\sin i$ of $42.0^{+0.6}_{-0.2}$ km s^{-1}. This compares to a value of 41.3 km s^{-1}reported by Hackman et al. (2016) and also used by Willamo et al. (2022). Kriskovics et al. (2019) reports a value of 38 ± 1 km s^{-1}. This study derives a rotation period of 1.167 ± 0.05 days which compares to 1.357 days obtained from Hackman et al. (2016). It should be noted that a similar value of 1.16 days was derived from photometry by Cutispoto et al. (2003), which Hackman et al. (2016) believes is incorrect because they used a more extensive photometric data set to arrive at their value of 1.357 days. Our derived unchanging RV value of 21 km s^{-1}(see Table 4.3.4) compares to 16.66 km s^{-1}in SIMBAD (Zuniga-Fernandez et al., 2021) . Figure 4.3.2 shows two plots of the inclination angle varied by one degree increments and the χ^2 determined. The two plots, one for each observational epoch, are in close agreement and an inclination value of 68 ± 5°is selected as the median value.

As with VXR 77A the ATLAS 9 Kurucz atomic data base was used for the line mask (Kurucz & Bell, 1995). For the observation using the AAT (Epoch 2008.94) a step size of 1.7 km $s^{-1}$was used to create the LSD profiles. For the TBL, a step size of 1.6 km $s^{-1}$was used. The total number of spectral lines in each exposure used to create an LSD profile was between 2114 and 2215 for the AAT and between 4075 and 4090 for the TBL.

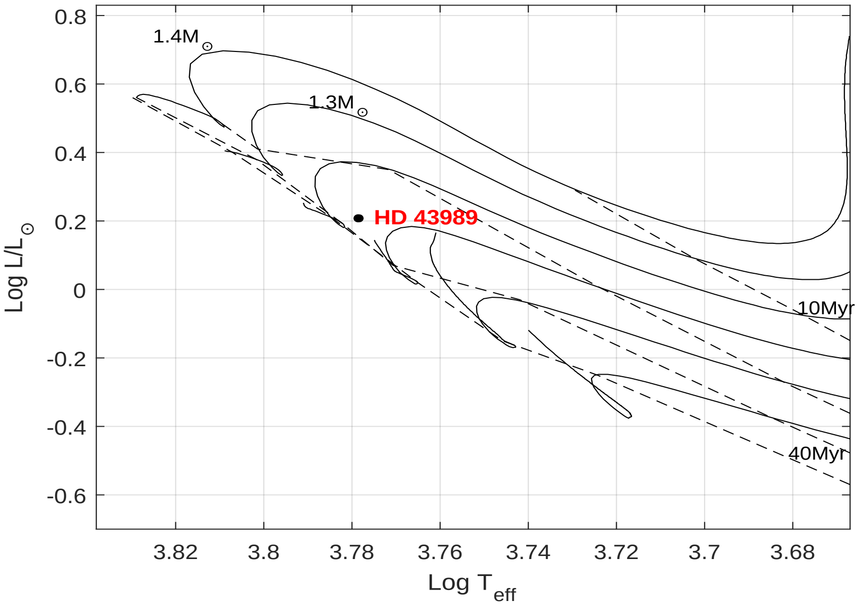

Figure 4.3.1: Age and Mass of HD 43989. Surface temperature and luminosity for HD 43989 were obtained from the Gaia DR 2 release (Gaia et al., 2018) and are plotted in an HR diagram of 0.9 to 1.4 $M_\odot$ in 0.1 $M_\odot$ increments against evolutionary track models provided by Baraffe et al. (2015). Stellar ages of 10, 20, 30 and 40 Myr are overlayed as isochrones. From this plot an age of ~28 Myr and a mass of ~1.15 $M_\odot$ is observed.

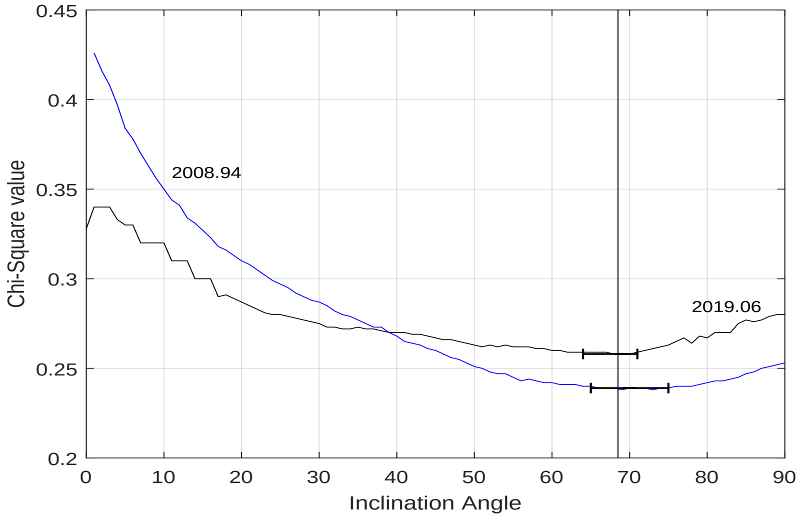

Figure 4.3.2: Inclination angle analysis for HD 43989. A minimum χ^2 value was obtained by changing the inclination angle by 10° increments for each epoch. A vertical line is drawn between the lowest χ^2 values to arrive at an inclination angle of ~68°. This value is close to a calculated value of inclination from the Gaia radius and *v*sin*i* value derived in this study as discussed in Section 4.3.2.

4.3.3 Results

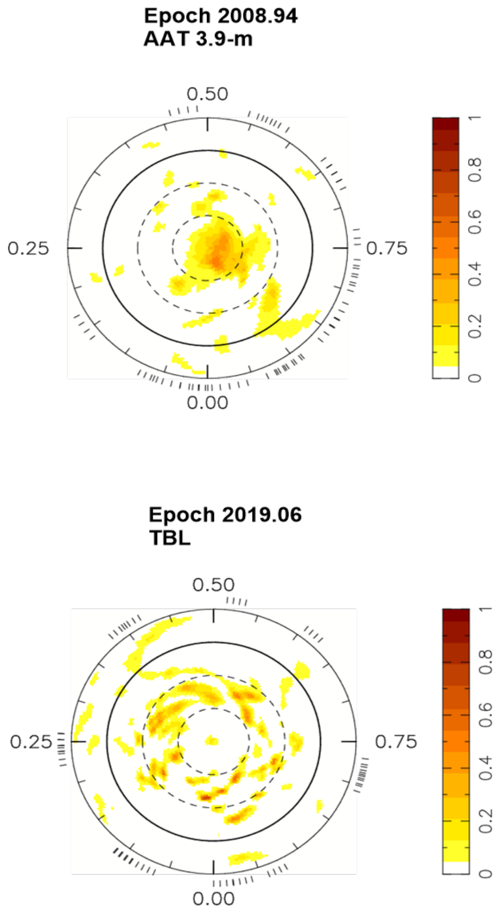

Figure 4.3.3: DI brightness maps for HD 43989 for all epochs. The plot characteristics are the same as in Figure 4.2.3. Both maps were calculated using DR values obtained during the DI process.

Stokes *I* and Stokes *V* Image Reconstruction As with VXR 77A the LSD profiles created using procedures described in Section 3.1.2 are used to create surface brightness maps and magnetic maps for both epochs (epoch 2008.94, 2019.96) using procedures described in Section 3.2 (see maximum entropy fit maps in Figures A.2.1 and A.2.2 and magnetic fit maps in Figure B.1.1) . Polar projections of the surface brightness for each epoch are shown in Figure 4.3.3. These plots show a prominent polar spot in the first epoch with less prominent spots spreading down to and below the visible equator. This polar spot is largely absent in the second epoch however, there is a small spot directly at the visible pole.

Figures 4.3.4 and 4.3.5 show the magnetic maps for the two epochs respectively. These maps show a magnetic field with the poloidal and toroidal components roughly equal (see Table 4.3.3) and non-axisymmetric. The meridional field in the first epoch (2008.94) is very weak compared to the later epoch (2019.06) which shows a more complex field. The small spot located at the pole in the brightness map for epoch 2008.94 can be seen in the azimuthal map for the same epoch. Most of the field strength is in the higher harmonics ($l \geq 4$).

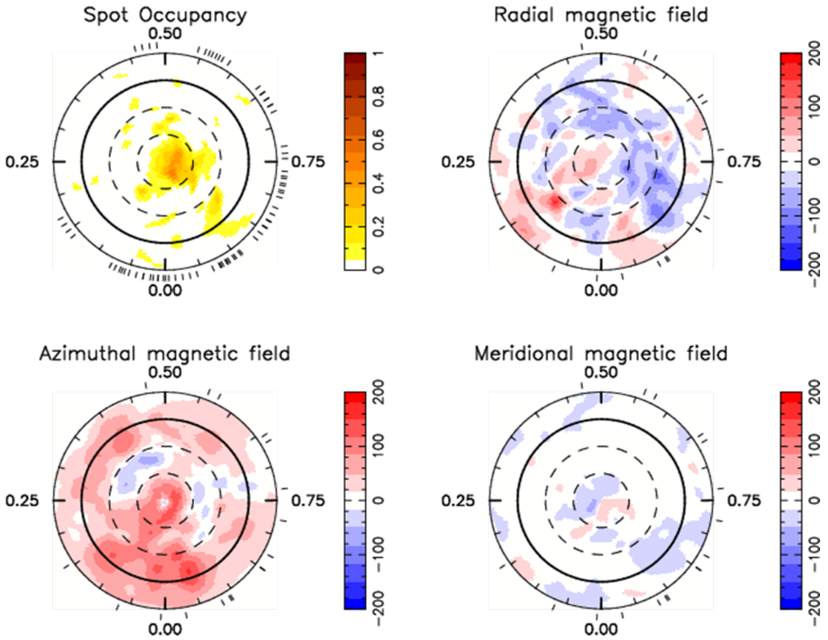

Figure 4.3.4: Maximum entropy brightness and magnetic image reconstructions for HD 43989 epoch 2008.94. The spot occupancy (brightness) map is the same as in Figure 4.3.3. The scale bar for the magnetic maps provides field strength in Gauss and the polarity. All maps were calculated using the DR value obtained in the DI process.

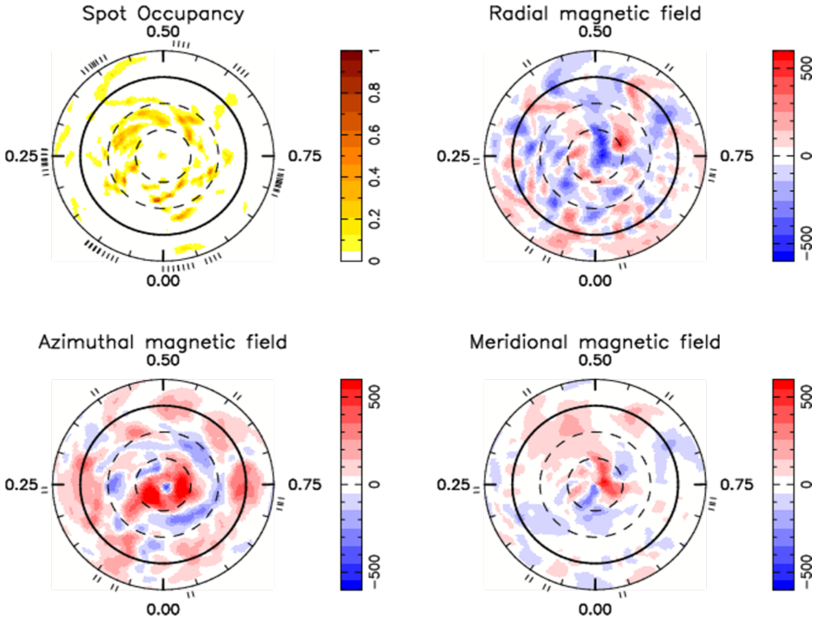

Figure 4.3.5: Maximum entropy brightness and magnetic image reconstructions for HD 43989 epoch 2019.06. The spot occupancy (brightness) map is the same as in Figure 4.3.3. The scale bar for the magnetic maps provides field strength in Gauss and the polarity. Threshold levels for field strength have been set higher than those seen in Figure 4.3.4. This could suggest that there has evolved a higher field strength than the earlier observation, but is just as likely that the higher sensitivity of the spectropolarimeter at the TBL recovered a greater portion of the magnetic field and required a higher field strength threshold in the display map to avoid saturation of the colors.

Table 4.3.3: Magnetic quantities derived from maps in Figure 4.3.4 and Figure 4.3.5. Magnetic field values are separated into poloidal and toroidal parts and are further separated into l values of 1, 2, 3 and ≥ 4 respectively. The last two values in the table show which parts of the poloidal and toroidal fields are axisymmetric (m=0). Variations were obtained by increasing and decreasing $v\sin i$ by + 0.6 km s^{-1}and -0.2 km s^{-1}, inclination angle by 10°and DR by one standard deviation (± 0.033 rad d^{-1}). The field percentages indicate that the magnetic field may be in the middle of a cycle with the majority of the energy in the $l \geq 1$ shell.

Quantity (percent energy)	Epoch 2008.94	Epoch 2019.06
Total poloidal	43^{+2}_{-5}	51^{+7}_{-11}
Total toroidal	57^{+6}_{-1}	49^{+11}_{-0}
poloidal (l=1)	13^{+0}_{-2}	4^{+0}_{-1}
poloidal (l=2)	$7^{+0}_{-1.5}$	2^{+0}_{-1}
poloidal (l=3)	2^{+0}_{-1}	1^{+0}_{-1}
poloidal (l≥4)	20^{+3}_{-4}	$45\ ^{+0}_{-10}$
toroidal (l=1)	34^{+6}_{-1}	$6\ ^{+1}_{-0}$
toroidal (l=2)	4^{+1}_{-1}	$2\ ^{+0}_{-1}$
toroidal (l=3)	2^{+1}_{-3}	$0\ ^{+3}_{-0}$
toroidal (l ≥4)	17^{+12}_{-1}	40^{+1}_{-6}
axisymetry poloidal	11^{+2}_{-2}	$19\ ^{+3}_{-4}$
axisymetry toroidal	49^{+1}_{-2}	$36\ ^{+10}_{-6}$

The large-scale magnetic field is constructed from the spherical harmonic expansions in percentages of poloidal and toroidal components as described in Section 3.2.2, and are then divided into l values. From this it can be seen how the star's magnetic field is distributed through the star, and how these values change between epochs, providing information about the evolution of the magnetic field and its underlying dynamo. Table 4.3.3 shows the values for the magnetic quantities derived from the two magnetic maps, with magnetic energies given as percentages of the poloidal and toroidal components.

Differential Rotation As with VXR 77A DR parameters were derived using procedures and limitations discussed in Section 5.2. DR parameters were obtained from epoch 2008.94 only and resulted in a less than perfect paraboloid. The values obtained from this plot are $\Omega_e q$ = 4.69 ± 0.08 and dΩ = 0.44 ± 0.06. These values when incorporated into the DI analysis reduced the χ^2 value only slightly. Again as with VXR 77A, the poor shape of the paraboloid in Figure 4.3.6 make the DR values recovered tentative at best.

As with VXR 77A the differential shear derived for HD 43989 (if correct) place it in the higher realms of the young solar-type stars discussed in the Literature Review Section 2. This comparison along with VXR 77A in this thesis are discussed in more detail in the final discussion in Section 5.

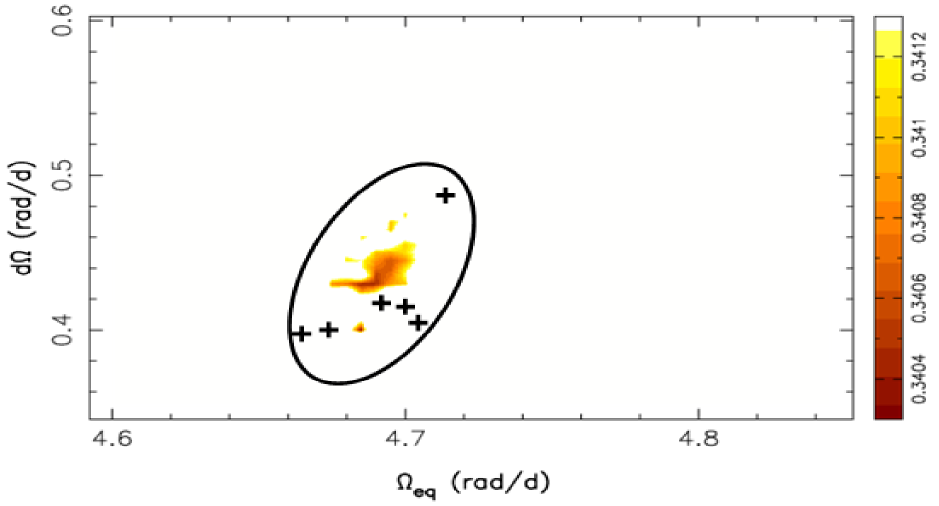

Figure 4.3.6: DR measurement for HD 43989 epoch 2008.94. Values of $d\Omega$ versus Ω_{eq} are plotted to form a paraboloid (yellow-brown area of the plot) with the best χ^2 value at the darkest area in the center. 1σ variances are generated by changing the inclination by 10°, $v\sin i$ by -0.2 km s^{-1}to 0.5 km s^{-1}and the maximum entropy spot aim by ± 5 percent. The values shown are crosses which are within the ellipse.

Table 4.3.4: Data derived from the DI analysis for HD 43989. The observation epoch is in column 1. The total number of usable Stokes *I* exposures is in column 2. Column 3 is the SNR for each exposure. Percent spot coverge across the stellar surface is in column 4. RV values are in column 5. By plotting RV values against decreasing χ^2 values an error of 0.1 km s^{-1}is estimated for the AAT and TBL.

Epoch	No. of Exposures	LSD SNR	Spot Percentage	RV (km s^{-1}) Values
2008.94	74	866	2.2	21.0 ± 0.1
2019.06	64	366	2.3	21.0 ± 0.1

Radial Velocity RV measurements for HD 43989 did not change between the two observational epochs of this study. The value measured is 21.0 ± 0.1 km s^{-1}which is close to the value of 20.36 ±0.38 km s^{-1}from the Gaia DR 3 release (Gaia et al., 2022). This appears to indicate no major companion orbiting HD 43989. Table 4.3.4 lists the results of the DI analysis.

Spots and Latitude Distribution Latitudal spottedness is displayed as with VXR 77A using Equation 4.2.2. This is graphically shown in Figure 4.3.7. The graph shows some evolution of spots between epochs with spots concentrated off-center of the visible pole for epoch 2008.94 and further distributed in epoch 2019.06.

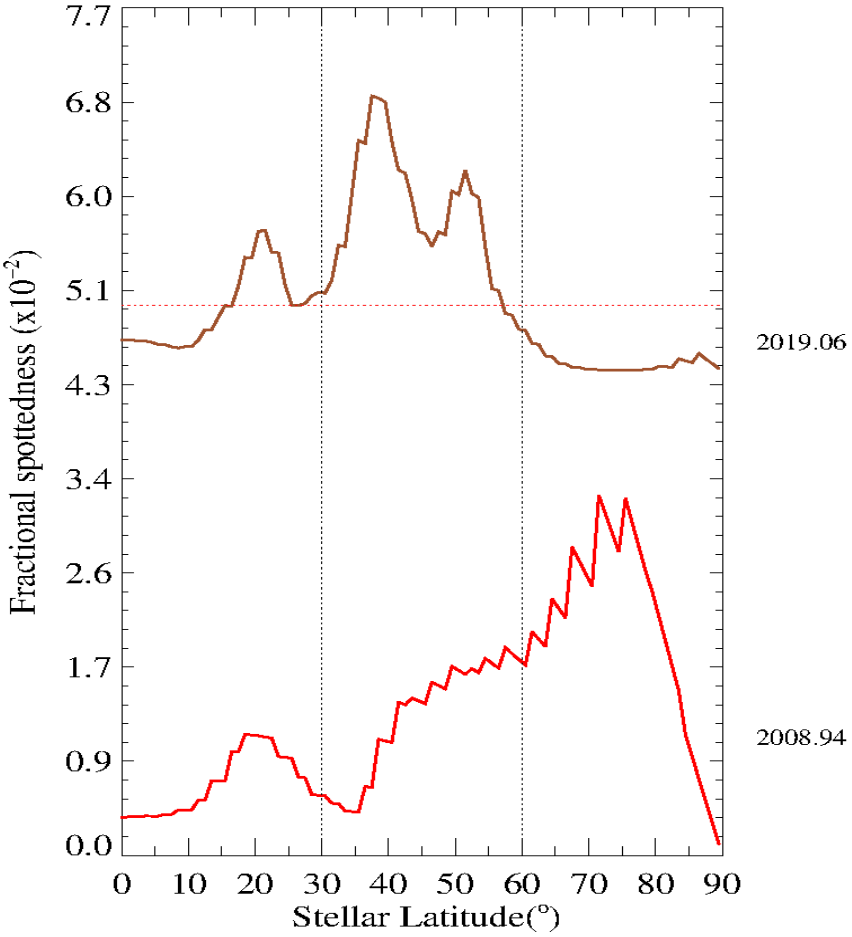

Figure 4.3.7: HD 43989 fractional spottedness by latitude for all epochs. Fractional spottedness is defined by Equation 4.2.2 and is the average instance of spots at each latitude. Epoch 2019.06 is shifted up for graphing purposes. A major change in fractional spot latitude distribution is apparent between these two epochs.

4.3.4 HD 43989 TESS Photometric Comparisons

As with VXR 77A additional photometric data for HD 43989 was obtained from the Transiting Exoplanet Survey Satellite (TESS) using the data portal at the Mukulski Archive for Space Telescopes (MAST) (STSCI, 2024). This data is shown in Figure 4.3.8. These are light curve files for two observations made in 2018 and 2020 using Simple Aperture Photometry (SAP) by summing pixel brightness from a pre-selected aperture (TSSC, 2024). A periodogram of each curve shows a period of ~1.360 d for both graphs, sector 06 and sector 33. This compares to a rotational period of ~1.167 derived from the DI analysis (see Table 4.3.2).

It should be noted here that the period of 1.360 d obtained from the TESS light curves closely matches the value of 1.357 d reported by (Hackman et al., 2016) as discussed earlier at the beginning of Section 4.3.2. This value could be fitted to the AAT 2008.94 epoch only by raising the χ^2 value to the calculations. A rotation rate of 1.167 d was the best statistical fit for both the AAT data (Epoch 2008.94) and the TBL data (Epoch 2019.06) from this study.

As with VXR 77A photometric analysis of the light curve data is discussed in Section 5.1. Construction of the light curves as well as analysis of the periodogram was done using the TESS data analysis tool lightkurve (Lightkurve Collaboration et al., 2018).

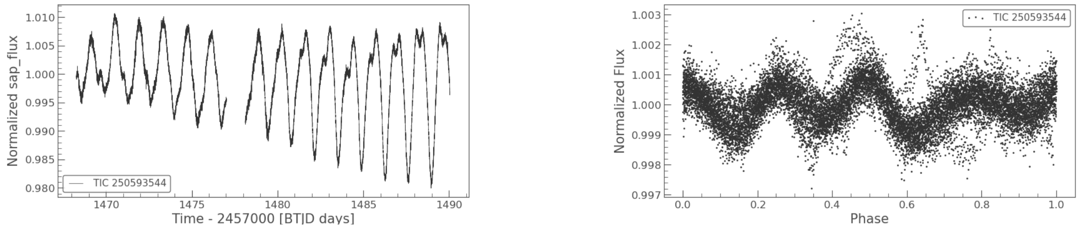

(a) Sector 06 2018 Light Curve, period ~1.360 d (b) Sector 06 2018 Folded Light Curve

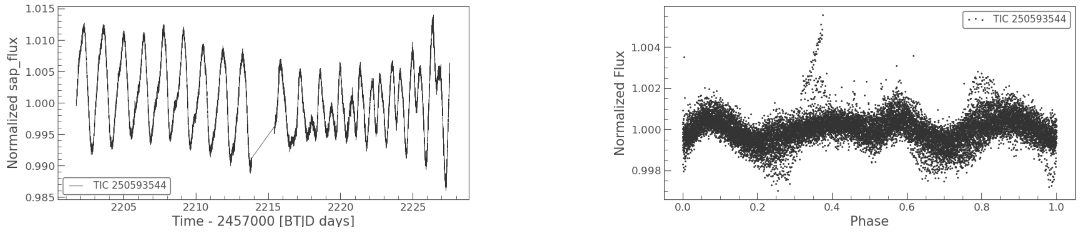

(c) Sector 33 2020 Light Curve, period ~1.360 d (d) Sector 33 2020 Folded Light Curve

Figure 4.3.8: TESS photometric observations of HD 43989 made in 2018 and 2020. The period of these plots is consistent with the rotation period of 0.653 days derived from the DI analysis (see Table 4.3.2). The data described here may be obtained from the MAST portal. The TESS Identification Catalog ID is shown for each graph (see discussion in Section 4.3.4).

4.4 HIP 71933

4.4.1 Observations Overview

Seven epochs of HIP 71933 were observed between 2009 to 2019 using three telescopes (see Table 4.4.1 for a summary). Epochs 2009.34, 2010.33, 2012.26, 2018.07, and 2019.46 were recorded using 2.3-m telescope at Siding Spring Observatory. Stokes I data only was recorded. This data has been published as a part of this PhD research in Hughes et al. (2023).

For the Stokes V polarisation data, two epochs were recorded at telescopes equipped with spectropolarimeters. Epoch 2009.26 was recorded at the AAT using the SEMPOL/UCLES spectropolarimeter. Epoch 2011.37 was recorded at the 3.6-m using the HARPSpol spectropolarimeter.

As with VXR 77A and HD 43989 the observation epochs cover sufficient time to provide full-phase coverage of HIP 71933 given the rotation period of 0.67 d (see Table 4.4.2). As with VXR 77A and HD 43989 the zero points for all epochs are calculated as an integer number of rotations starting with the zero point of the first epoch. The zero point chosen for the epoch is the JD which is closest to the previously calculated value.

The rotational phase was computed using the ephemeris:

$$\mathrm{JD} = 2454932.211 + 0.67\phi \tag{4.4.1}$$

where JD is the observational data and ϕ is the rotational phase.

Table 4.4.1: Log of spectroscopic observations for all epochs for HIP 71933. The first column lists the epoch of the observation and the second column lists the telescope. Columns arrangements are the same as for VXR 77A in Table 4.2.3. The zero points for all epochs are calculated the same as for VXR 77A. This table is reproduced from Hughes et al. (2023).

Epoch	Telescope	Instrument Resolution	Date	UT Start	UT End	No. of Stokes I exposures	Observer(s)	Rotational Cycle
2009.26	AAT	~70,000	2009 Apr 07	12:20	16:02	8	I. Waite	-4.563 to 4.668
			2009 Apr 08	11:01	16:45	12	S. Marsden, I. Waite	
			2009 Apr 09	11:40	18:22	7	S. Marsden, I. Waite	
			2009 Apr 13	16:11	16:55	4	B. Carter, S. Marsden, I. Waite	
2009.34	2.3-m	~24,000	2009 May 04	12:39	17:36	7	D. Burton	-1.214 to 2.070
			2009 May 06	10:35	10:55	11	D. Burton	
2010.33	2.3-m	~24,000	2010 Apr 01	12:09	18:59	15	D. Burton	-2.722 to 2.093
			2010 Apr 02	12:38	19:13	11	D. Burton	
			2010 Apr 03	13:05	17:16	10	D. Burton	
			2010 Apr 04	12:22	17:20	9	D. Burton	
2011.37	3.6-m	~115,000	2011 May 16	02:04	23:20	12	E. Hébrard	-3.384 to 4.147
			2011 May 17	01:39	23:19	12	E. Hébrard	
			2011 May 18	00:26	23:57	16	E. Hébrard	
			2011 May 19	01:17	07:31	8	E. Hébrard	
			2011 May 20	00:01	23:28	22	E. Hébrard	
2012.26	2.3-m	~24,000	2012 Apr 04	12:28	16:59	5	D. Burton	-4.180 to 3.596
			2012 Apr 05	15:11	18:44	3	D. Burton	
			2012 Apr 06	16:29	17:30	2	D. Burton	
			2012 Apr 07	11:15	17:41	6	D. Burton	
			2012 Apr 09	11:51	17:41	6	D. Burton	
2018.07	2.3-m	~24,000	2018 Jan 25	16:45	18:37	4	I. Waite	-2.763 to 1.794
			2018 Jan 28	15:16	18:06	6	I. Waite	
2019.46	2.3-m	~24,000	2019 Jun 17	08:07	11:46	10	S. Marsden	-2.080 to 2.874
			2019 Jun 18	08:04	12:16	12	S. Marsden	
			2019 Jun 19	08:05	16:06	16	S. Marsden	
			2019 Jun 20	08:02	16:02	18	S. Marsden	

Table 4.4.2: Fundamental parameters for HIP 71933 (HD 129181, Gaia DR2 5905397139423601792). This table is reproduced from Hughes et al. (2023).

Parameter	Value
Classification[4]	F8V
Right Ascension[1]	14^{h} 42^{m} 5^{s}
Declination[1]	-48°47^{m} 59.28^{s}
Distance[1]	90.033 ± 0.042 pc
Luminosity[1]	2.839± 0.028 $L_{\odot}$
Radius (R)[1]	1.60 ± 1.21 $R_{\odot}$
V magnitude [1]	8.17
Mass [2]	$\sim$1.3 $M_{\odot}$
Age[2]	$\sim$15 Myr
Photospheric temperature (T_P)[1]	5922.1 ± 155 K
Spot temperature (T_S)[3]	4022 ± 50 K
Photosphere-Spot difference[3]	1900 ± 50 K
$v$sin$i$[5]	$76^{+0.5}_{-0.2}$ km s^{-1}
Inclination angle[5]	37°± 10°
Calculated Inclination angle[5]	38.95°
Rotational period[5]	0.67 ± 0.05 days
Rotation rate at equator (Ω)[5]	$9.46^{+0.02}_{-0.01}$rad d^{-1}
Rotational shear ($d\Omega$)[5]	$0.33^{+0.07}_{-0.04}$ rad d^{-1}

[1] Gaia et al. (2016, 2018, 2020)
[2] Baraffe et al. (2015) (see Figure 4.4.1)
[3] Berdyugina (2005)
[4] Torres et al. (2006)
[5] This study

4.4.2 Stellar Parameters

Fundamental parameters for HIP 71933 are listed in Table 4.4.2. As described with VXR 77A in Section 4.2.2 and HD 43989 in Section 4.3.2 most of the parameters were obtained from the ESA's Gaia space mission, and the remaining were derived from this study as described in Sections 3.2.1 and 3.2.2. A distance of 90.033 ± 0.042 pc was calculated from a parallax of 11.107 measured by the Gaia satellite, which also measured luminosity to be 2.839 ± 0.028 $L_{\odot}$ and a photospheric temperature of 5922.1 ± 155 K (Gaia et al., 2018). As with Section 4.2.2 (Berdyugina, 2005) is used to obtain a difference between photospheric temperature and spot temperature to result in a spot temperature of 4022 ± 50 K. . Using the (Baraffe et al., 2015) atmospheric models HIP 71993 can be placed on this graph to estimate a mass of $\sim$1.3 $M_{\odot}$ and an age of $\sim$15 Myr (see Figure 4.4.1). Previous estimates of 20 Myr Waite et al. (2011) are slightly older but did not have access to the more recent Baraffe et al. (2015) models and the Gaia et al. (2018) release. The values derived in this study, $v$sin$i$, radial velocity (RV), inclination and rotation period (P_{rot}) were obtained by varying these parameters until a minimum χ^2 was accomplished. A $v$sin$i$ of 76 ± 0.5 km $s^{-1}$and a rotational period of 0.67 ± 0.05 days is derived in this study. This is comparted with a $v$sin$i$ of 75± 1,0 km s^{-1}reported by Waite et al. (2011) and a rotational period of 0.67 days reported by Desidera et al. (2015) which is the same as the value derived in this study. Inclination values are plotted against decreasing χ^2 values from the observation epochs with the best

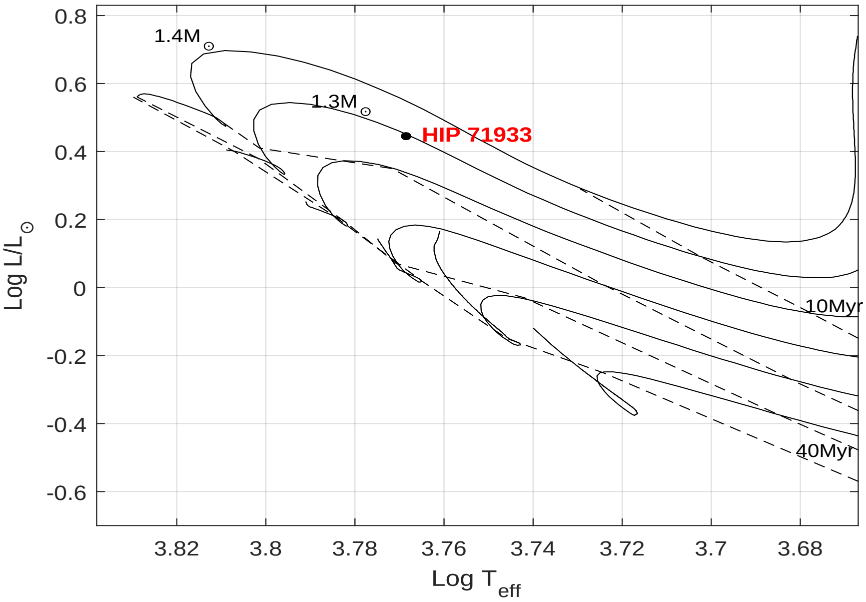

Figure 4.4.1: Age and mass of HIP 71933. Surface temperature and luminosity for HIP 71933 were obtained from the Gaia DR 2 release (Gaia et al., 2018) and are plotted in an HR diagram of 0.9 to 1.4 M$_\odot$ in 0.1 M$_\odot$ increments against evolutionary track models provided by Baraffe et al. (2015). Stellar ages of 10, 30, 30 and 40 Myr are overlayed as isochrones. From this plot an age of ~15 Myr and a mass of ~1.3 M$_\odot$ is observed. This plot is reproduced from Hughes et al. (2023).

phase coverage. A vertical line is drawn across the inclination plots at the lowest χ^2 to obtain an inclination of 37 ± 10°(see Figure 4.4.2). From this plot, a stellar inclination of ~37 ± 10°is seen (see Figure 4.4.2). Using the Gaia DR 2 radius of 1.6 R$_\odot$ (Gaia et al., 2018), a $v\sin i$ of 76 km s^{-1}and rotational period of 0.67 days derived in this study, an inclination of 38.95°is calculated which is consistent with the modelled value.

As with VXR 77A and HD 43989 the ATLAS 9 Kurucz atomic data base was used for the line mask (Kurucz & Bell, 1995). A step size of 1.7 km s^{-1}was used for the AAT observations. A step size of 4.2 km s^{-1}was used for the 2.3-m telescope and a step size of 1.6 km s^{-1}was used for the 3.6-m telescope. The total number of spectral lines in each exposure used to create an LSD profle was between 2072 and 2185 for the AAT, 2705-3093 for the 2.3-m telescope and 3049-3082 for the 3.6-m telescope.

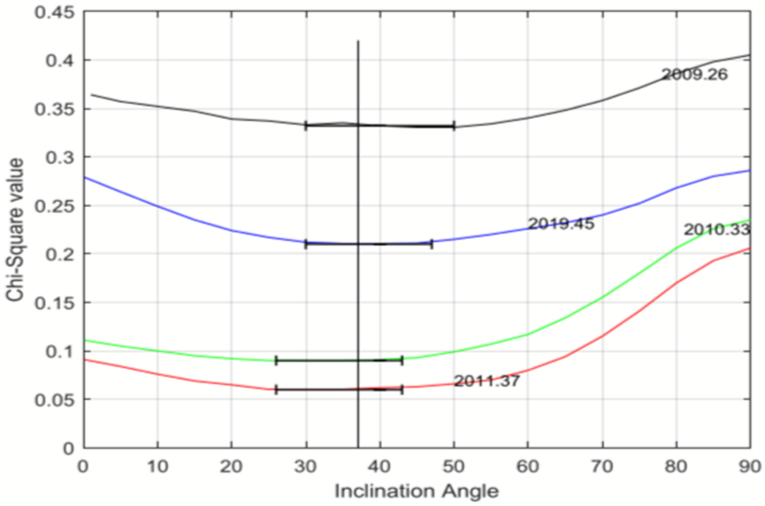

Figure 4.4.2: Inclination angle analysis for HIP 71933. A minimum χ^2 was obtained by changing the inclination angle by 10°increments for each epoch. A vertical line is drawn between the lowest χ^2 values to arrive at an inclination angle of ~37°. This value is close to a calculated value of inclination from the Gaia radius and *v*sin*i* value derived in this study as discussed in Section 4.4.2. This plot is reproduced from Hughes et al. (2023).

4.4.3 Results

Stokes *I* and Stokes *V* Image Reconstruction As with VXR 77A and HD 43989, the LSD profiles created using procedures described in Section 3.1.2 (see Figures A.3.1 through A.3.7) were used to create surface brightness maps using procedures described in Section 3.2 for all epochs and magnetic image maps for two epochs (2009.26 and 2011.37). Table 4.4.4 lists spot coverage as a percent of stellar surface and RV. Figure 4.4.3 shows polar projections of the surface brightness for each epoch.

Figures 4.4.4 and 4.4.5 show the magnetic maps for epochs 2009.36 and 2011.37 respectively. The brightness map is reproduced in the top left to compare with the magnetic maps. Both magnetic maps show a dipolar field with the greatest strength in the poloidal field. The +60°ring prominent in the brightness maps of all epochs is also displayed in the azimuthal field of the magnetic maps.

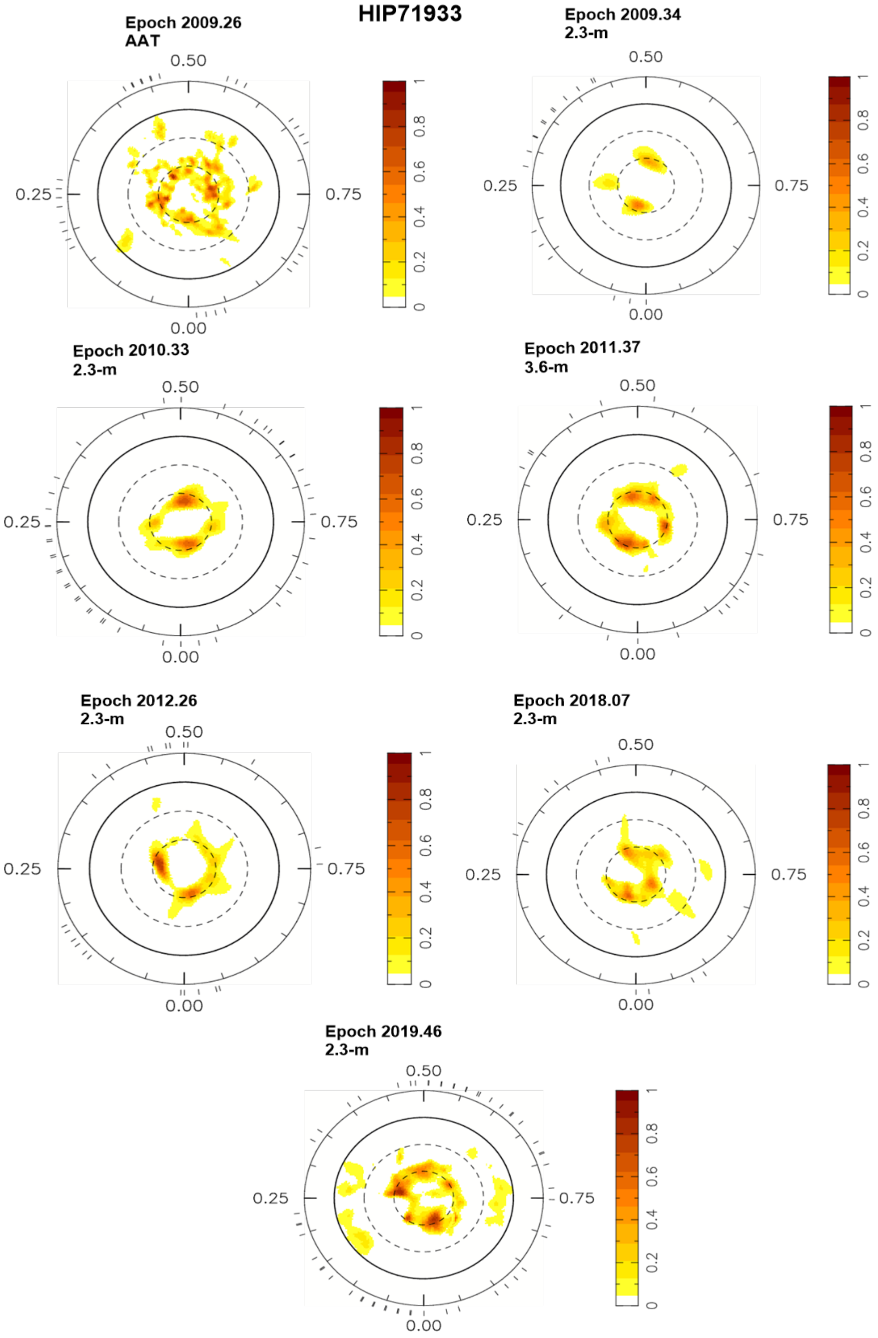

Figure 4.4.3: DI brightness maps for HIP 71933 for all epochs. The plot characteristics are the same as in Figure 4.2.3. All maps were calculated using the DR value obtained during the DI process. This plot is reproduced from (Hughes et al., 2023).

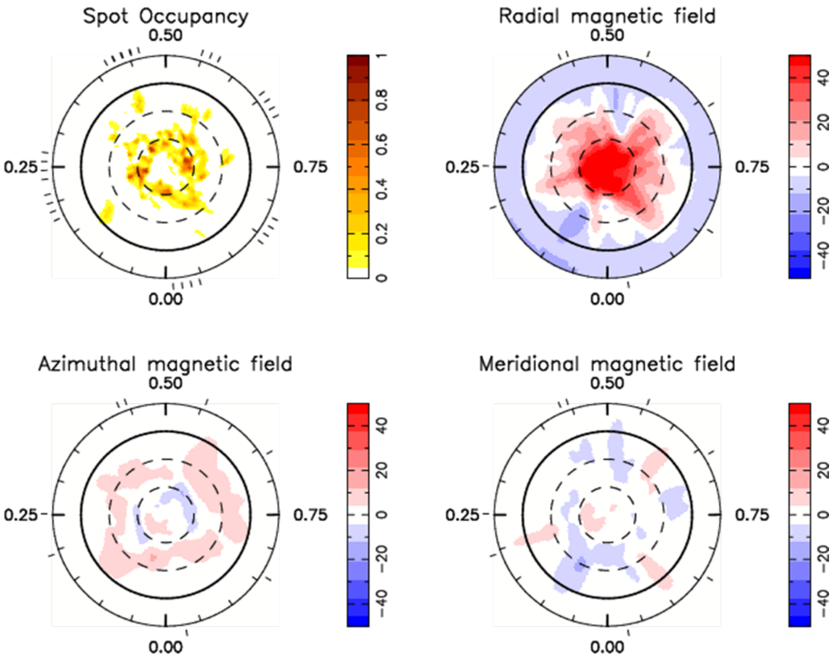

Figure 4.4.4: Maximum entropy brightness and magnetic image reconstructions for HIP 71933 Epoch 2009.26. The spot occupancy (brightness) map is the as in Figure 4.4.3. The scale bar for the magnetic maps provides field strength in Gauss and polarity. All maps were calculated using the DR value obtained during the DI process. This plot is reproduced from (Hughes et al., 2023).

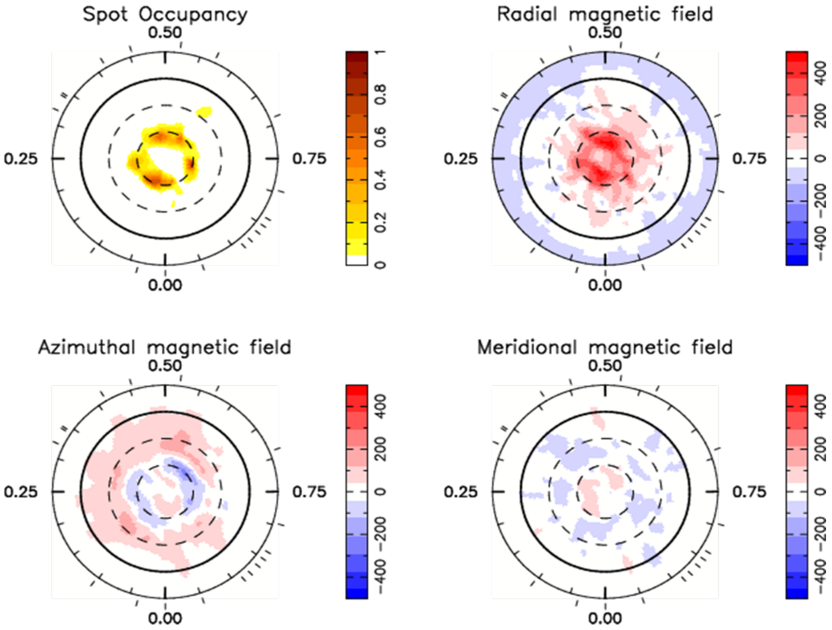

Figure 4.4.5: Maximum entropy brightness and magnetic image reconstructions for HIP 71933 Epoch 2011.37. The spot occupancy (brightness) map is the as in Figure 4.4.3. The scale bar for the magnetic maps provides field strength in Gauss and polarity. All maps were calculated using the DR value obtained in the DI process. This plot is reproduced from (Hughes et al., 2023).

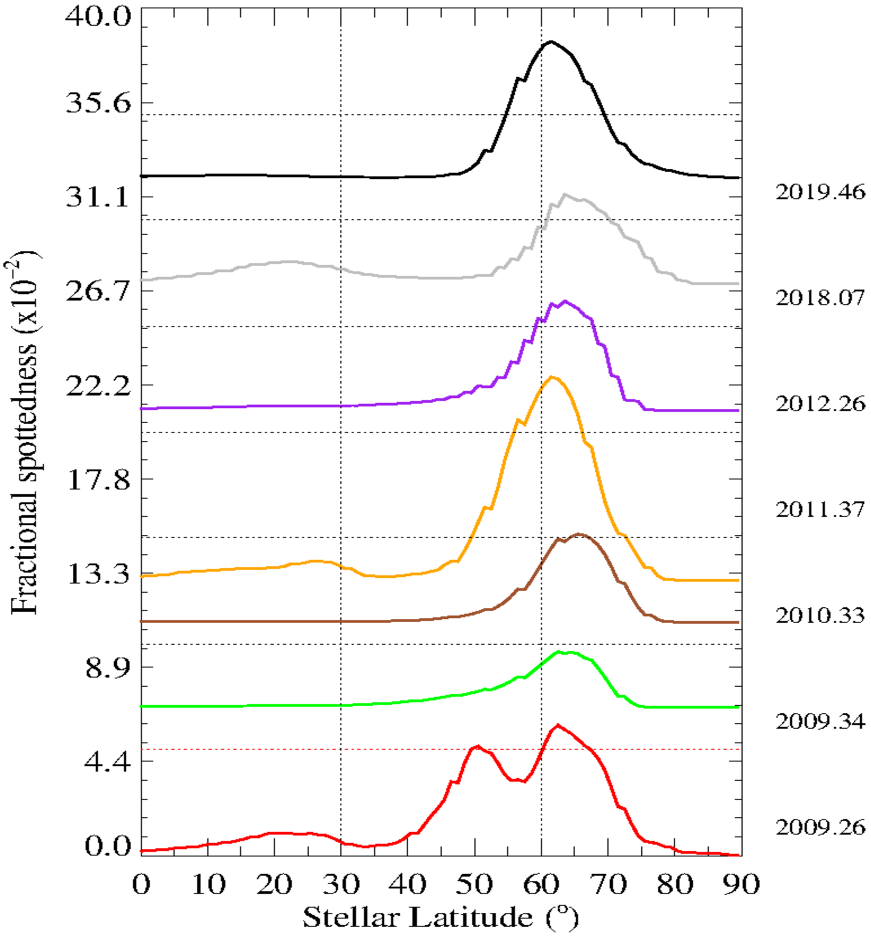

Figure 4.4.6: HIP 71933 fractional spottedness by latitude for all epochs. Fractional spottedness is defined by Equation 4.2.2 and is the average instance of spots at each latitude. Each epoch is shifted up for graphing purposes. The peaks show increased spots at the +60°ring with little or no spotting at the visible pole. The bump at the 50°latitude in epoch 2009.26 could be an indication of the end of a more active cycle since it appears in the first epoch of the ten years of observations. This plot is reproduced from Hughes et al. (2023).

Spots and Latitude Distribution Latitudinal spottedness is displayed as with VXR 77A and HD 43989 using Equation 4.2.2. This is graphically shown in Figure 4.4.6. Here there is a bump at approximately the 60°latitude which shows maximum spots at the persistent high-latitude ring seen in all epochs in the brightness and magnetic maps.

As with HD 43989, the large-scale magnetic field is constructed from the spherical harmonic expansions in percentages of poloidal and toroidal components as described in Section 3.2.2, and are then divided into *l* values. From this it can be seen how the star's magnetic field is distributed over the stellar surface, and how these values change between epochs, providing information about how the magnetic field evolves and its underlying dynamo. Table 4.4.3 shows magnetic quantities for each epoch in poloidal and toroidal percentages.

Table 4.4.3: Magnetic quantities from maps in Figures 4.4.4 and 4.4.5. Magnetic field values are separated into poloidal and toroidal parts and are further separated into l values of 1, 2, 3, and ≥ 4 respectively. The last two values in the table show which parts of the poloidal and toroidal fields are axisymmetric (m=0). Variations were obtained by increasing and decreasing $v\sin i$ by +0.6 kmss and -0.2 km s^{-1}, inclination angle by 10° and DR by one standard deviation (± 0.033 rad d^{-1}). This table is reproduced from Hughes et al. (2023).

Quantity	Epoch 2009.26 percent energy	Epoch 2011.37 percent energy
Total poloidal	94^{+1}_{-0}	83^{+2}_{-3}
Total toroidal	6^{+0}_{-1}	17^{+3}_{-1}
poloidal (l=1)	62^{+2}_{-2}	50^{+5}_{-1}
poloidal (l=2)	14^{+2}_{-1}	12^{+1}_{-1}
poloidal (l=3)	7^{+1}_{-0}	5^{+1}_{-1}
poloidal ($l \geq 4$)	12^{+1}_{-1}	$14\ ^{+2}_{-2}$
toroidal (l=1)	2^{+0}_{-0}	$5\ ^{+1}_{-1}$
toroidal (l=2)	1^{+0}_{-0}	$2\ ^{+1}_{-0}$
toroidal (l=3)	0^{+0}_{-0}	$1\ ^{+1}_{-0}$
toroidal ($l \geq 4$)	3^{+0}_{-0}	$10\ ^{+2}_{-2}$
axisymetry poloidal	82^{+3}_{-1}	$74\ ^{+3}_{-1}$
axisymetry toroidal	5^{+0}_{-1}	$16\ ^{+2}_{-2}$

When discussing spottedness it must be noted that there is an almost ten year period between the first observations in 2009 and the last in 2019. Given that the rotational period was stated to be 0.67 ±0.05 d (reference Table 4.4.2) the phase information becomes unreliable after 20 days. Long time periods between observations reduce the ability to observe evolution of spots from epoch to epoch. In the case of HIP 71933 it is more important to identify the existence of the +60°ring, the recurring spot clumps within the ring and the absence of spots at the observable pole. These features persist throughout all of the observation epochs.

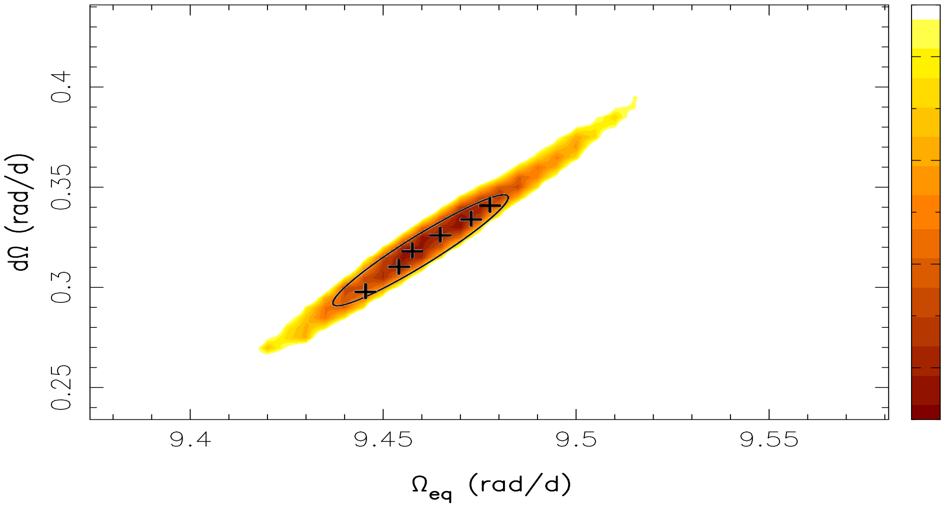

Figure 4.4.7: DR measurement for HIP 71933 epoch 2011.37 Values of $d\Omega$ versus Ω_{eq} are plotted to form a paraboloid (yellow-brown area of the plot) with the best χ^2 value at the darkest area in the center. 1σ variances are generated by changing the inclination by 10°, $v$sin$i$ by -0.2 km $s^{-1}$to 0.5 km $s^{-1}$and the maximum entropy spot aim by ± 5 percent. The values shown are crosses which are within the ellipse. This plot is reproduced from Hughes et al. (2023).

Differential Rotation As with VXR 77A DR and HD 43989 DR parameters were derived using procedures and limitations discussed in Section 5.2 and parameters were derived from the 2011.37 epoch only, from the Stokes I (brightness) maps. Unlike VXR 77A and HD 43989 a uniform paraboloid is recovered, indicating a more trustworthy result, with values of Ω_{eq} = 9.46 ±0.04 rad $d^{-1}$and a rotation shear dΩ = 0.33 ±0.01 rad d^{-1}. These values when incorporated into the DI analysis resulted in a significant drop in the χ^2 value obtained. As with VXR 77A and HD 43989 the differential shear derived for HIP 71933 place it in the higher realms of the young solar-type stars as described in Section 2. This comparison along with the other two stars in this thesis are discussed in more detail in the discussion in Section 5.

Radial Velocity Previous studies have reported RV values for HIP 71933. A RV of 5.5 km s^{-1} was reported by the VLT/NaCo Large Program (Desidera et al., 2015) and they record HIP 71933 as a suspected spectroscopic binary (SB) although there is no record of HIP 71933 (or HD 129181) in the Ninth Catalog of Spectroscopic Binary Orbits (SBORBITCAT) (Pourbaix et al., 2018). A mean value of 12.3 km $s^{-1}$is reported by the Pulkovo compilation of radial velocities (Gontcharov, 2016). A value of 6.18 km $s^{-1}$is entered by the Gaia DR 3 release (Gaia et al., 2022). This study derives a variation across epochs from 4.5 ± 1.0 km $s^{-1}$to 6.4 ± 0.1 km s^{-1}(see Table 4.4.4). It is difficult to identify a period in this study because there is no data before 2009 and between 2013 and 2018, however the values support the previous report that HIP 71933 is a SB. RV values for HIP 71933 plotted against time for all epochs is shown im Figure 4.4.8.

Table 4.4.4: Data derived from the DI analysis for HIP 71933. The observation epoch is in column 1. The total number of usable Stokes *I* exposures is in column 2. Column 3 is the SNR for each exposure. Percent spot coverge across the stellar surface is in column 4. RV values are in column 5. By plotting RV values against decreasing χ^2 values an error of 0.1 km $s^{-1}$is estimated for the AAT and 3.6-m telescopes and 1.0 km $s^{-1}$for the 2.3-m telescope. This table is reproduced from Hughes et al. (2023).

Epoch	No. of Exposures	LSD SNR	Spot Percentage	RV (km s^{-1}) Values
2009.26	31	937	1.8	5.7 ± 0.1
2009.34	18	541	0.73	5.9 ± 1.0
2010.33	45	832	1.47	6.4 ± 0.1
2011.37	70	1045	2.00	6.1 ± 1.0
2012.26	22	871	1.43	5.8 ± 1.0
2018.07	10	868	1.67	5.7 ± 1.0
2019.46	56	835	1.69	4.5 ± 1.0

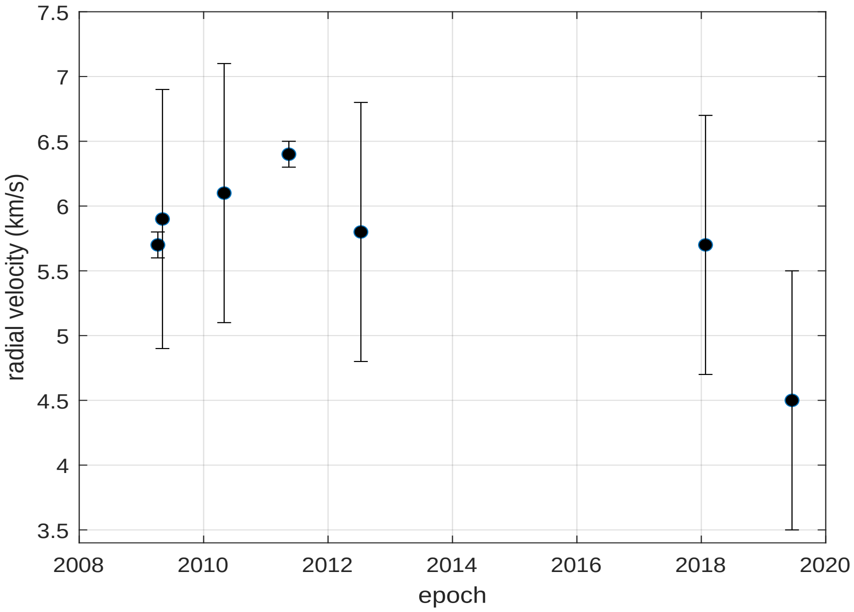

Figure 4.4.8: Radial Velocity (RV) values plotted over time for all epochs. Error bars were obtained from RV values derived with decreasing χ^2. RV errors for epoch 2009.26 and 2011.37 are the smallest due to the superior resolution and stability of the spectroscopic measurements made at the AAT and the ESO 3.6-m telescope. There is no data between 2013 and 2018. This plot is reproduced from Hughes et al. (2023).

4.4.4 HIP 71933 TESS Photometric Comparisons

As with VXR 77A and HD 43989 additional photometric data for HIP 71933 was obtained from the Transiting Exoplanet Survey Satellite (TESS) using the data portal at the Mukulski Archive for Space Telescopes (MAST) (STSCI, 2024). This data is shown in Figure 4.4.9. These are light curve files for three observations made in 2019, 2021 and 2023 using Simple Aperture Photometry (SAP) by summing pixel brightness from a pre-selected aperture (TSSC, 2024). A periodogram of each lightcurve shows a period of ~0.668 for the top curve sector 11, ~ 0.674 for the middle curve sector 38 and ~0.676 for the bottom curve sector 65. These values are consistent with a value of ~0.67 ±0.05 d for HIP 71933 derived in the DI analysis (see Table 4.4.2) and narrow the error margin obtained in that analysis. As with VXR 77A and HD 43989 photometric analysis of the light curve data is discussed in Section 5.1. Construction of the light curves as well as the analysis of the periodogram was done using the TESS data analysis tool lightcurve (Lightkurve Collaboration et al., 2018).

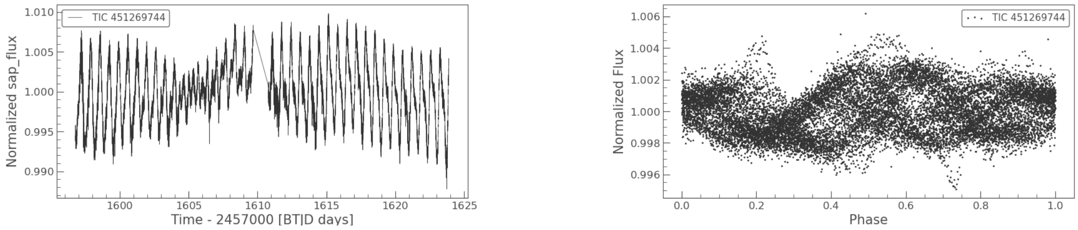

(a) Sector 11 2019 Light Curve, period ~0.668

(b) Sector 11 2019 Folded Light Curve

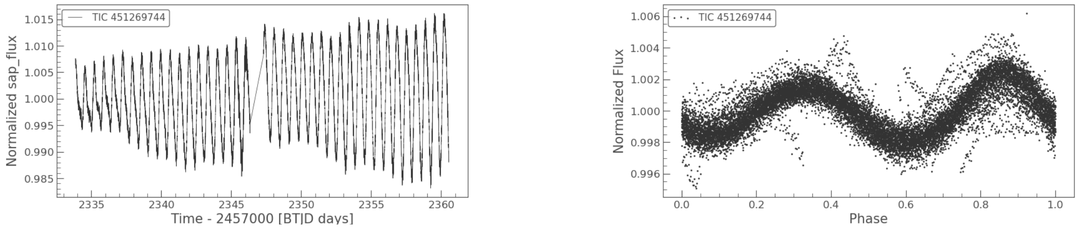

(c) Sector 38 2021 Light Curve, period ~0.674

(d) Sector 38 2021 Folded Light Curve

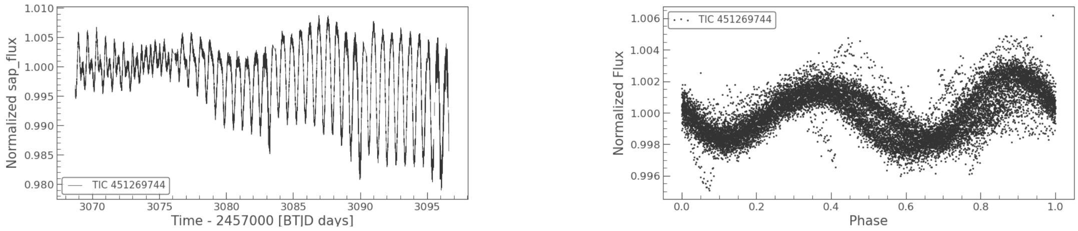

(e) Sector 65 2023 Light Curve, period ~0.676

(f) Sector 65 2023 Folded Light Curve

Figure 4.4.9: TESS photometric observations of HIP 71933 made in 2019, 2021 and 2023. The period of these plots is consistent with the rotation period of 0.67 days derived from the DI analysis (see Table 4.4.2). The data described here may be obtained from the MAST portal. The TESS Identification Catalog ID is shown for each graph (see discussion in Section 4.4.4).

5 DISCUSSION AND FUTURE WORK

Data from three different young late -F stars has been collected and reduced, from four different telescopes, including spot distribution, magnetic field topology and differential rotation measurement. How these characteristics compare to the values for other young solar-type stars, and what these comparisons can tell us about early Suns are in the subject of the discussion.

5.1 Photometric Analysis

All of the data used in DI and ZDI analysis for this thesis was collected from spectroscopic analysis using four telescopes (see discussion in Section 4). During the course of this study the TESS satellite made several pointed photometric observations of all three stars between 2018 and 2023. The results of these photometric observations are plotted in Sections 4.2.4, 4.3.4 and 4.4.4.

For stars with inclinations in the area of ~60° it is expected that the period identified with a photometric analysis will be more heavily weighted at the higher latitudes than the equator since this is where the majority of the star's surface is seen. It is assumed that solar-type stars will rotate differentially more slowly at higher latitudes than the equator since that is what the Sun does. This relation is represented by Equation 3.3.1. This equation is repeated here:

$$\Omega(\theta) = \Omega_{eq} - d\Omega sin^2\theta \tag{5.1.1}$$

where $\Omega(\theta)$ is the rotation rate at latitude θ in rad d^{-1}, Ω_{eq} is the equatorial rotation rate in rad $d^{-1}$and dΩ is the rotational shear between the equator and the poles (the DR in rad d^{-1}).

We would therefore expect to see rotation periods from the photometry data to be slightly longer than the equatorial rotation periods derived from the DI analysis. An estimate of the higher latitude rotation rates can be calculated using Equation 5.1.1 at a 60° latitude based upon the equatorial rotation rate derived from the DI analysis. Values for three rotation rates for each star are listed in Table 5.1.1:

Table 5.1.1: Calculated rotation rates of thesis stars at high latitude (+60°).

Star	Equatorial rotation (days)	Calculated high latitude rotation (days)	Photometric measured averaged rotation (days)
VXR 77A	0.653	0.647	0.648
HD 43989	1.167	1.440	1.360
HIP 71933	0.670	0.681	0.673

From this table it can be seen that VXR 77A and HD 43989 have a measured photometric rotation rate slower than equatorial as expected, whereas HIP 71933 is somewhat higher. The values measured however are roughly close to expected with the largest difference seen for HD 43989. Periods obtained from photometric measurements are subject to errors both instrumental as well as variabilty of the star's surface brightness and in general should not be as accurate as periods calculated from spectral measurements. Appendix D shows brightness and magnetic maps for each star at each epoch using rotation rates measured from the TESS photometric observations.

5.2 Differential Rotation

The surface temperature of a star is a major factor which will determine the size of the convection zone. Hotter stars will have thin convective zones and the coolest stars will have convective zones which are a substantial percentage of the star's radius, including nearly all of it (Böhm-Vitense, 1992). The transition between these two states is believed to occur approximately at the F5 spectral region of the HR diagram (Simon & Landsman, 1991; Wolff & Simon, 1997; Mizusawa et al., 2012; Seach et al., 2020). Hotter stars with thinner convective zones are expected to have higher rotational shear as the difference in rotational velocity at different latitudes is not as well smoothed out. A thinner convective zone could not redistribute angular momentum as well to counter rotational variation. Several observations have reported an increase in measured differential rotation versus hotter surface temperatures and thinning convective zones (Barnes et al., 2005; Küker et al., 2011; Marsden et al., 2011b; Mizusawa et al., 2012).

Figure 5.2.1 is a reproduction of Figure 2.4.1 ($d\Omega$ versus convection depth) with the three stars studied in this thesis added in red. Convection zone depths were calculated from models in Baraffe et al. (2015) as described in Section 2.4. Figure 5.2.2 is the $\mathrm{d}\Omega$ versus surface temperature.

The three stars in this study have convection zones roughly equal to or thinner than the convection zones in the review stars (see Figure 5.2.1), which are mostly early-G stars, as would be expected from the HR diagram. The higher DR would also be expected, although the limited χ^2 improvement from the DR value used with the DI and ZDI calculations for VXR 77A and HD 43989 make those DR values tentative.

5.3 Spot Features

Stokes *I* brightness maps for all epochs of VXR 77A is shown in Figure 4.2.3. Of these five epochs, the best are epoch 2005.09 from the AAT and Epoch 2018.07 from the 2.3-m telescope. From these two epochs are seen high latitude spot features with the strongest spots at the visible pole. There is more overall spots, especially at the visible pole in the 2005.09 than 2018.07, however the higher resolution of earlier epoch taken at the AAT could likely be responsible, allowing for more spots to be recovered. There is little change or evolution of spots between these two epochs, spanning over 13 years. Epoch 2012.04 in between these two epochs also shows the dominant spots at the visible pole with more low latitude spots.

Whereas there are only two observational epochs for HD 43989 in this study, there is additional data in the literature. Hackman et al. (2016) reports a magnetic field that is dominant in non-axisymmetric modes, unlike other late-F stars in the study. Activity cycles are seen by Kriskovics et al. (2019) and Willamo et al. (2022) with a ~1600 day cycle observed by Kriskovics et al. (2019). In this study HD 43989 is also seen to exhibit greater magnetic activity with more dynamic evolution of spots. Epoch 2008.94 from this study shows a significant off-center spot at the visible pole with light spots down to the equator.

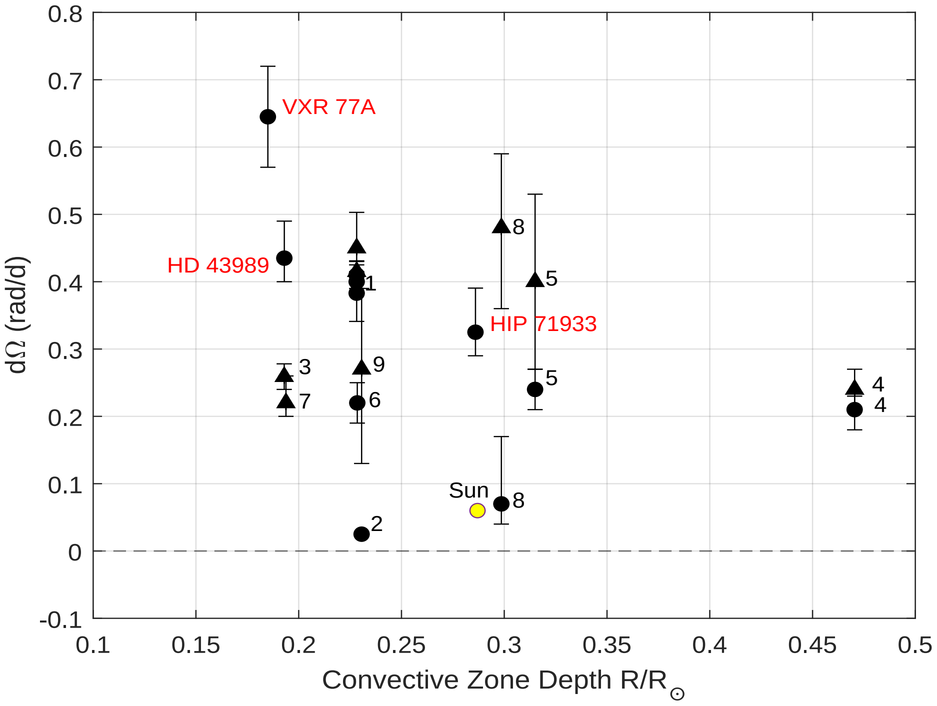

Figure 5.2.1: Surface differential shear $d\Omega$ versus convective zone depth as a function of solar radius for the stars in the literature review. Dots show surface differential shear from surface brightness analysis and triangles from surface magnetic analysis. The convective zone depth was calculated from evolutionary models in Baraffe et al. (2015). References cited are for the dΩ values. Errors are plotted where published. The value for the Sun's dΩ is taken from Küker & Rüdiger (2008). The value for the Sun's convective zone depth is taken from Hathaway (2022). This is a reproduction of Figure 2.4.1 with the three thesis stars added in red.

[1] HD 171488 (V889 Her), G2V (Marsden et al., 2006a), (Jeffers & Donati, 2011)
[2] HD 307938 (R58), G2V (Marsden et al., 2005)
[3] HR 1817, F8V (Marsden et al., 2006a)
[4] HD 106506, G1V (Waite et al., 2011)
[5] HD 141943, G2 C (Marsden et al., 2011a)
[6] HD 206860 (HN Pegasi), G0V (Boro Saikia et al., 2015)
age estimate for this star is from (Gaia et al., 2018)
[7] HD 35296, F8V (Waite et al., 2015)
[8] HD 29615, G3V (Waite et al., 2015)
[9] HD 12933 (EK Dra) , G1.5V (Waite et al., 2017)

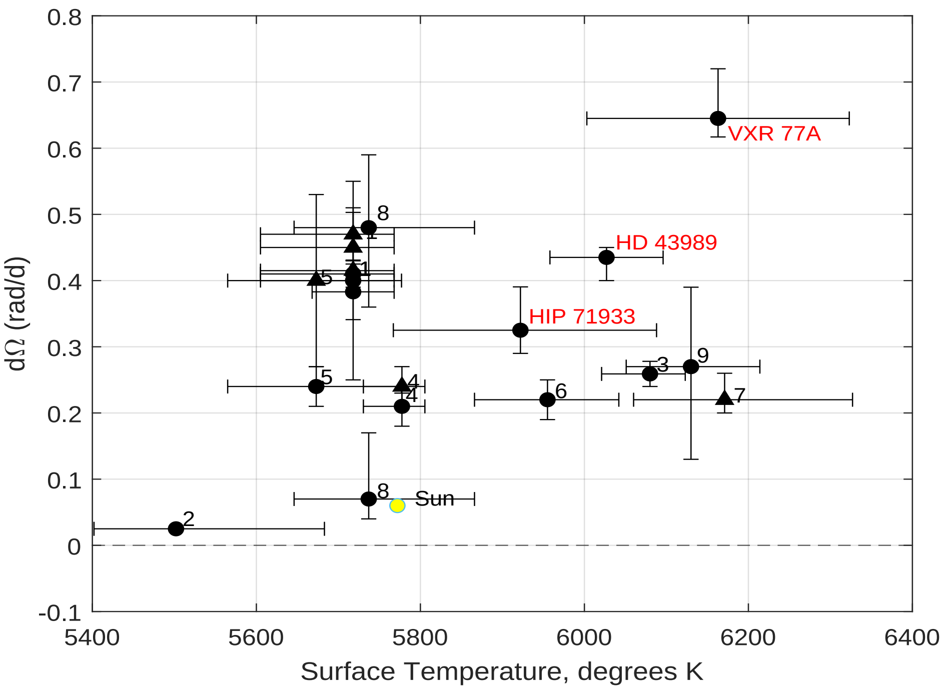

Figure 5.2.2: Surface differential shear $d\Omega$ versus photospheric temperature for the stars in the literature review. Dots show surface differential shear from surface brightness analysis and triangles from surface magnetic analysis. Values for differential shear are taken from the references below. Values for photospheric temperature are taken from Gaia DR 2 (Gaia et al., 2018). The three stars in this study are shown in red. These three stars have increasing surface temperatures and differential shear $d\Omega$ (see discussion in Section 5.2). The value for the Sun's dΩ is taken from Küker & Rüdiger (2008). The value for the Sun's surface temperature is taken from Hathaway (2022). This is a reproduction of Figure 2.4.2 with the three thesis stars added in red.

[1] HD 171488 (V889 Her), G2V (Marsden et al., 2006a; Jeffers & Donati, 2011)
[2] HD 307938 (R58), G2V (Marsden et al., 2005)
[3] HR 1817, F8V (Marsden et al., 2006a)
[4] HD 106506, G1V (Waite et al., 2011)
[5] HD 141943, G2 C (Marsden et al., 2011a)
[6] HD 206860 (HN Pegasi), G0V (Boro Saikia et al., 2015)
age estimate for this star is from (Gaia et al., 2018)
[7] HD 35296, F8V (Waite et al., 2015)
[8] HD 29615, G3V (Waite et al., 2015)
[9] HD 12933 (EK Dra) , G1.5V (Waite et al., 2017)

Off-center and non-axisymmetric spots has been observed on other solar-type stars including VW Cephei (G8V+K0V) (Hendry & Mochnacki, 2000), EK Draconis (G1.5V) (Senavci et al., 2021) and V530 Persei (G8V) (Cang et al., 2020). A persistent off-center polar spot on HD 43989 is reported by Kriskovics et al. (2019) during observations in December 2013. A little over ten years later epoch 2019.06 (this study) shows only a small spot directly at the visible pole with more extensive spots down to the stellar equator and below (see Figure 4.3.3).

Persistent spot features are seen throughout including a ring of spots at the +60°latitude and an absence of spots directly at the pole (see Figure 4.4.3). The ring-like structure is seen mostly at the +60°latitude with the exception of Epoch 2009.26 where there are additional spots between +40°and +60°latitudes. This could be a result of the superior resolution of the AAT, however there are fewer spots at these latitudes in Epoch 2011.37 with the even higher HARPSpol resolution. This could be due to spot evolution over the two year difference, or that the AAT observation was at the end of a cycle when the magnetic field was more active.

The number of spots in this ring varies between epochs, possibly because of spots are disappearing and reforming in a continuous cycle. The resolution of DI in general does not make it possible to determine if the clumps seen are a single spot formation of groups of smaller spots (Schüussler & Solanki, 1992; Solanki & Unruh, 2004). Barnes et al. (1998); Perugini et al. (2021); Senavci et al. (2021) imply that evolution of spots on rapidly-rotating stars should occur in short time periods, of weeks or months. The long-lasting nature of the ring on HIP 71933 could be because new spots are being added as old ones decay (Hughes et al., 2023).

Ring-like structures are occasionally seen on other young solar-type stars (Donati & Cameron, 1997; Marsden et al., 2006b; Alvarado-Gómez et al., 2015; Carter et al., 2015). The persistence of the +60°ring on HIP 71933 and the apparent lack of spots at the pole over the same period is unusual. Marsden et al. (2005) reported a similar phenomena from a study of R58 (HD 307938) (G2V in the young cluster IC2602). This star has a mass (1.18 $M_\odot$) a radius (1.18$R_\odot$) and an age (35 Myr) similar to HIP 71933 (see Table 4.4.2). An absence of spots was seen in the brightness maps produced by the DI calculations.

Most of the LSD profiles had a large dip in the center. Because the observations were made near a full moon, the dips were believed to be caused by solar contamination (reflected moonlight) which confused the star's RV with the terrestrial velocity toward it and interfered with the LSD computations. This created dips in the profiles which interfered with the spot recovery at the visible pole. There is a similar structure seen in the LSD profiles of HIP 71933 for epoch 2009.34 (see Figure A.3.2), although this dip is much smaller than that reported by Marsden et al. (2005) for R58.

By continuing to adjust the $v\sin i$ value as described in Section 3.2.1 this additional structure (dip) can be removed by using a $v\sin i$ of 74 km s^{-1}which improved the fit and eliminates the dip in the profile. This resulted in the appearance of additional spots above the +60° latitude, however the center of the pole is still absent of spots. (see Figure A.3.2).

Lowering the $v\sin i$ results in additional spots above the +60°latitude in the brightness maps for all of the observing epochs of HIP 71933, however this value results in an unreliable statistical fit (Skilling & Bryan, 1984) for all epochs except Epoch 2009.34. A $v\sin i$ of 76 km $s^{-1}$is the only value that produces an acceptable statistical fit for all epochs. The $v\sin i$ value should not vary across observing epochs. The value of 74 km s^{-1}needed to provide the best fit for Epoch 2009.34 might be attributed to the poorer stability of the 2.3-m telescope spectrograph as well as the poorer phase coverage for that observation (Hughes et al., 2023).

The position and phase of the Moon for each of the epochs recorded for HIP 71933 was obtained using an ephermis (Espenak, 1999; Peat, 2022). The Moon was not close to HIP 71933 in any of the observations, and was below the horizon for one. Only small dips are seen in Epoch 2009.34 (see Figure A.3.2) and do not see any of the extreme dips reported by Marsden et al. (2005). For these reasons solar contamination or poor fits has been discounted as the reason for the lack of spots at the visible pole (Hughes et al., 2023).

Dynamo models have been tested in other numerical simulations and have produced wreath-like structures on rapidly-rotating stars, including rings surrounding a polar spot with opposite polarity (Granzer et al., 2000; Schrijver & Title, 2001). Other simulations result in clusters that appear 180°apart in a high-latitude structure (Holzwarth, 2004) (see discussion in Sections 2.2 and 2.3). HIP 71933 meets the mass criteria of Schrijver & Title (2001) (1.0 - 1.7$M_\odot$) and spot clusters 180°apart are visible in Epochs 2009.34 and 2011.37. Other epochs (2012.26 and 2019.46) have clusters that are not exactly 180°apart (see Figure 4.4.3). The rings on HIP 71933 are azimuthal (corresponding to azimuthal magnetic fields seen in magnetic maps in Figures 4.4.4 and 4.4.5) and highly axisymmetric, however there is no strong spot feature at the visible pole that is seen in the simulations.

The observations of HIP 71933 in this study consistently lack polar spots throughout the ten year observation period. The LSD profiles do not have the flat bottom profiles that have been associated with dark polar spots on other stars. There is a data gap of six six years between 2012 and 2018 however the brightness maps are similar on either side of this gap. Strong polar spots are seen on other young solar-type stars observed with the same instruments including (Mengel, 2005; Waite et al., 2011; Perugini et al., 2021) and this thesis. This suggests that the absence of polar spots is a real feature of HIP 71933 during these observations. It appears that HIP 71933 an unusually rapidly-rotating star without a polar spot (Hughes et al., 2023).

5.4 Magnetic Data Analysis

There are four epochs in this study which were made with a spectropolarimeter, epochs 2008.94 and 2019.06 for HD 43989 and epochs 2009.26 and 2011.37 for HIP 71933. There are therefore magnetic maps in addition to brightness maps for these epochs.

Epoch 2008.94 for HD 43989, as discussed earlier, shows an off-center polar spot in the brightness map. There is a strong azimuthal field from the pole throughout the entire visible hemisphere of the star, with a small absence of azimuthal magnetic energy directly at the pole. Ten years later in epoch 2019.06 the small spot directly at the visible pole is replaced by negative azimuthal field energy and also surrounded by positive azimuthal field energy with a partial ring of negative azimuthal energy at the +60°latitude (see Figures 4.3.4 and 4.3.5). The magnetic quantities derived from the ZDI process indicate a complex field with epoch 2008.94 having slightly more toroidal energy (57^{+6}_{-1}%) and epoch 2019.06 approximately even (poloidal 51^{+7}_{-11}%). In both epochs the majority of the magnetic field energy is distributed in the higher multipoles ($l \geq 4$) (see Table 4.3.3).

These results might indicate that HD 43989 was undergoing one or more magnetic field reversals between these epochs. Kriskovics et al. (2019) reported a photometric cycle for HD 43989 (referred to as V1358 Ori) of ~1600 days based upon analysis of long-term photometric data. Figure 5.4.1 is taken from (Kriskovics et al., 2019) Figure 1, with vertical bars showing the HJD of the observations of the two HD 43989 observations in this study. Extrapolating the fitted curve in Figure 5.4.1 might suggest that HD 43989 is observed just before the beginning of a magnetic reversal at epoch 2008.94 and just before a reversal in epoch 2019.06. An examination of the magnetic maps for HD 43989 (see Figures 4.3.4 and 4.3.5) might indicate the beginning of a reversal, particularly in the azimuthal maps.

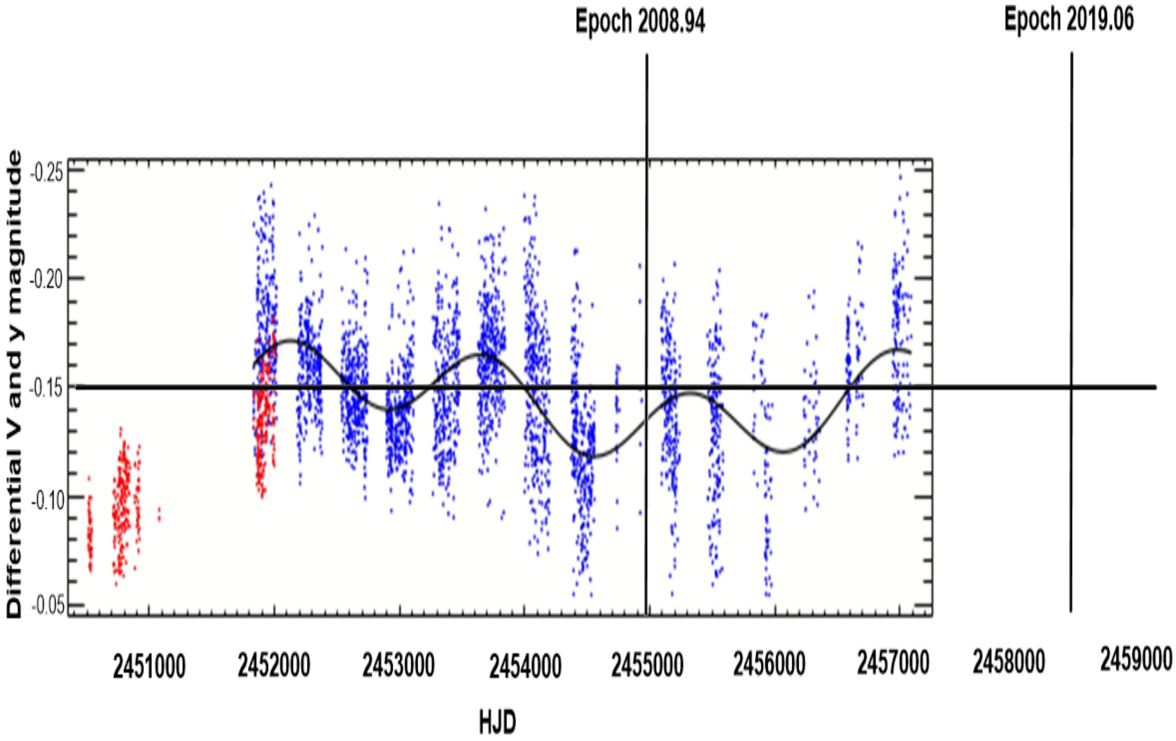

Figure 5.4.1: Photometry in the Strömgren *y* (red) and Johnson *V* (blue) for HD 43989. This figure taken from Kriskovics et al. (2019, Figure 1) annotated with a vertical bar at the HJD of the two epochs in this study.

Similarly to HD 43989 there are two observations of the seven for HIP 71933 that were recorded with a spectropolarimeter, epoch 2009.26 at the AAT and epoch 2011.37 at the La Silla Observatory 3.6-m telescope. Of these two observations, epoch 2009.26 has the superior phase coverage. Unlike HD 43989 which has a complex magnetic field, both epochs for HIP 71933 have structures that are similar with the dominant field energy being poloidald (94^{+1}_{-0}% for Epoch 2009.26 and 83^{+2}_{-3}% for Epoch 2011.37). The radial field is predominantly positive in polarity throughout the visible hemisphere of the star and possibly in the non-visible hemisphere. There is little change between the two epochs compared to HD 43989, possibly indicating a long period of stability.

The ring of spots in the brightness maps is not as well defined in the corresponding magnetic maps (see Figures 4.4.4 and 4.4.5) although they do appear to be aligned. The azimuthal ring seen in all the brightness maps is visible as a negative azimuthal field surrounding the +60° latitude at the visible pole. The poloidal field dominates both epochs with the majority of the energy in the first level multipole ($l = 1$). This is unlike most of the solar-type stars where there is a greater balance between poloidal and toroidal magnetic field strength (see the review in Section 2, Figure 2.7.1). The poloidal fields for HIP 71933 in the two epochs in this study are of a higher percentage than any of the other studies (see Table 4.4.3) , showing that young solar-type stars can have a dominant poloidal field at some times.

The field strengths for Epoch 2011.37 are much higher than that recovered for epoch 2009.26 (see Figures 4.4.4 and 4.4.5). Changes in the difference between poloidal and toroidal field strengths could be migrations of the magnetic field. The small difference seen in the two epochs of HIP 71933 (94% vs 83%) cannot explain the significant difference in the magnetic maps. The additional resolution of the spectropolarimeters more likely allowed for more recovery of the magnetic field at the observation using the HARPSpol spectropolarimeter (epoch 2011.37). It is likely that the large differences in field strength between epoch 2009.26 and 2011.37 are instrumental, and the distributions and percentages of field quantities in these two epochs is of more important interest.

During solar minimums the Sun has a dominant poloidal field when the internal toroidal field is at a maximum (Munoz-Jaramillo et al., 2008). Studies of young solar-type stars indicate that young rapidly-rotating stars should possess a large toroidal component in the magnetic fields on their surfaces (Petit et al., 2008) (see Figure 2.7.1). The dominance of the poloidal field strength and lack of latitudinal evolution of the spots seen in the brightness maps and the stability of the ring structure in the brightness maps may indicate that HIP 71933 was observed during a low-activity cycle (Hughes et al., 2023). The strong azimuthal field component present in the magnetic maps of both HD 43989 and HIP 71933 is similar to magnetic maps seen in other young, solar-type stars such as HD 141943 (Marsden et al., 2011a), HD 106506 (Waite et al., 2011), and HD 35296 and HD 29615 (Waite et al., 2015). Donati et al. (2003) interpret strong azimuthal fields at the surface of a star as being caused by dynamo processes directly throughout the convection zone. Brown et al. (2010) conducted MHD simulations which found that strong magnetic wreaths are constructed within the convection zones of stars rotating more rapidly than the Sun, without any interaction from a tacholine. The results seen on HD 43989 and HIP 71933 therefore indicate a non-solar type dynamo at work in these stars.

If the simulation analysis by Hackman et al. (2024) is accurate (see discussion in Section 2.7) then the most reliable data collected in this study is the ratio between poloidal and toroidal magnetic field energies, as well as the spot images in the brightness maps. The three stars span a range from above and below the $v\sin i$ and inclination best values cited by (Hackman et al., 2024) for the best magnetic field recovery.

5.5 Poloidal versus Toroidal Percentages

Figure 5.5.1 plots the percentage of toroidal magnetic field energy versus rotation period for all the stars in the literature review as well as HD 43989 and HIP 71933 from this study, for which magnetic data is available. These two stars are on average hotter and younger than those in the review (Section 2) and are faster rotators. HIP 71933 displays an unusually low percentage of toroidal magnetic energy for a rapidly rotating star.

5.6 Convective Zone Depth and Differential Shear

Küker & Rüdiger (2005) studied the physics of convection zone heat transfer in solar-type stars and conclude that surface differential shear should increase upon increasing surface temperature, including increasing convective zone turnover times, at least from the lower main sequence up to F-type stars. Observations of stars across these spectral classes support this view (Barnes et al., 2005; Küker & Rüdiger, 2007). However our examination of the literature review stars indicates some stars of nearly the same surface temperature have a range of differential shear values (see Figure 5.2.2). The depth of the convective zone may also be a factor in the differential shear, perhaps more important that the star's spectral type (surface temperature) (Waite et al., 2011). Deeper convection zones would distribute

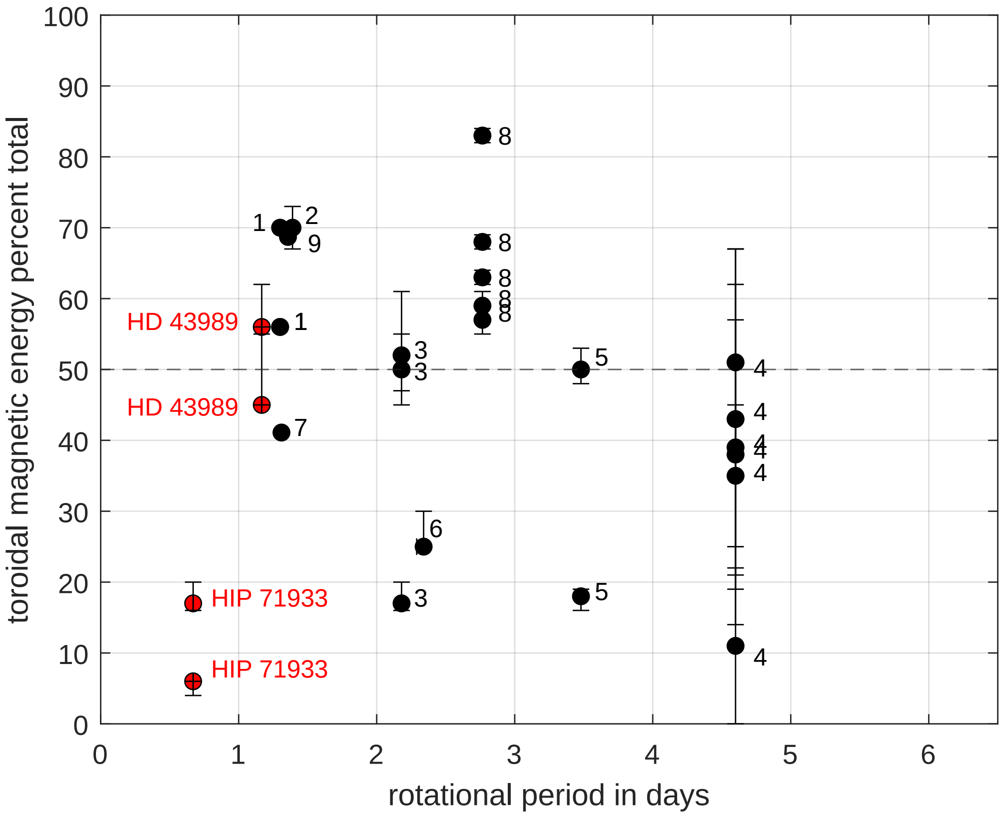

Figure 5.5.1: Percent of toroidal magnetic field energy for the literature review stars with Stokes *V* data vs. rotational period. Stars with multiple epochs of ZDI observations are plotted as individual points. Errors are plotted where published. This is a reproduction of Figure 2.7.1 with the stars in this study added in red.

[1] HD 171488 (V889 Her), G2V (Jeffers & Donati, 2011) Epochs 2007.39 and 2007.77
[2] HD 106506, G1V, (Waite et al., 2011), Epoch 2007.24
[3] HD 141943, G2V, (Marsden et al., 2011a), Epochs 2007.26, 2009.27, 2010.24
[4] HD 206860 (HN Pegasi), G0V, (Boro Saikia et al., 2015), Epochs 2007.67, 2008.71, 2009.54, 2010.62, 2011.67, 2013.68
[5] HD 35296, F8V, (Waite et al., 2015), Epochs 2007.06, 2008.05
[6] HD 29615, G3V, (Waite et al., 2015), Epoch 2009.90
[7] HD 36869 (AH Lep), G3V, (Hackman et al., 2016), Epoch 2009.69
[8] HD 129333 (AH Lep), G1.5V, (Waite et al., 2017), Epochs 2006.99, 2007.07, 2007.08, 2008.06, 2012.03
[9] HD 43989 (V1358 Ori), F8V, (Hackman et al., 2016), Epoch 2013.09

angular momentum throughout the zone resulting in a higher overall shear as seen at the star's surface. Figures 5.2.2 and Figure 5.2.1 place HIP 71933 in fair support of these assumptions. VXR 77A and HD 43989 shown in Figure 5.2.2 also support the notion that a higher surface temperature will increase differential shear, but their placement in Figure 5.2.1 is not consistent with the other stars. The differential shear values derived in this study for VXR 77A and HD 43989 are not as reliable as that obtained for HIP 71933 so any conjectures about these stars is not as dependable.

5.7 Radial Velocity and the Possibility of Companions

RV estimates were made as a part of the DI process for all three stars. The RV value derived for HD 43989 was unchanged through epochs across ten years. Some variation was seen for both VXR 77A and HIP 71933 for which there is a larger number of epochs observed.

Figures 4.2.6 and 4.4.8 show plots of the RV values derived for VXR 77A and HIP 71933. There is not enough data to identify a close-orbiting companion, however both plots suggest a periodic reflex. Stars who have known visual binaries have been recorded with RVs of single digit km s^{-1}(Katoh et al., 2018). The RV changes recorded in this study for VXR 77A and HIP 71933 are several times larger and might indicate a large exoplanet, or possibly a small stellar companion.

If either VXR 77A or HIP 71933 are binary stars, a companion might be seen in the LSD profiles. Secondary stars may be seen if the LSD signature is sufficiently large and the velocity space wide enough (Marsden et al., 2005; Lavail et al., 2020; Lehmann et al., 2020). There is so far no report in the literature for VXR 77A as a suspected binary. As mentioned in Section 4.4.3, HIP 71933 has been identified as a possible binary star (Desidera et al., 2015).

A large companion orbiting a star might affect the spin rate by tidal action, thus increasing the magnetic activity (Poppenhaeger et al., 2014). Sanchis-Ojeda & Winn (2011) observed what they believed to be a mis-aligned super Neptune-sized planet orbiting HAT-P-11 (a mature K4V star), along with the possibility of an active spot latitude of +60°, although this cannot be necessarily tied to the suspected exoplanet. Could the +60°ring observed on HIP 71933 as well as the spot clumps within this ring be caused by tidal influences of a large companion (see discussion of opposite spot clumps in Sections 2.2 and 2.3)? The stars studied in (Poppenhaeger et al., 2014) were mostly older (> 1Gyr) and there is no evidence of a companion in the LSD profiles for either VXR 77A or HIP 71933, however these two stars might be good candidates in the relatively new study of star-planet interactions, including searching for exoplanets and surface studies of X-rays.

5.8 Conclusion

Three late-F stars have been analyzed from data collected at four telescopes between late 2003 and early 2019 for a total of fourteen observing epochs, for the purpose of comparing their fundamental parameters and magnetic characteristics against late -F to mid -G stars currently in the literature. Values derived using DI for $v\sin i$ and rotational period are consistent with the G-type stars in the literature review. Values derived for DR from the Stokes I data were on average higher than the same stars which was expected for hotter stars.

The spot maps from two of the stars (VXR 77A and HD 43989) exhibited a large slightly off center polar spot consistent with the stars in the literature review. HD 43989 has an off-center polar spot in the first epoch, which is largely gone by the second epoch ten years later, with an increase in the spot distribution at lower latitudes. HIP 71933 exhibits a lack of spots at the pole in all epochs of with a persistent ring of spots at the +60°latitude. There appears to be spot movement throughout each epoch but it is limited to the ring with little change in latitude of spots over the seven epochs.

Magnetic field maps for HD 43989 indicate a complex magnetic field with most of the energy in the higher multipole (*l*≥4) with a dominant toroidal field in the first epoch and a dominant poloidal field in the second epoch. Previous studies of HD 43989 report a magnetic cycle of ~1600 days and HD 43989 might be seen at different places on this cycle. HIP 71933 has azimuthal wreaths with the magnetic field energy mostly poloidal. The azimuthal ring appears to be consistent with the spot maps. Wreathes appear on other young solar-type stars, but a dominant poloidal field in a rapidly-rotating star is more rare. The field is strongly dipolar and axisymmetric and there is no evidence in HIP 71933 of a solar-like cycle. The relatively long-term stability of HIP 71933 may be influenced by a fossil field component which would expand the current theories as to the threshold between fossil and dynamo-driven magnetic fields. It also is possible that the observational epochs of HIP 71933 in this study are just made during a period of low activity. In either case, the presence of strong azimuthal fields on the surface of HD 43989 and HIP 71933 and the significant surface DR indicate a dynamo mechanism present throughout the convection zone of the stars.

Variations in the RV measurements of HD 43989 and HIP 71933 as well as spot features on HIP 71933 indicate the possibility of a large companion. This could be a large exoplanet or a secondary star. Although there is no evidence of a secondary in the LSD profiles of either star, a small companion might still be present. This is supported by previous studies indicating that HIP 71933 might be a Spectroscopic Binary as mentioned in Section 5.7.

5.9 Future Work

5.9.1 Further Observations

Of the three stars analysed in this study VXR 77A and HD 43989 closely match similar stars in the literature review, in the existence of dominant polar spots and the calculated size of the convection zones. Where there is not enough data in this study to determine any cyclic activity in VXR 77A, there is some evidence of magnetic cycle in HD 43989 consistent with previous studies. HIP 71933 differs in that there is little spot evolution during ten years of observation or any significant changes in the magnetic field topology. Additional observations should be made of HD 43989 in order to further solidify the period of the magnetic field transitions and to determine the level of complexity of these transitions. With HIP 71933 little spot evolution is seen over ten years and little change in the magnetic field topology from two spectro-polarimetric observations over two years, during which time the poloidal field components is dominant, which is unusual for a young rapidly-rotating star. Its spectral class is just late of the believed transition point between dominance of fossil field to dynamo-driven field. This star warrants further spectro-polarimetric observation over a longer time period to see if the apparent stability of the surface features continues and to further attempt to characterize the source of its magnetic field.

5.9.2 Infrared Emissions from Spots

Infrared spectra from OH (Hydroxide) molecules has been detected in the Sun (Hall, 1973) and later in stellar spectra (Beer et al., 1972; Grevesse et al., 1984). During a study of starspots on active stars O'Neal & Neff (1997) and O'Neal et al. (2001) reported a near linear relationship between the OH equivalent width ratio EWR and T_{eff} (see Tang et al. (2024, and references therein)). Catalano et al. (2002) exploited this process to measure the IR changes in the effective temperature (T_{eff}) in spots as a way to measure the star's rotational period (P_{rot}).

Tang et al. (2024) further develop this technique by utilizing OH/Fe line depth ratios to estimate the star's T_{eff} and P_{rot} through periodic LDR and EWR variations in T Tauri stars (TTS). Target stars with known values of T_{eff} are used to create a database of T_{eff} - EWR relationships by measuring the EWR values in the OH infrared spectrum of these stars. This database can then be used to estimate the T_{eff} from a measurement of the EWR of the OH spectra.

For these stars, Tang et al. (2024) observed a periodicity of EWR, LDR and RV that closely tracked the same rotational period of the star by a light curve analysis. For the stars studied in this thesis, HIP 71933 has the most observation periods over the longest period of time. This star would be a good target to continue testing the techniques described by Tang et al. (2024), using the same observational datasets, since T_{eff} and P_{rot} were derived or refined from the DI analysis.

5.9.3 Analysis of Prominences from the Line Spectra

Donati et al. (1999) and Donati et al. (2000b) analyzed the broadening of the Hα emission profile from the T Tauri stars AB Doradus (K0) and LQ Lup (RX J1508.6-4423) (G8IV) using a method developed by Marsh & Horne (1988) to create maps of accretion disks from observations of line profiles. In this way they convert Hα spectra into Doppler maps assuming that this spectra is also rotating along with the star. This provides additional information about the star's differential rotation along with that obtained by the conventional DI methods described in Section 3.2.1. In addition the analysis of the concentrations of these maps were found to correspond to brightness features recovered from the DI analysis of the two stars. As the concentrations of these Hα lines are believed to be induced by prominences, this provides additional qualitative information about the prominences such as how the lines are modulated along with the star's rotation. This can be cross-checked against the DI results and can lead to estimates about momentum loss and resulting rotational braking time scales.

Like with the previous discussion concerning IR in spots, data sets used in this thesis, especially for HIP 71933 can also be analyzed to see if there are similar correlations. This analysis might further refine DR estimates for these stars as well as rotational braking estimates for these young late-F stars.

5.9.4 Principal Component Analysis

Principal Component Analysis (PCA) is a mathematical technique which captures the largest variation of data in a large data set and transforms this data onto a smaller data set. It has roots back to mathematical work done by Carl Gauss in the 19th century but was later refined by Karl Pearson and Harold Hotelling in the early 20th century (Pearson, 1901; Hotelling, 1933). The basic idea is to reduce the number of variables in a data set while preserving the maximum amount of information. This is done for the sake of simplicity and comes at a cost of reducing accuracy. This is accomplished by creating "principle components" which are linear combinations of initial variables and compressing information from the initial variables into the first component with remaining information in subsequent components. The result is a smaller dataset that is easier to analyze and visualize requiring less compute time.

Semel et al. (2006) outlines the use of this technique in lieu of ZDI in which synthetic spectra for a range of possible magnetic field parameters are compressed into principal components that represent the synthetic (calculated) spectra. These principal components are expressed as eigenvectors that are common for all of the models in the database. From a large database of calculated synthetic spectra based upon all possible magnetic field strengths and orientations a smaller database of principle components is created.

Lehmann & Donati (2022) used this technique to evaluate the magnetic field characteristics of two stars CE Boo (M3V) and DS Leo (M1V) and found that analysis of the initial principle components of the spectral data (in the form of the Stokes *V* LSD profiles) were in close agreement with the ZDI maps and were able to reveal additional information about the axisymmetry and mean field complexity. Of the two stars in this thesis for which there is Stokes *V* data available, HIP 71933 has the most data over the longer period. Use of PCA with the existing spectro-polarimetric data for this star could enhance the ZDI maps with additional detail as seen by Lehmann & Donati (2022). This information might provide more clues as to the apparent long-term stability of the magnetic field this study observed over 10 years for HIP 71933.

5.9.5 Surface Activity in the Search for Exoplanets

Surface activity is known to frustrate the search for exoplanet signals in the spectra of stars. Spot activity can be mistaken for RV velocites caused by an exoplanet influence on the host star (Saar & Donahue, 1997; Santos et al., 2000) Several techniques have been developed in an attempt to measure and possibly subtract surface activity, including spot modelling and measurement of chromospheric indices (Aigrain et al., 2012; Vilela et al., 2014; Santos et al., 2014; Dumusque et al., 2014). Spots can be difficult to model as there are problems with temporal variability (spots can evolve rapidly), degeneracies (different combinations of spots can produce similar observational effects) and overall complexity. Chromospheric indices have similar problems in that there are time variations in the spectral lines and degeneracy in the interpretation.

DI techniques using Maximum Entropy image reconstruction as those described in this thesis can help to separate activity-induced RV signals from real RV values (caused by the stellar reflex due to an exoplanet or exoplanets) because of the models that predict the effect of the spot on a line profile. This can still be confused by the greater spot complexity that appear on young solar-type stars. This complexity can be further reduced by attempting to perform periodicity analysis on the residuals between measured LSD profiles against the synthetic profiles produced by the modelling. Brown et al. (2024) explores the use of Gaussian process regression (GPR) which attempts to model the activity-induced RV signals as Gaussian noise. This method encounters difficulty with stars that have long-lived polar spots, a feature seen in most rapidly-rotating solar-type stars (see discussions in the review in Section 2). This is because of the different decay-time scales of these polar spots against the lower latitude spots. Other difficulties occur with insufficient observation time scales needed to record long-term RV variations.

The stellar characteristics derived in this thesis for HIP 71933 might make this data a good candidate to test these techniques further, as previously stated, HIP 71933 appears to be a rapidly-rotating young solar-analogue without a polar spot, and the extended time period of available data used in this thesis. Again, as with the previous discussions the existing data for HIP 71933 used in this thesis could be used as is for this study.

5.9.6 Deep Learning for use in Dopper and Zeeman Doppler Imaging

It is practically impossible to include a section in any scientific thesis about future work without discussion about the recent explosion in deep learning and machine learning, and how it might apply to the type of research done herein. There exists a large and growing data set from past and future surveys from which to train AI models against existing algorithms to improve the accuracy, the ability to handle complexity of the models and to discover new patterns and relationships between parameters. Neural network models could be trained using supervised learning to determine what kind of magnetic field topology would best represent a set of observed LSD profiles for a young solar-type star, and what type of dynamos would produce those magnetic fields. For those wishing to learn the techniques of deep learning, any of the existing data (but especially the high quality data for HIP 71933) from this research could be used to train a neural network to produce synthetic LSD profiles that are a close match to the observed profiles. Later incorporation of data sets from observations of other stars would then be used to improve the derivation of stellar parameters. Such an application of deep learning would also represent a useful research training exercise with further potential applications to other areas of astronomy. Reference (Baron, 2019, and references therein).

A MAXIMUM ENTROPY FITS

Figures A.1.1 through A.3.7 are the Stokes *I* maximum entropy fits for each epoch. The red lines are the original LSD profiles and the black lines are the fits calculated by the Doppler Imaging code.

Figure A.3.2 additionally shows brightness maps for different values of $v\sin i$ along with the associated fits in order to illustrate the unusual spotting features of the star (HIP 71933). This is further discussed in Section 5.3.

A.1 VXR77A

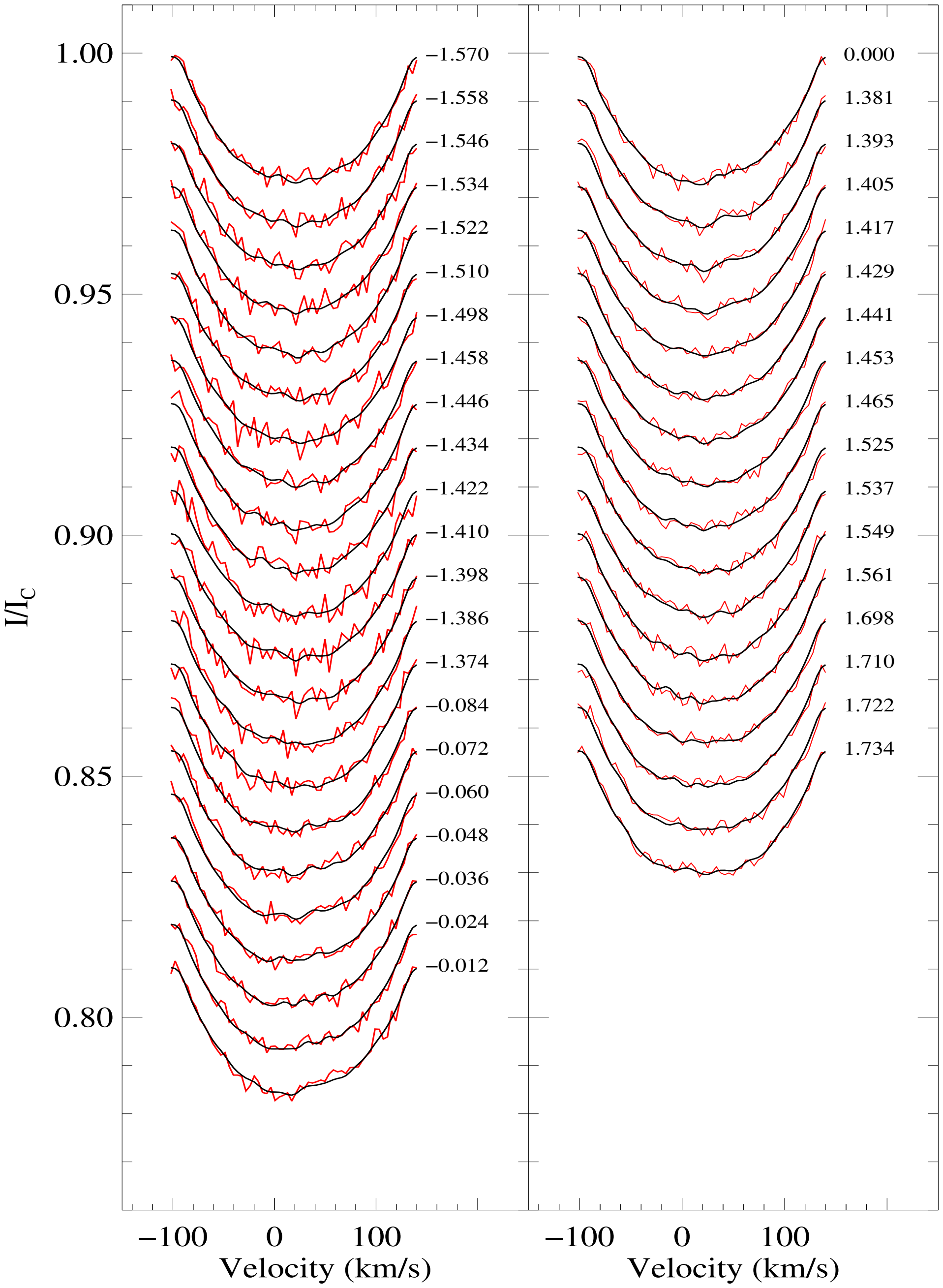

Figure A.1.1: Maximum entropy fits to the Stokes *I* LSD profiles for VXR77A observed at the AAT in December 2003 epoch 2003.92. The red lines represent the observed LSD profiles while the black lines represent the fits to the profiles produced by the Doppler Imaging code. Rotational phases for each observation are indicated to the right. Each profile is shifted for graphical purposes. Observation logs report heavy cloud cover for most of the exposures, making the fits noisy. The velocity step for this plot only was doubled in order to provide a cleaner appearance of the fits.

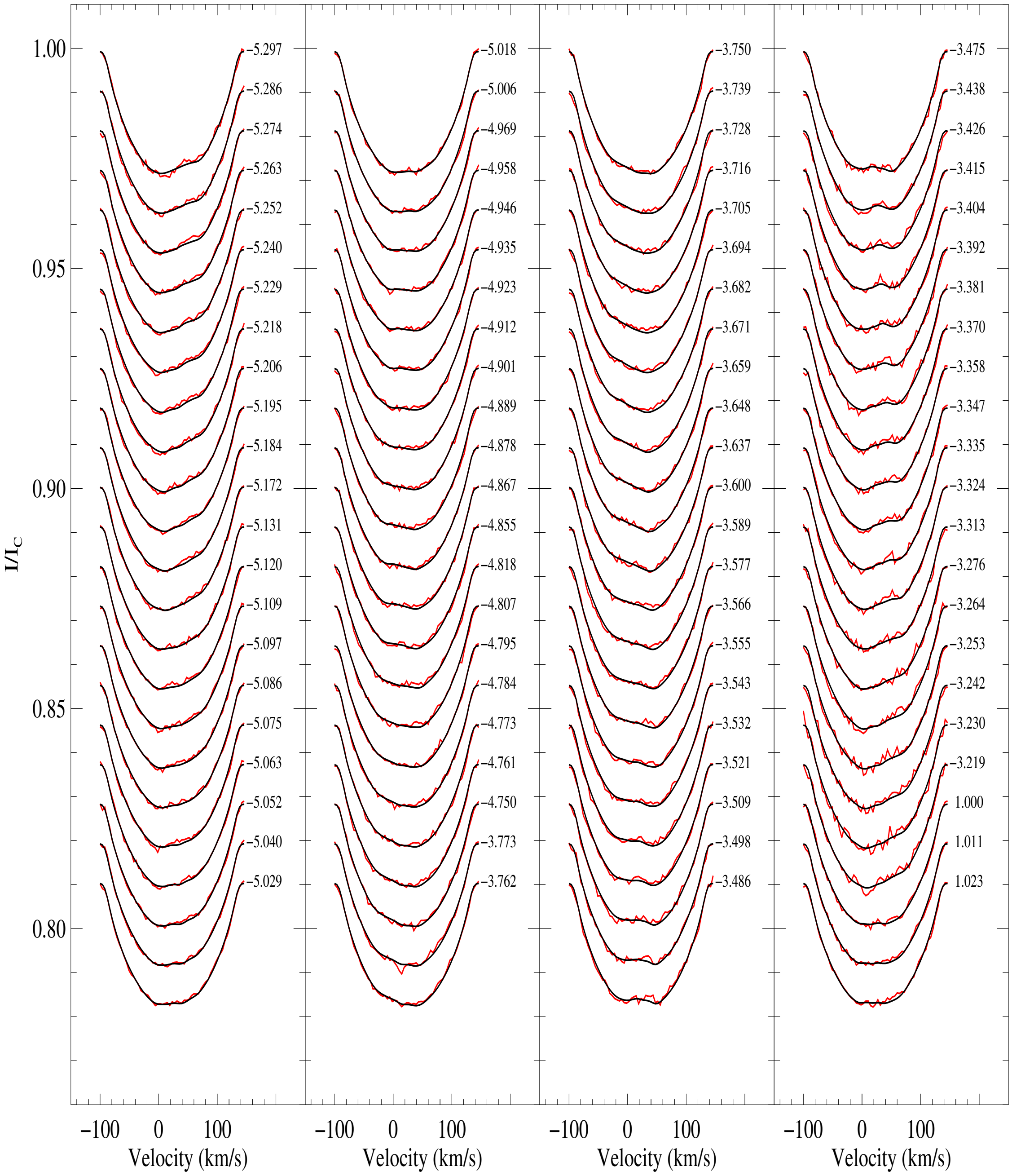

Figure A.1.2: Maximum entropy fits to the Stokes *I* LSD profiles for VXR77A observed at the AAT in February 2005 epoch 2005.09. The plot details are the same as in Figure A.1.1 for epoch 2003.92.

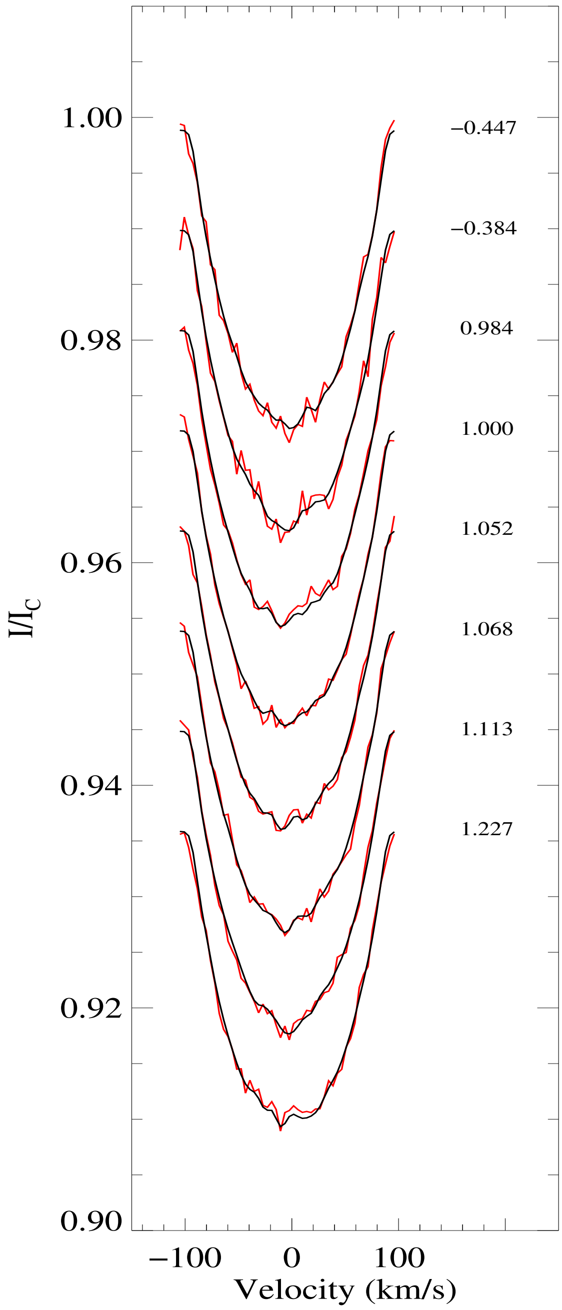

Figure A.1.3: Maximum entropy fits to the Stokes *I* LSD profiles for VXR77A at the 2.3-m telescope in January 2012 epoch 2012.04. The plot details are the same as in Figure A.1.1 for Epoch 2003.92.

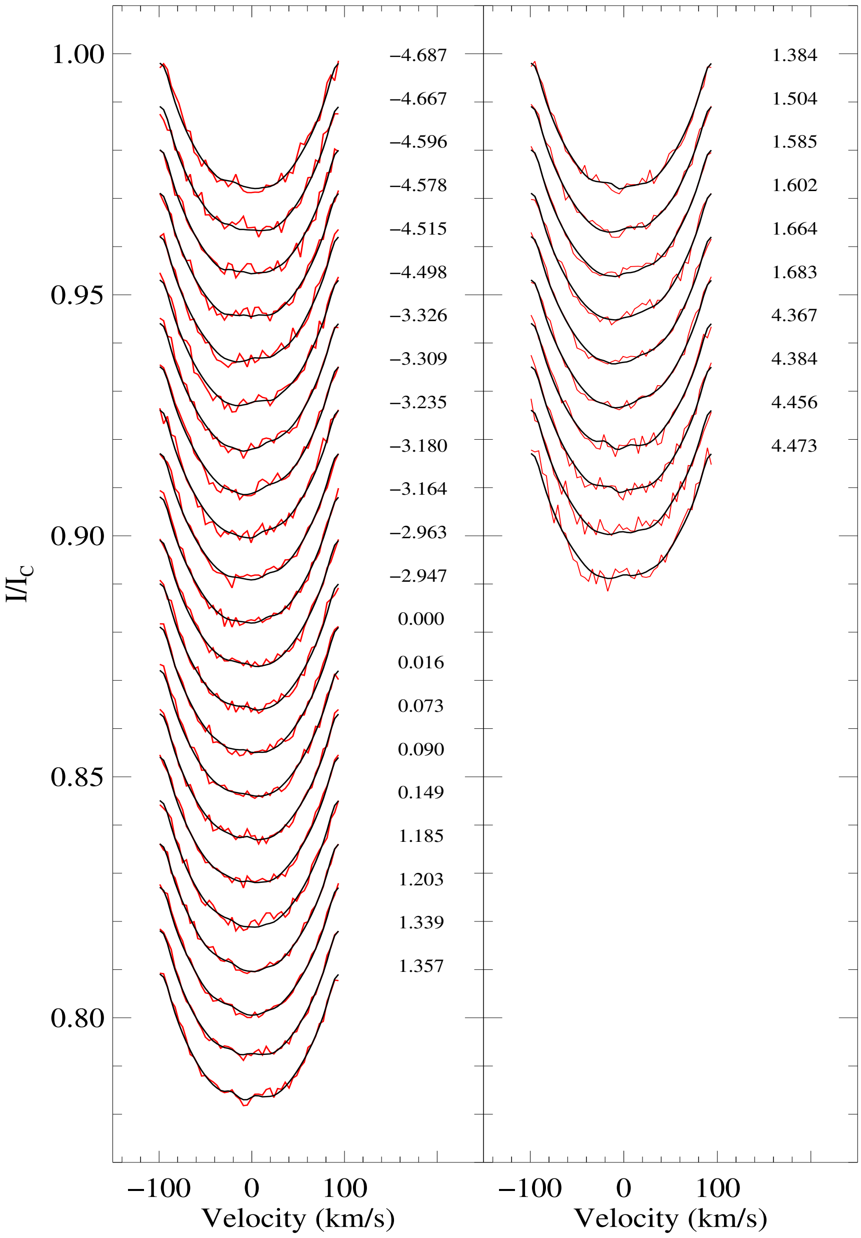

Figure A.1.4: Maximum entropy fits to the Stokes *I* LSD profiles for VXR77A at the 2.3-m telescope in January 2018 epoch 2018.07. The plot details are the same as in Figure A.1.1 for Epoch 2003.92.

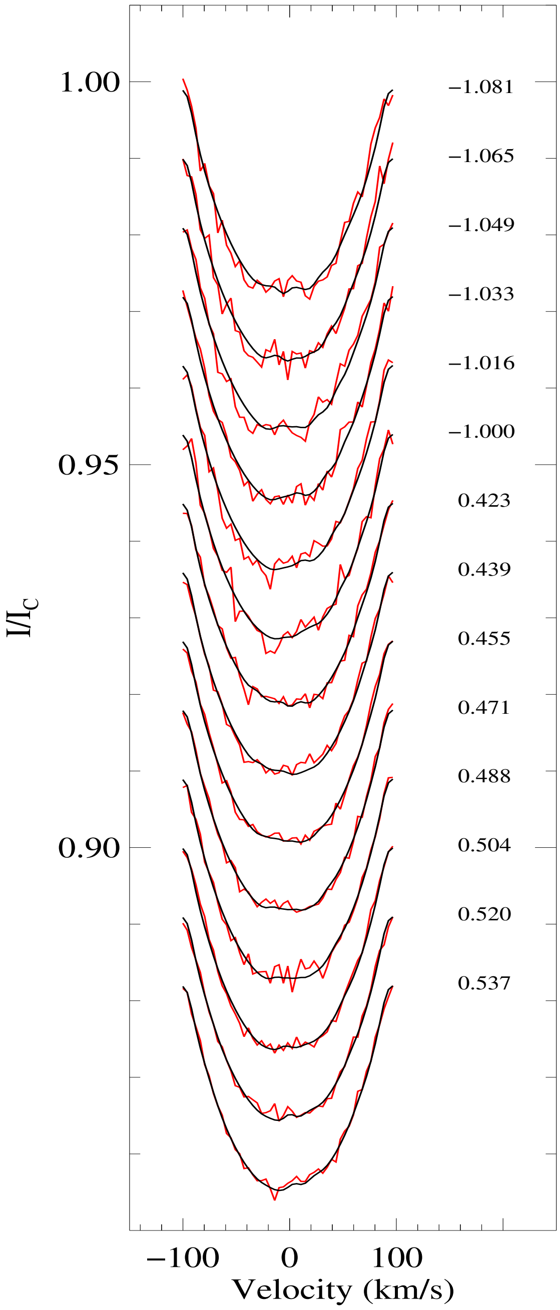

Figure A.1.5: Maximum entropy fits to the Stokes *I* LSD profiles for VXR77A at the 2.3-m telescope in September 2018 epoch 2018.72. The plot details are the same as in Figure A.1.1 for epoch 2003.92.

A.2 HD 43989

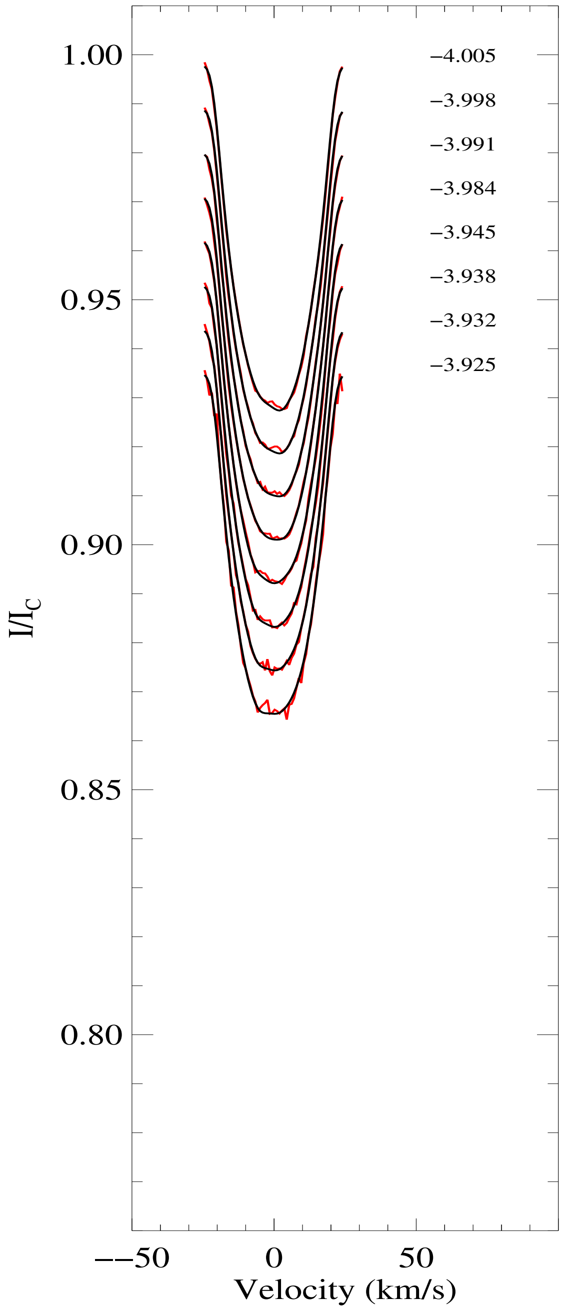

Figure A.2.1: Maximum entropy fits to the Stokes *I* LSD profiles for HD 43989 at the AAT in December 2008 epoch 2008.94. The plot details are the same as in Figure A.1.1.

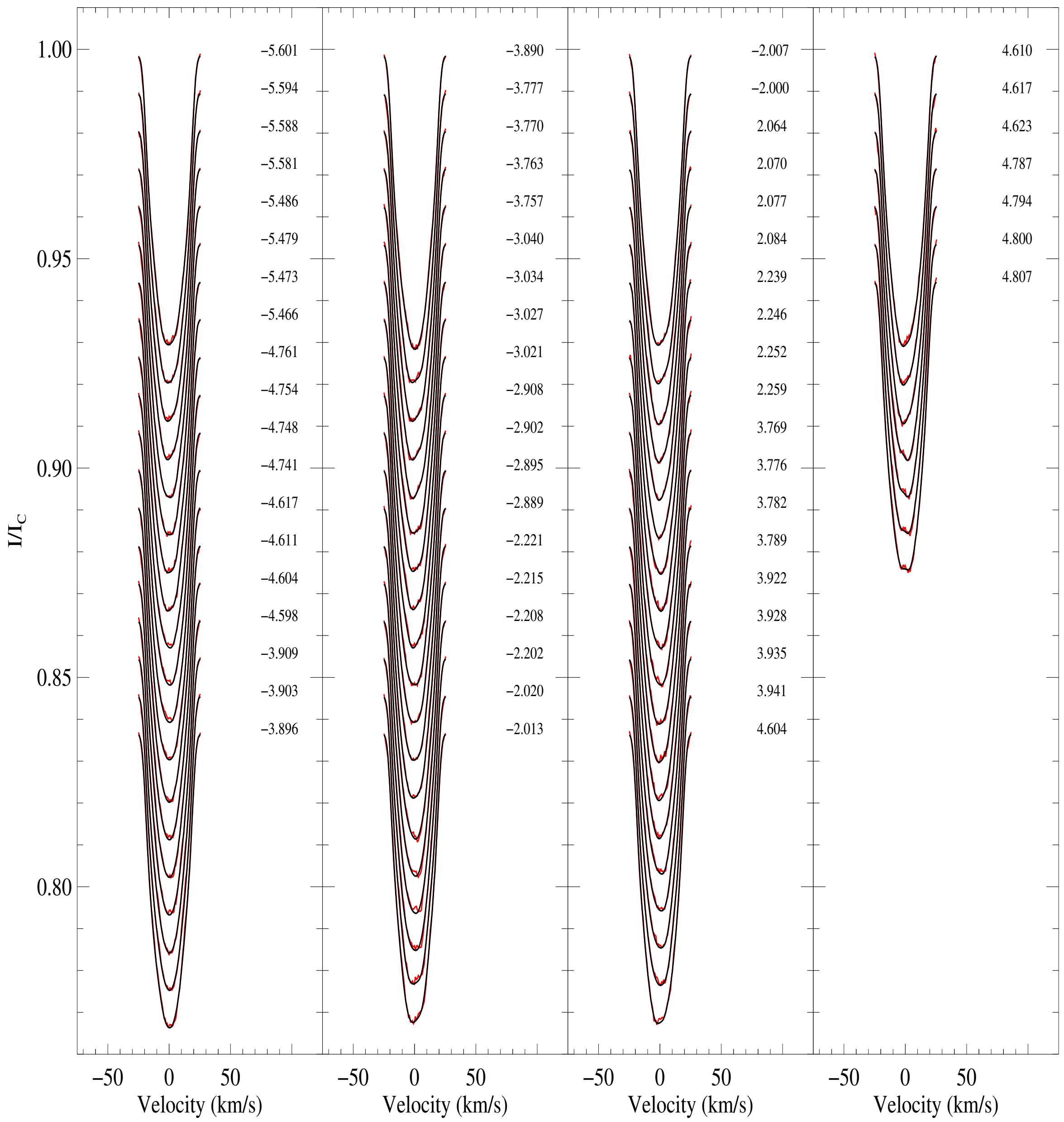

Figure A.2.2: Maximum entropy fits to the Stokes *I* LSD profiles for HD 43989 at the TBL telescope in January 2019 epoch 2019.06. The plot details are the same as in Figure A.1.1.

A.3 HIP 71933

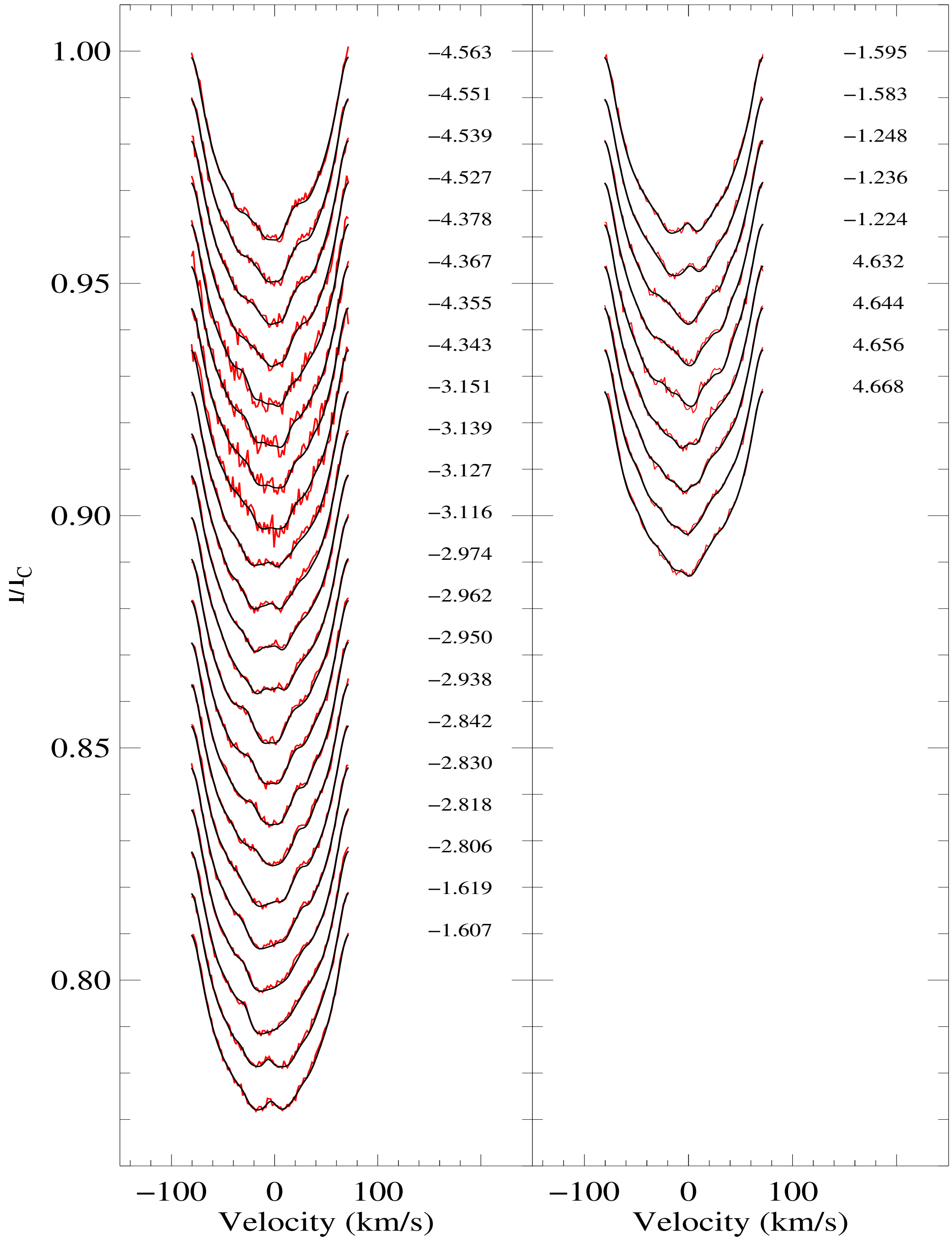

Figure A.3.1: Maximum entropy fits to the Stokes *I* LSD profiles for HIP 71933 at the AAT in April, 2009 epoch 2009.26. The plot details are the same as in Figure A.1.1. This figure is reproduced from Hughes et al. (2023).

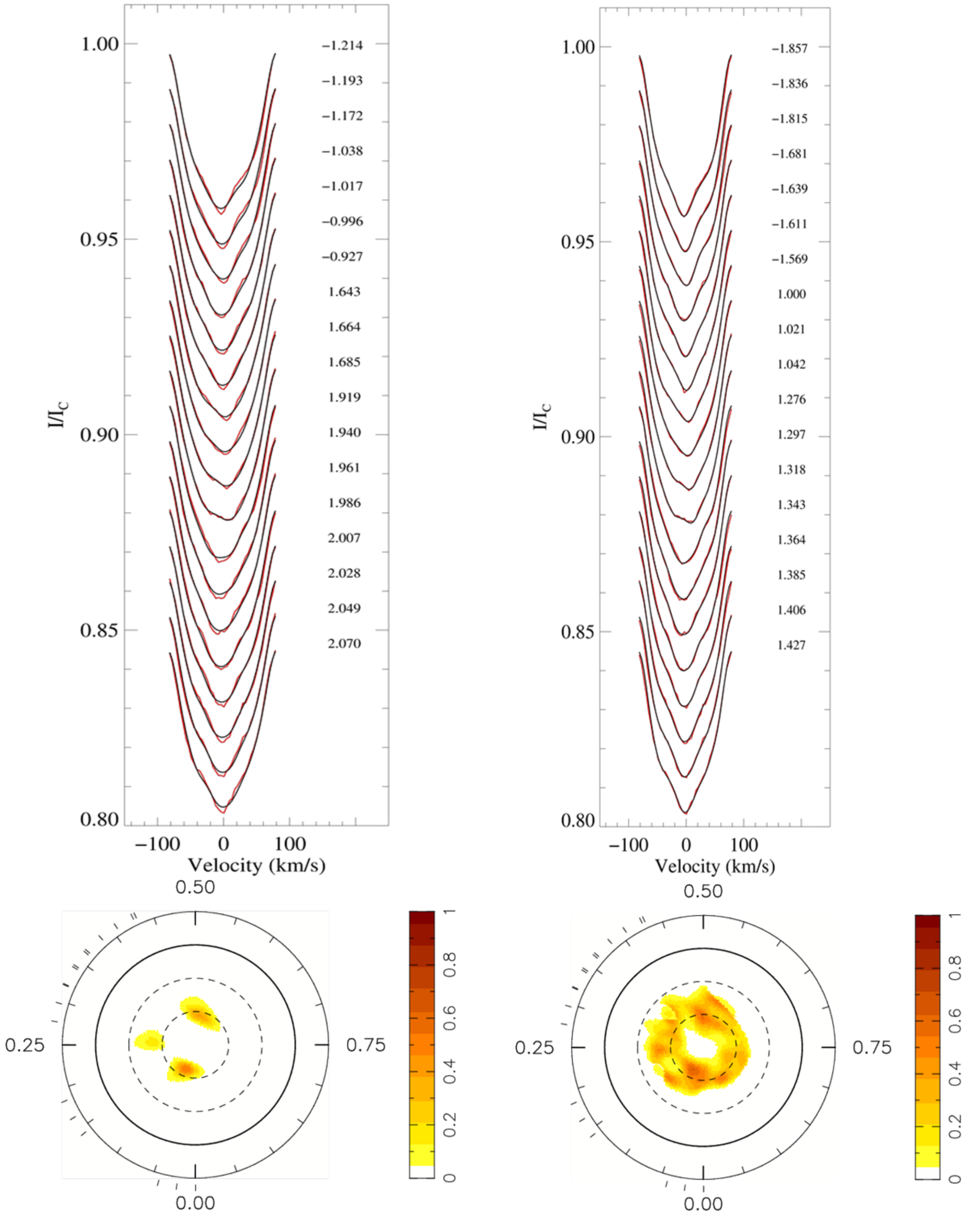

Figure A.3.2: Maximum entropy fits to the Stokes *I* LSD profiles for HIP 71933 at the 2.3-m telescope epoch 2009.34. The plot details are the same as in Figure A.1.1. The associated brightness maps are shown below the corresponding fits. The upper left image are the fits using a *v*sin*i* value of 76 km s^{-1}and shows small additional structure (dips) in the center of most of the profiles. The upper right image are the fits for a *v*sin*i* of 74 km s^{-1}, which provides a better fit. This fit results in a brightness map with additional spottedness above the +60° latitude, however there is still a lack of spots at the pole. See Section 5.3 for additional discussion. This figure is reproduced from Hughes et al. (2023).

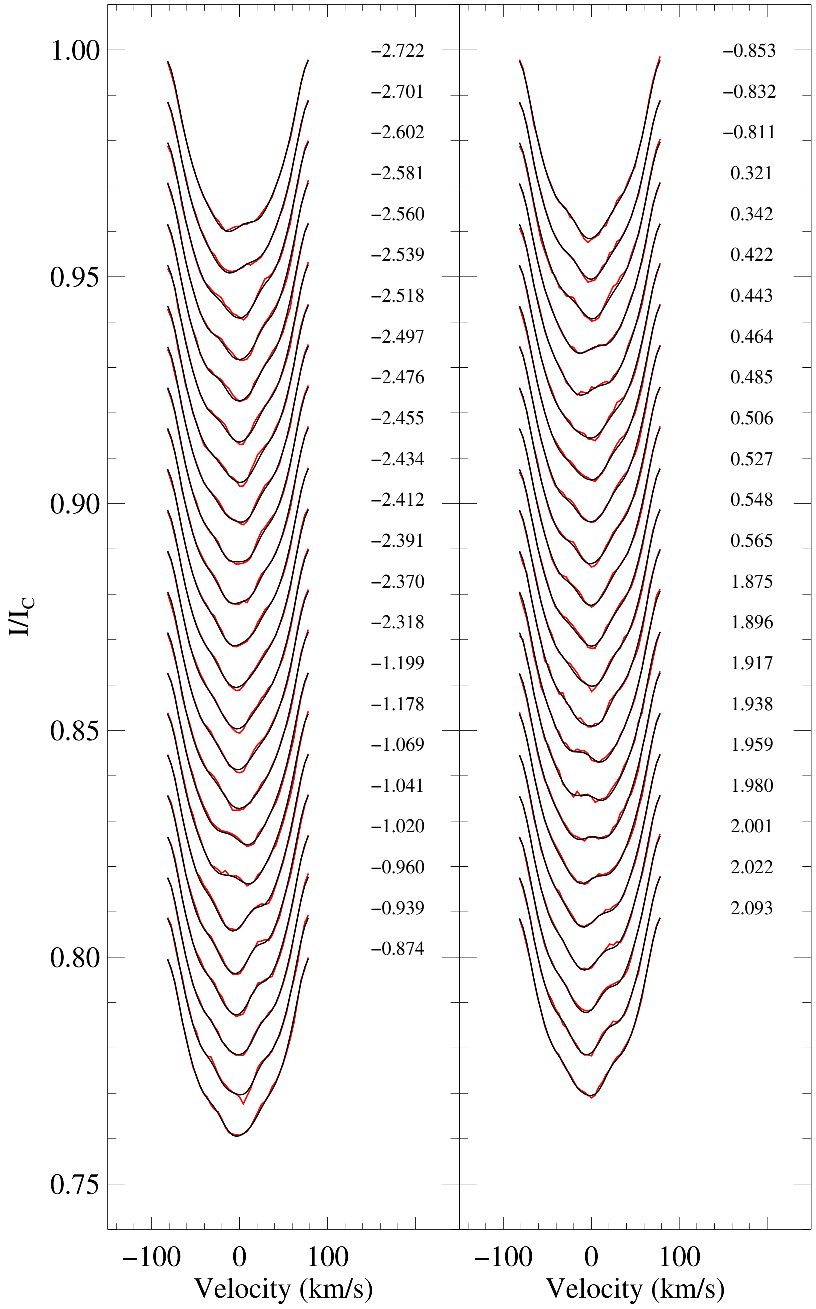

Figure A.3.3: Maximum entropy fits to the Stokes *I* LSD profiles for HIP 71933 at the 2.3-m telescope in April, 2010 epoch 2010.33. The plot details are the same as in Figure A.1.1. This figure is reproduced from Hughes et al. (2023).

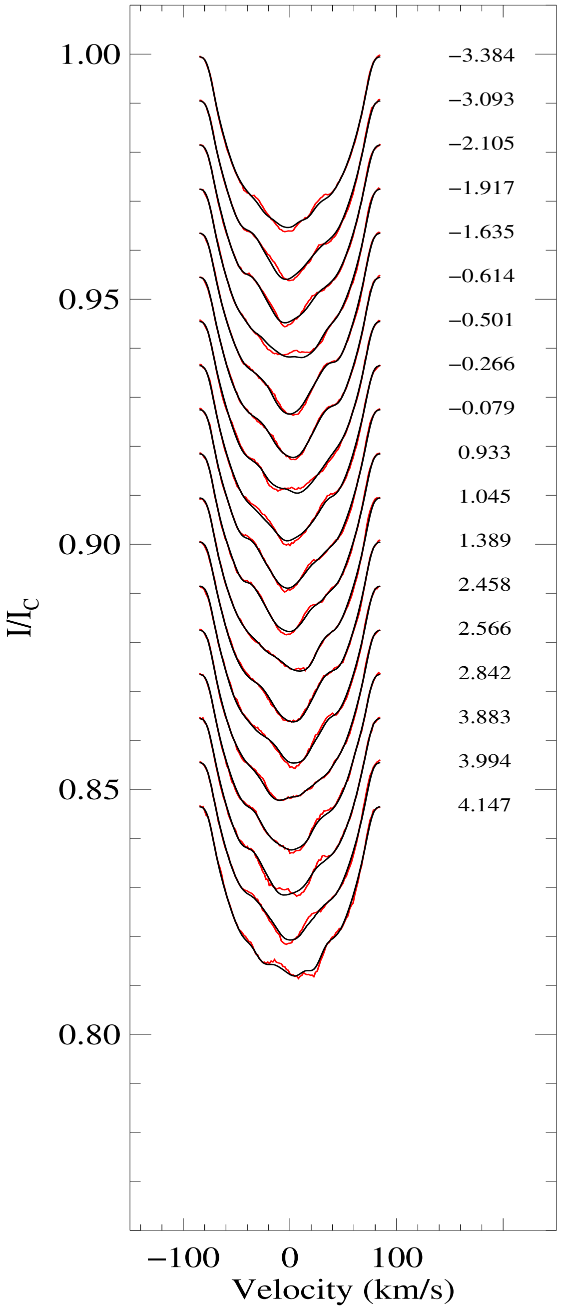

Figure A.3.4: Maximum entropy fits to the Stokes *I* LSD profiles for HIP 71933 at the 3.6-m telescope in May 2011, epoch 2011.37. The plot details are the same as in Figure A.1.1. This figure is reproduced from Hughes et al. (2023).

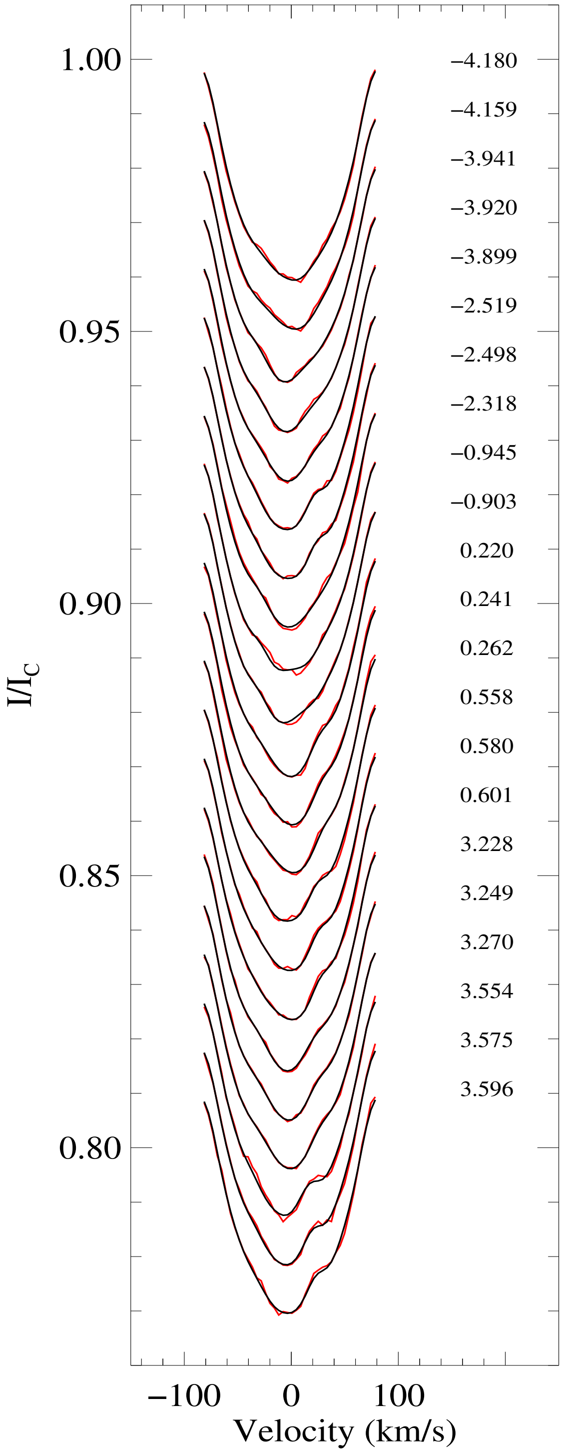

Figure A.3.5: Maximum entropy fits to the Stokes *I* LSD profiles for HIP 71933 at the 2.3-m telescope in April 2012, epoch 2012.26 The plot details are the same as in Figure A.1.1. This figure is reproduced from Hughes et al. (2023).

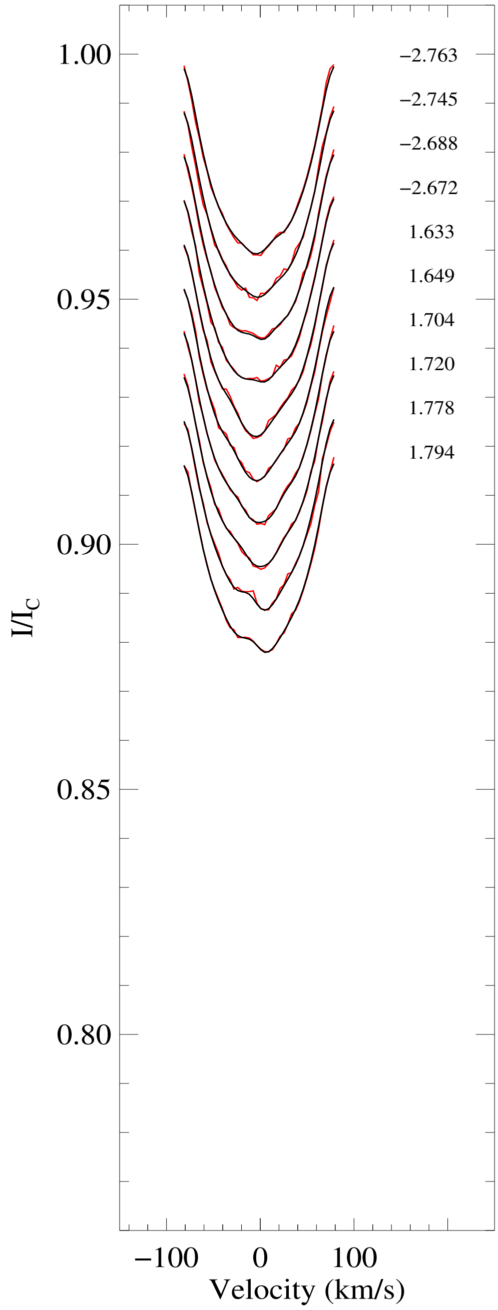

Figure A.3.6: Maximum entropy fits to the Stokes *I* LSD profiles for HIP 71933 at the 2.3-m telescope in January, 2018, epoch 2018.27 The plot details are the same as in Figure A.1.1. This figure is reproduced from Hughes et al. (2023).

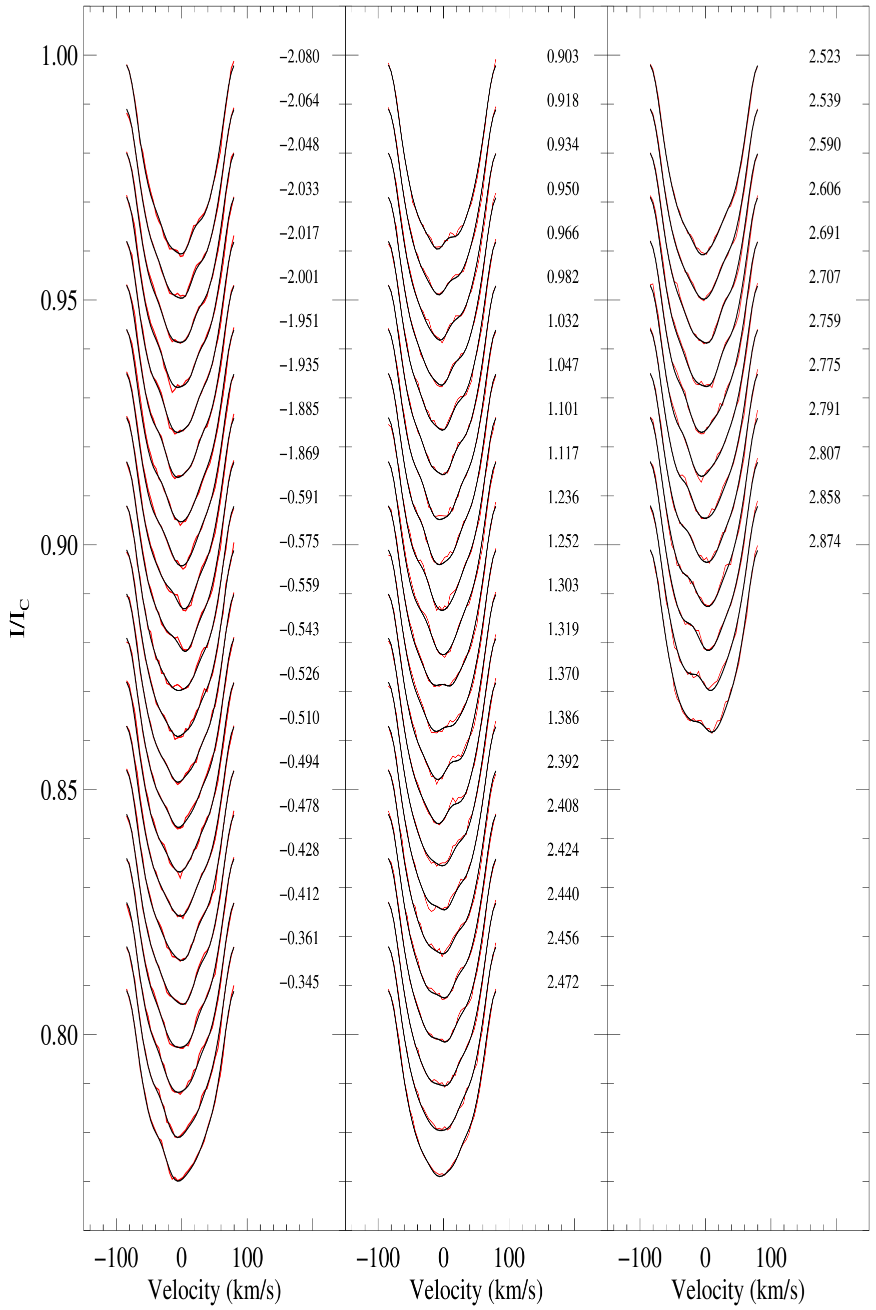

Figure A.3.7: Maximum entropy fits to the Stokes *I* LSD profiles for HIP 71933 at the 2.3-m telescope in June, 2019, epoch 2019.46 The plot details are the same as in Figure A.1.1. This figure is reproduced from Hughes et al. (2023).

B MAGNETIC FITS

Figure B.1.1 through B.2.1 are the Stokes *V* maximum entropy fits for the four epochs where Stokes *V* data was obtained from the spectropolarimeters at the AAT SEMPOL, the TBL and the LaSilla HARPSpol. Again, the red lines are the observed LSD profiles and the black lines are the fits calculated from the Zeeman Doppler Imaging code.

B.1 HD 43989

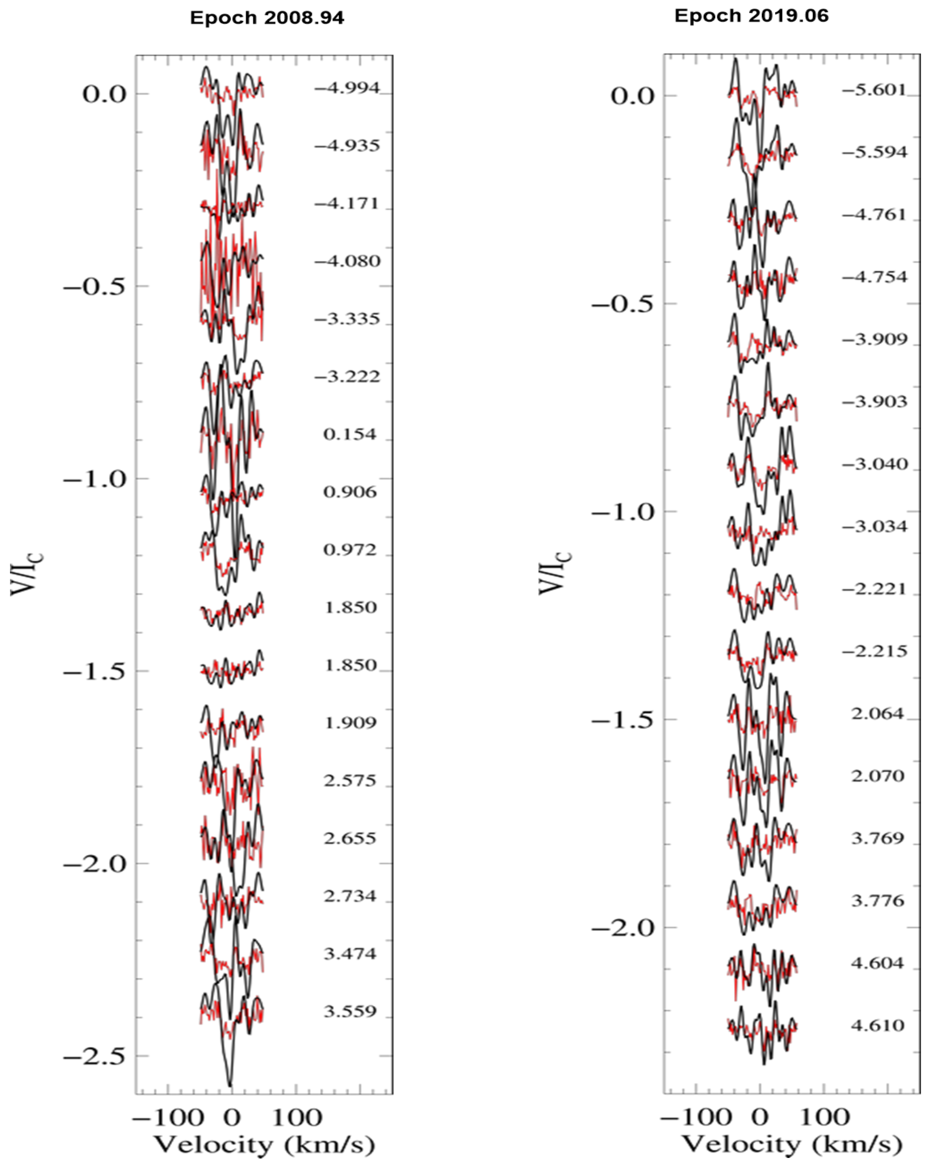

Figure B.1.1: Maximum entropy fits to the Stokes *V* LSD profiles for HD 43989 at the AAT and the TBL telescopes in December 2008 and the TBL in Jan 2019, epochs 2008.94 and 2019.06. The red lines are the observed data and the black lines are the calculated fits. Each profile is shifted down for graphical purposes. The rotational phases for each profile are shown on the right.

B.2 HIP 71933

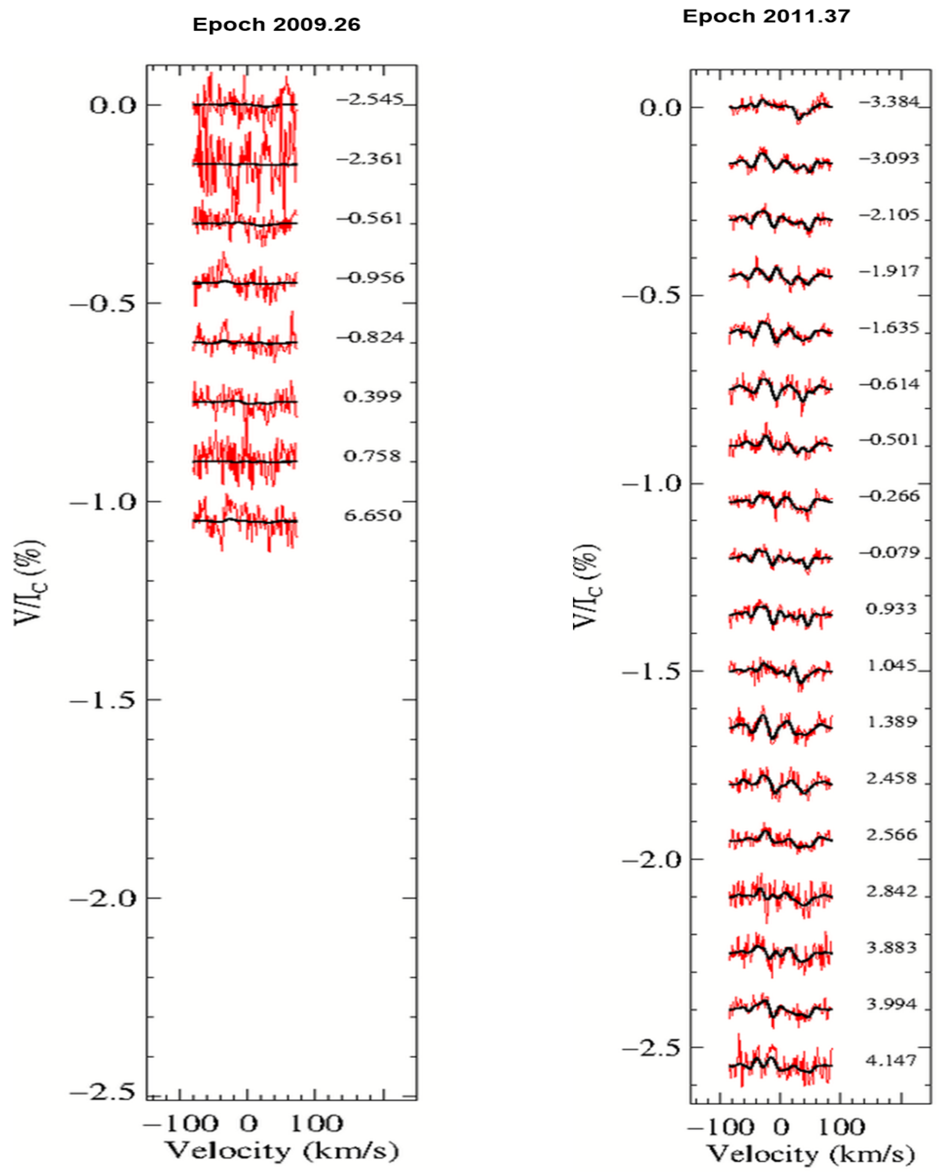

Figure B.2.1: Maximum entropy fits to the Stokes *V* LSD profiles for HIP 71933 at the AAT in April 2009, epoch 2009.26 and La Silla 3.6-m telescope in May 2011, epoch 2011.37. The plot details are the same as in Figure B.1.1. This figure is reproduced from Hughes et al. (2023).

C COMPUTATIONAL METHODS

C.1 DI-ZDI

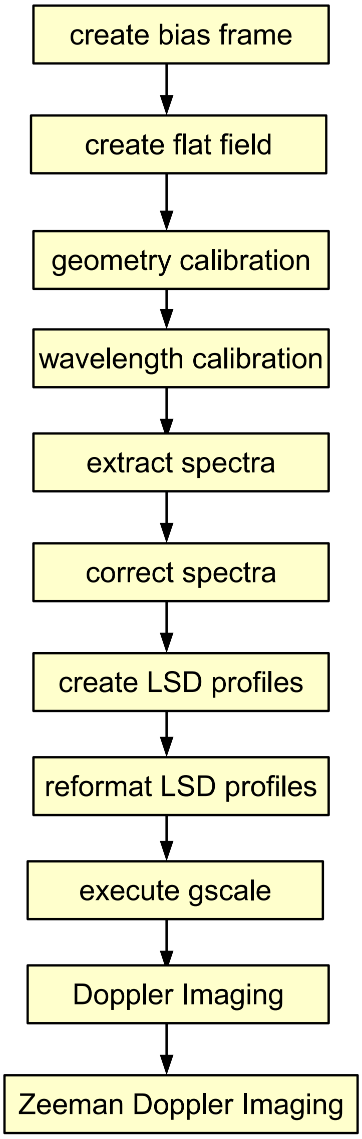

Figure C.1.1: Computational steps for the DI-ZDI process.

The computer programs used to perform the calculations described in Section 3 were obtained from the authors cited in that Section and installed and configured in onto a multi-core computer running Linux. The codes for the DI-ZDI process are executed in a pipleline which is shown in Figure C.1.1. The first seven steps in this pipeline from the creation of an average bias file up to the creation of the LSD profiles is executed through a package ESpRIT (Echelle Spectra Reduction and Interactive Tool) (Donati et al., 1997). The DI and

ZDI codes used to create the brightness and magnetic maps were created by Donati & Brown (1997). Each of these steps is described in the following sub-paragraphs.

Bias frame file Light from distant stars is extremely weak which means that any kind of astronomical detector must be calibrated to remove sources of noise. CCD detectors produce stray voltages during each exposure which are inherent in the detector itself. This particular type of noise is called *bias* which is signal offset from the detector.

During observational runs, time is taken to close the detector to any input light and expose several frames in sequence. These will be averaged together to be later subtracted from the reduced data. These bias frames are taken throughout the night as the telescope slews between selected targets. The group of bias frames that are taken closest to the observation of a particular target are averaged into a single bias frame. This program adjusts the frame to separate the orders correctly so that it can be later reduced.

Flat field file A flat frame is meant to record noise inherent in the optics of the telescope which is to be subtracted along with the bias files. Flat frames are usually recorded at dusk before an observing night and just before dawn, where the sky is uniformly illuminated and somewhat dim.

Geometry calibration The spectrum of a star is too large to fit across the detector in the spectrograph and to compensate, the spectral lines are cut into orders which are laid across the CCD in the detector. These orders are uneven and overlap. This code calculates the geometry of the spectrum as it is laid across the CCD in an X-Y format. As inputs, the program needs the location of the center of the first order, the separation between orders the number and increment of the orders and the direction of dispersion with increasing wavelength. A graphical representation of the fit to order curvature is produced from the estimated slit curvature and accuracy of the fit. This requires as input the bias average file, flat average file and an series of Thorium Argon (ThAr) exposures which place a ThAr spectrum onto the CCD. This is done by recording exposures made by a ThAr arc lamp. The code identifies the orders on the CCD and prints a list of the center points and separation. This process is repeated after adjusting the input values until the orders appear well centered in the output.

Wavelength calibration Throughout an observing run temperature and pressure changes can affect the geometry of the telescope and spectrograph, which leads to shifts of the wavelength values recorded by the detector. From the geometry process there is already a comparison spectrum from the ThAr exposures. Using these lines as a reference this program determines the wavelength location on the CCD which will later be used to adjust the recorded spectral line wavelengths closer to their true value. Along with the geometry calibration, this can also be a long labor-intensive process, involving estimates of the starting order increments, initial wavelengths and dispersion, all from a visual inspection of the ThAr exposures. A graph of residual line shift against the number of pixels is produced against an ideal dispersion to visually inspect for a proper fit and like the geometry calibration, is repeated after an examination of this graph, with new estimates.

Spectra extraction The spectral lines that are collected from each exposure are then refined by including the average bias file, the average flat file, the geometry information from the geometry calibration, and the wavelength information from the wavelength calibration. The process is finally completed by including the detector gain and the detector rejection threshold. These last two will be published values from the telescope instrumentation documentation.

These lines are "uncorrected" because it has not taken into account the movement of the Earth during the observation. For this reason the observation process includes recording the heliocentric velocity of the Earth towards the star and the Julian Date and UT time of the observation as well as the radial velocity of the Earth as shown by the telluric lines in the exposure. These values will be used in the next step to correct the spectra and are recorded for each exposure because they will change between exposures.

Spectra RV correction This step using the values discussed above uses a telluric line atlas to help identify which spectral lines are atmospheric. An LSD process as described in 3.1.2 is used to create an LSD profile of the telluric lines that are in the exposure. The spectral lines from each exposure are then corrected from this telluric LSD profile.

LSD profiles The corrected spectrum contains as many as 2,000 to 3,000 spectral lines. Each individual line has an SNR of approximately 30 to 50. The LSD process described in Section 3.1.2 is then applied to these lines to produce a single line profile with a much higher SNR. This profile (see Figure 3.1.3) is a curve of intensity plotted against velocity. Any distance from a zero velocity is interpreted as the radial velocity (RV) of the star relative to the Earth.

The previous step is the end of the codes in the EsPRIT package and results in the production of the LSD profiles (one for each exposure) used in the the DI and ZDI process to produce brightness and magnetic maps. These steps are discussed in detail in Mengel (2014a).

To begin with the DI and ZDI steps a set of stellar parameters is established from which the DI and ZDI codes will attempt to fit. These values are manually adjusted in a continuous fashion and the DI and ZDI iterations are re-executed until a best χ^2 fit of the LSD profiles is obtained. Each iteration includes a maximum-entropy calculation which provides a metric (*test* parameter) per the rules defined in (Skilling & Bryan, 1984). The goal is to select a set of values which will produce the lowest χ^2 value that does not exceed a maximum maximum entropy test value which represents the maximum entropy in the data. These stellar parameters are:

inclination (i): the "tilt" of the star as seen by the observer,

$v\sin i$: the rotational velocity of the star "reduced" by the sin of the inclination as seen by the observer,

rotational period (P_{rot}): the rotational period of the star in days,

photospheric temperature (T_{phot}): the temperature of the photosphere, sot temperature (T_{spot}): the temperature of a spot on the photosphere.

The DI and ZDI calculations are more sensitive to the first three parameters and temperature values obtained from the GAIA satellite are used with little or no variation.

Reformat the LSD Profiles This is the first step of preparing the LSD profiles to submit to the DI code.

Rotational Phase The rotational phase of star is given by:

$$\phi_{obs} = \frac{JD_{obs} - t_0}{P_{rot}} \tag{C.1.1}$$

where JD_{obs} is the julian date of the observation, t_0 is the selected starting time and P_{rot} is the rotational period of the star. This value is necessary for the DI codes to map the brightness features at the correct longitude. The starting point t_0 (or *zero point*) is calculated to be the midpoint of the first observation in an epoch. The zero point for all subsequent epochs is calculated as a integer number of rotations starting with the zero-point of the first epoch that is the closest to the mid-point of each epoch. The rotational phase for each observing epoch was for this thesis calculated by hand and entered as an input parameter into the reformat codes.

The reformat code is the first set of codes in the (Donati & Brown, 1997) package and produces a single input file from all of the lsd profiles to use as an input for the subsequent gscale calculation. This requires the rotational phase, the SNR of the lsd profiles, which was computed during the lsd profile creation, and the resolution of the spectrograph.

Gscale The gscale code uses the single input file created during the reformat step and normalizes the continuum and the equivalent width of the LSD profiles.

DI and ZDI From here the DI and ZDI processes as described in sections 3.2.1 and 3.2.2 are exected using multiple χ^2 iterations to create the brightness and magnetic maps against the mathematical models. The stellar parameters are adjusted manually until the best χ^2 value with the highest entropy can be achieved. These steps are described in more detail in (Mengel, 2014b).

As would be expected, each calculation defined in Figure C.1.1 is best executed using scripts with an input file containing the parameters described above. For the purpose of this thesis I elected to formalize these scripts into a series of PERL scripts which allowed for the selection of stellar parameters from a group of files and controls execution of the codes within the ESpRIT, DI and ZDI programs. A description of these scripts as well as sample files and outputs in shown in Appendix C.3.

C.2 Differential Rotation

DR calculations as described in Section 5.2 produce a two dimensional grid of rotation rate Ω_{eq} vs rotational shear $d\Omega$. The grid nature of the calculations as well as the fact that they are time consuming make them well suited for parallelization. The multi-core linux computer used for this study was set up to calculate a set of shear values from the stellar equator to the pole for small increments of rotation. These calculations were executed in parallel in separate directories, and the resultant output files were then "stitched" together to form a single output file. As with the DI-ZDI calculations, a set of PERL scripts was developed to split up the codes into separate shear "slices" which were edited to define the slices and were then executed simultaneously. The output map files were then "stitched together".

C.3 PERL Scripts

The computer codes that make up the ESpRIT, DI, ZDI and DR packages can all be executed separately, with the required parameters entered manually via the computer keyboard when prompted. For obvious reasons, this becomes tedious and error prone, give the large number of executions needed to produce the final outputs. Each code is suited for execution with an input data file with the necessary parameters and execution options ("yes" or "no" for various execution paths, etc). This process alone can result in a large amount of typing to complete execution of the pipline described in Sections C.1 and C.2.

To solve this problem I elected to create somewhat more formalized PERL scripts in order to organize the execution of the codes. In these scripts input files are constructed for each program, themselves created from manual data files which allows for the execution of the entire pipeline, or some steps in the pipeline with a specific set of stellar and other data parameters. All of the scripts and codes for the different epochs for each star were encapsulated within separate accounts on a computer with a multi-core CPU running Linux Ubuntu 14.04 (later upgraded to Mint 21). Each PERL script organizes the execution of the astronomy codes by constructing the input files from manual data files and storing the output of the program in separate output files. These files are saved for later analysis for the process of troubleshooting the execution of the codes. The PERL scripts varied for each observing epoch because of the differences in the reduction methods at each telescope. For example, the raw data received from the HARPSpol at La Silla observatory and the TBL telescope were corrected extracted spectra, with the preliminary calibration steps performed by the observing astronomer using procedures unique to those telescopes. Raw data from the 2.3-m telescope at the Siding Spring Observatory required modification to be consistent with the EsPRIT codes.

At the top of this set of PERL scripts is a control script which allows the user to select which sets of computer codes will be executed. Options presented to the user by this script allow for the execution of PERL modules which themselves execute the astronomy codes, which are written in languages including Unix C-shells, FORTRAN and C++. From these modules, the input files needed by the various programs are constructed and the output files saved. Section C.3.1 is the top level DI-ZDI PERL script which allows selection of the other astronomy codes individually. There are also options to execute some of the codes in order, and finally an option to run all of the codes from the raw FITS files to the final creation of the brightness and magnetic maps and output data files. Section C.3.2 provides the same for the script which controls execution of the DR codes. Following each script listing is the output.

C.3.1 Top DI-ZDI script

```
#
######################################################################
#
# main.pl
#
# script to execute DI ZDI astronomy codes
#
####################################################################
#
#
use Switch;
use Astro::FITS::CFITSIO;
use File::Find;
use Data::Dumper;
use Storable;
#
use lib "modules";     # this is the path to the modules from the
    current directory
#
use modules::GlobalVariables;
use modules::CreateFITSHash;
use modules::PrintByDate;
use modules::CreateSubhashes;
use modules::CreateBiasAverages;
use modules::CreateFlatAverages;
use modules::IdentifyTHARFile;
use modules::CreateGeometryData;
use modules::WavelengthCalibration;
use modules::CreateUncorrectedSpectrum;
use modules::CorrectSpectrum;
use modules::ProduceStokesI;
use modules::ZDICamStellarParameters;
use modules::ZDICamReformat;
use modules::ZDICamGscale;
use modules::ZDICam;
use modules::ZDICamDisplay;
use modules::ZDICamGdata;
use modules::ZDIpy_renormalize_LSD;
use modules::Createinzdi;
use modules::PrintOutParameters;
use modules::Prepzdipy;
use modules::ZDIpy;
#
use modules::CreateUncorrectedSpectrumStokesV;
use modules::CorrectSpectrumStokesV;
use modules::ProduceStokesV;
use modules::ReformatStokesV;
use modules::ZDIPot;
use modules::ZDIPotDisplay;
use modules::CreateGeometryDataStokesV;
```

```
use modules::GlobalVariables;
use modules::CreateUncorrectedSpectrumStokesV;
use modules::CorrectSpectrumStokesV;
use modules::ProduceStokesV;
use modules::ReformatStokesV;
use modules::ZDIPot;
use modules::ZDIPotDisplay;
use modules::CreateGeometryDataStokesV;
#
#
##############################
# put up the main menu
##############################
#
$target = "HIP71933";
$dataset_origin = "AAT";
#
$observation_month = "AAT_Apr09";
#
print "\n\n";
print "\n\n", "Display graphics?  (y/n) \n";
chomp ($display_graphics = <STDIN>);
#
# clear the screen
#
#system("clear");
#
print "The target is:  $target\n";
print "The dataset is from $dataset_origin\n";
#
print "\n\n\n";
print " (1)  create_FITS_hash \n";
print " (2)  print by date \n";
print " (3)  create subhashes \n";
print " (4)  create bias averages \n";
print " (5)  create flat averages \n";
print " (6)  identify thar file to use \n";
print " (7)  create geometry data \n";
print " (8)  perform wavelength calibration \n";
print " (9) create uncorrected spectrum  \n";
print " (10) correct the spectrum \n";
print " (11) produce the Stokes I profile \n";
print " (12) produce ZDIcam prep data  (para 2)\n";
print " (13) ZDIcam reformat  (para 4)\n";
print " (14) ZDIcam gscale (para 5)\n";
print " (15) ZDIcam (para 6)\n";
print " (16) ZDIcam display (para 7)\n";
print " (17) ZDIcam gdata (para 7.2)\n";
#
print " (18)  Do 13, 14, 15, 16, 17, 18 (reformat, gscale, zdicam, gdata)
      \n";
#
print "\n\n";
print " (19)  do 1 - 18 (DI only) \n";
#
print " (20) print out parameters \n";
```

```
#
print " (21) do everything (DI and ZDI) \n";
#
print "\n\n\n";
#
chomp($num = <STDIN>);
#
switch($num) {
        #
        case "1" {CreateFITSHash::create_FITS_hash($target,
           $display_graphics, $dataset_origin, $observation_month);}
        case "2" {PrintByDate::print_by_date($target, display_graphics,
           $dataset_origin);}
        case "3" {CreateSubhashes::create_subhashes($target,
           display_graphics, $dataset_origin);}
        case "4" {CreateBiasAverages::create_bias_averages($target,
           $display_graphics, $dataset_origin);}
        case "5" {CreateFlatAverages::create_flat_averages($target,
           $display_graphics, $dataset_origin);}
        case "6" {IdentifyTHARFile::identify_thar_file($target,
           $display_graphics, $dataset_origin);}
        case "7" {CreateGeometryData::create_geometry_data($target,
           $display_graphics, $dataset_origin);}
        case "8" {WavelengthCalibration::perform_wavelength_calibration(
           $target, $display_graphics, $dataset_origin);}
        case "9" {CreateUncorrectedSpectrum::create_uncorrected_spectrum(
           $target, $display_graphics, $dataset_origin);}
        case "10" {CorrectSpectrum::correct_spectrum($target,
           $display_graphics, $dataset_origin);}
        case "11" {ProduceStokesI::produce_stokes_I_profile($target,
           $display_graphics, $dataset_origin);}
        case "12" {ZDICamStellarParameters::zdicam_stellar_parameters(
           $target, $display_graphics, $dataset_origin); }
        case "13" {ZDICamReformat::zdicam_reformat($target,
           $display_graphics, $dataset_origin); }
        case "14" {ZDICamGscale::zdicam_gscale($target, $display_graphics
           , $dataset_origin); }
        case "15" {ZDICam::zdicam($target, $display_graphics,
           $dataset_origin); }
        case "16" {ZDICamDisplay::display($target, $display_graphics,
           $dataset_origin); }
        case "17" {ZDICamGdata::gdata($target, $display_graphics,
           $dataset_origin); }
        case "18" {
                print "\nstart:   ", ‘date‘, "\n";;
                #
                ZDICamStellarParameters::zdicam_stellar_parameters(
                    $target, $display_graphics);
                ZDICamReformat::zdicam_reformat($target,
                    $display_graphics);
                ZDICamGscale::zdicam_gscale($target, $display_graphics);
                ZDICam::zdicam($target, $display_graphics);
                ZDICamDisplay::display($target, $display_graphics);
                ZDICamGdata::gdata($target, $display_graphics);
                PrintOutParameters::printoutparameters($target,
                    $display_graphics);
```

```
        #
        print "\n end: ",  ‘date‘, "\n";
        }


case "19" {
        print "\nstart:  ", ‘date‘, "\n";;
        #
        CreateFITSHash::create_FITS_hash($target,
            $display_graphics, $dataset_origin,
            $observation_month);
        CreateSubhashes::create_subhashes($target,
            $display_graphics, $dataset_origin);
        CreateBiasAverages::create_bias_averages($target,
            $display_graphics, $dataset_origin);
        CreateFlatAverages::create_flat_averages($target,
            $display_graphics, $dataset_origin);
        IdentifyTHARFile::identify_thar_file($target,
            $display_graphics, $dataset_origin);
        CreateGeometryData::create_geometry_data($target,
            $display_graphics, $dataset_origin);
        WavelengthCalibration::perform_wavelength_calibration(
            $target, $display_graphics, $dataset_origin);
        CreateUncorrectedSpectrum::create_uncorrected_spectrum(
            $target, $display_graphics, $dataset_origin);
        CorrectSpectrum::correct_spectrum($target,
            $display_graphics, $dataset_origin);
        #
        ProduceStokesI::produce_stokes_I_profile($target,
            $display_graphics, $dataset_origin);
        ZDICamStellarParameters::zdicam_stellar_parameters(
            $target, $display_graphics, $dataset_origin);
        ZDICamReformat::zdicam_reformat($target,
            $display_graphics, $dataset_origin);
        ZDICamGscale::zdicam_gscale($target, $display_graphics,
            $dataset_origin);
        ZDICam::zdicam($target, $display_graphics,
            $dataset_origin);
        ZDICamDisplay::display($target, $display_graphics,
            $dataset_origin);
        ZDICamGdata::gdata($target, $display_graphics,
            $dataset_origin);
        PrintOutParameters::printoutparameters($target,
            $display_graphics, $dataset_origin);
        #
        print "\n end: ",  ‘date‘, "\n";
        }
#
case "20" {PrintOutParameters::printoutparameters($target,
    $display_graphics, $dataset_origin); }
#
case "21" {
        print "\nstart everything:  ", ‘date‘, "\n";;
        #
        CreateFITSHash::create_FITS_hash($target,
            $display_graphics, $dataset_origin,
```

```
            $observation_month);
        CreateSubhashes::create_subhashes($target,
            $display_graphics, $dataset_origin);
        CreateBiasAverages::create_bias_averages($target,
            $display_graphics, $dataset_origin);
        CreateFlatAverages::create_flat_averages($target,
            $display_graphics, $dataset_origin);
        IdentifyTHARFile::identify_thar_file($target,
            $display_graphics, $dataset_origin);
        CreateGeometryData::create_geometry_data($target,
            $display_graphics, $dataset_origin);
        WavelengthCalibration::perform_wavelength_calibration(
            $target, $display_graphics, $dataset_origin);
        CreateUncorrectedSpectrum::create_uncorrected_spectrum(
            $target, $display_graphics, $dataset_origin);
        CorrectSpectrum::correct_spectrum($target,
            $display_graphics, $dataset_origin);

        ProduceStokesI::produce_stokes_I_profile($target,
            $display_graphics, $dataset_origin);
        ZDICamStellarParameters::zdicam_stellar_parameters(
            $target, $display_graphics, $dataset_origin);
        ZDICamReformat::zdicam_reformat($target,
            $display_graphics, $dataset_origin);
        ZDICamGscale::zdicam_gscale($target, $display_graphics,
            $dataset_origin);
        ZDICam::zdicam($target, $display_graphics,
            $dataset_origin);
        ZDICamDisplay::display($target, $display_graphics,
            $dataset_origin);
        ZDICamGdata::gdata($target, $display_graphics,
            $dataset_origin);
        PrintOutParameters::printoutparameters($target,
            $display_graphics, $dataset_origin);
        #
        CreateGeometryDataStokesV::create_geometry_data_stokes_V
            ($target, $display_graphics, $dataset_origin);
        CreateUncorrectedSpectrumStokesV::
            create_uncorrected_spectrum_stokes_V($target,
            $display_graphics, $dataset_origin);
        CorrectSpectrumStokesV::correct_spectrum_stokes_V(
            $target, $display_graphics, $dataset_origin);
        ProduceStokesV::produce_stokes_V_profile($target,
            $display_graphics, $dataset_origin);
        ReformatStokesV::reformat_stokes_V($target,
            $display_graphics,  $dataset_origin);
        ZDIPot::zdipot($target, $display_graphics,
            $dataset_origin);
        ZDIPotDisplay::display($target, $display_graphics,
            $dataset_origin);
        #
        print "\n\n end ", ‘date‘, "\n\n";
        #
        }
}
```

Top DI-ZDI script output

```
Display graphics? (y/n)
n
The target is: HIP71933
The dataset is from AAT



 (1)  create_FITS_hash
 (2)  print by date
 (3)  create subhashes
 (4)  create bias averages
 (5)  create flat averages
 (6)  identify thar file to use
 (7)  create geometry data
 (8)  perform wavelength calibration
 (9) create uncorrected spectrum
 (10) correct the spectrum
 (11) produce the Stokes I profile
 (12) produce ZDIcam prep data  (para 2)
 (13) ZDIcam reformat  (para 4)
 (14) ZDIcam gscale (para 5)
 (15) ZDIcam (para 6)
 (16) ZDIcam display (para 7)
 (17) ZDIcam gdata (para 7.2)
 (18)  Do 13, 14, 15, 16, 17, 18 (reformat, gscale, zdicam, gdata)


 (19)  do 1 - 18 (DI only)
 (20) print out parameters
 (21) do everything (DI and ZDI)
```

C.3.2 Top diffrot script

```
#
###############################################################
#
# diffrot.pl
#
#
#############################################################
#
#
use Switch;
use Astro::FITS::CFITSIO;
use File::Find;
use Data::Dumper;
use Storable;
#
use lib "modules";      # this is the path to the modules from the
   current directory
#
use modules::CalculateBetaGamma;
use modules::ExecuteDiffRot;
use modules::ClearDiffRotFiles;
use modules::PopulateDiffRotScripts;
use modules::KillDiffRotProcesses;
use modules::CheckForDiffRotMapFiles;
use modules::EditDiffRotScripts;
use modules::StitchDiffRotMapFiles;

#
##############################
# put up the main menu
##############################
#
print "\n\n",   "Enter target:  ";
chomp($target = <STDIN>);
#
#print "\n\n", "Enter value for omega from fitmap: ";
#chomp ($omega = <STDIN>);
#
#print "\n\n, Enter value for domega from fitmap: ";
#chomp($domega = <STDIN>);
#
# clear the screen
#
#system("clear");
#
print "The target is:  $target\n";
#
print "\n\n\n";
print " (1)  clear out existing diffrot files \n";
print " (2)  populate initial scripts  \n";
```

```
print " (3)  edit diffrot scripts \n";
print " (4)  execute  parallized differential rotation  \n";
print " (5)  kill parallelized diffrot processes  \n";
print " (6)  check for finished map files \n";
print " (7)  stitch together differential rotation maps  \n";
print " (8)  calculate beta and gamma values \n";


print "\n\n\n";
#
chomp($num = <STDIN>);
#
switch($num) {
        #
        case "1" {ClearDiffRotFiles::clear_files($target)}
        case "2" {PopulateDiffRotScripts::populate_scripts($target)}
        case "3" {EditDiffRotScripts::edit_diffrot_scripts($target)}
        case "4" {ExecuteDiffRot::execute_diffrot($target)}
        case "5" {KillDiffRotProcesses::kill_diffrot_processes($target)}
        case "6" {CheckForDiffRotMapFiles::check_for_diffrot_map_files(
            $target)}
        case "7" {StitchDiffRotMapFiles::stitch_diffrot_map_files($target
            )}
        case "8" {CalculateBetaGamma::calculate_beta_gamma($target)}
        #
        else {}
        }
```

Top diffrot script output

```
Enter target:  HIP71933
The target is:  HIP71933



 (1)  clear out existing diffrot files
 (2)  populate initial scripts
 (3)  edit diffrot scripts
 (4)  execute  parallized differential rotation
 (5)  kill parallelized diffrot processes
 (6)  check for finished map files
 (7)  stitch together differential rotation maps
 (8)  calculate beta and gamma values
```

D BRIGHTNESS AND MAGNETIC MAPS FROM PHOTOMETRIC ROTATION RATES

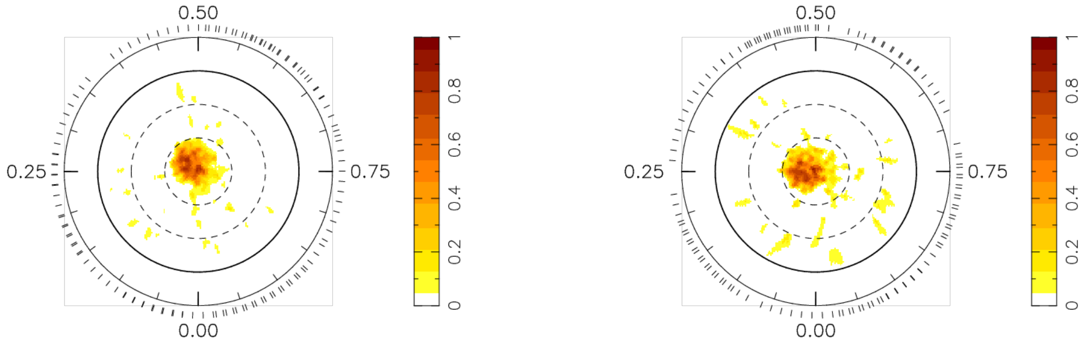

(a) VXR77A 2005.09 best rotation period (b) VXR77A 2005.09 TESS rotation period

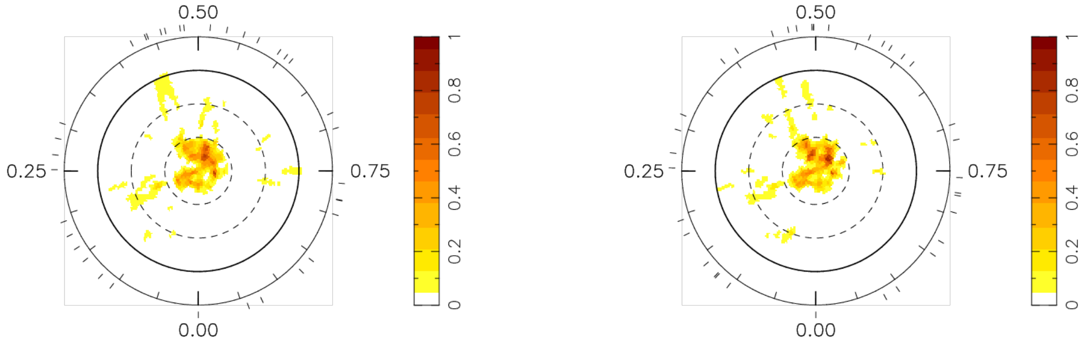

(c) VXR 77A Epoch 2018.07 best rotation period (d) VXR 77A Epoch 2018.07 TESS rotation period

Figure D.0.1: VXR77A brightness maps for Epoch 2005.09 and 2018.07, original best fit rotation period side by side with the rotation period derived from the TESS photometric observations. The maps on the left are duplicates of maps in Figure 4.2.3 and remain the best statistical fit. The maps on the right are a poorer statistical fit but within the limits described in (Skilling & Bryan, 1984)

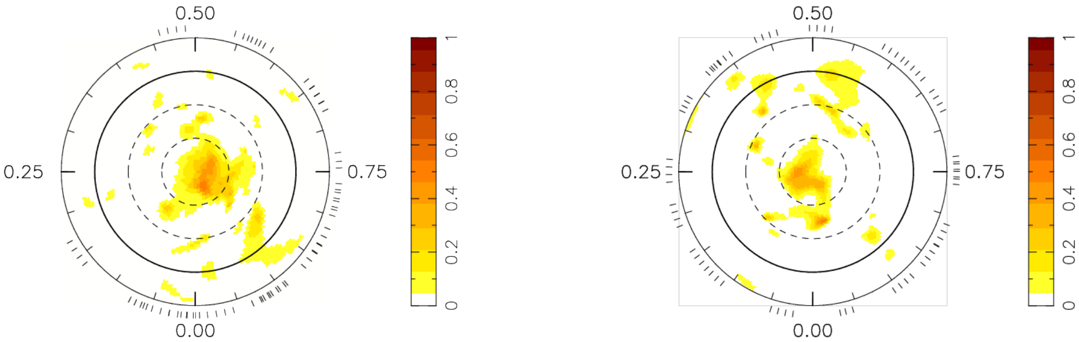

(a) HD 43989 Epoch 2008.94 best rotation period (b) HD 43989 Epoch 2008.94 TESS rotation period

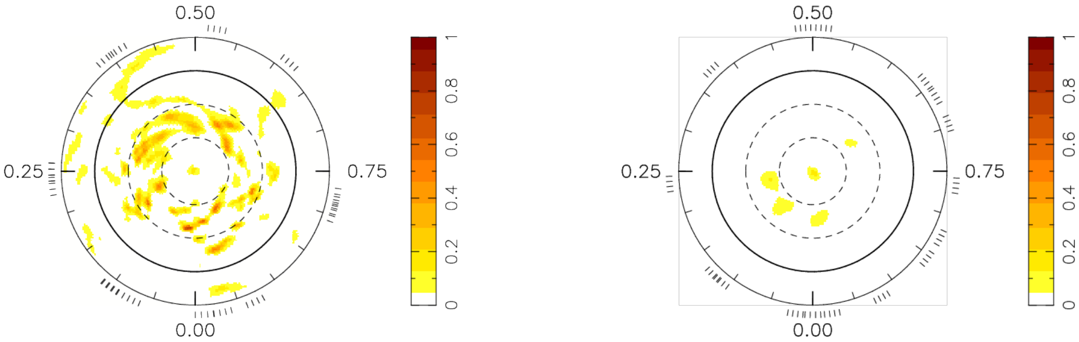

(c) HD 43989 Epoch 2019.06 best rotation period (d) HD 43989 Epoch 2019.06 TESS rotation period

Figure D.0.2: HD 43989 brightness maps for Epochs 2008.94 and 2019.06, original best fit rotation period side by side with the rotation period derived from the TESS photometric observations. The maps on the left are duplicates of maps in Figure 4.3.3 and remain the best statistical fits for both epochs. The rotation period of 1.167 d is a value that resulted in an acceptable fit for both the AAT and TBL data so was reported in Table 4.3.2. It is interesting to note that tthe TESS rotation rate (1.360 d) closely matches the rotation value of 1.357 d reported by (Hackman et al., 2016). In order to fit the TESS rotation rate to the AAT data, the χ^2 was raised (see Figure D.0.2b). See the discussion concerning this discrepancy in Section 4.3.2.

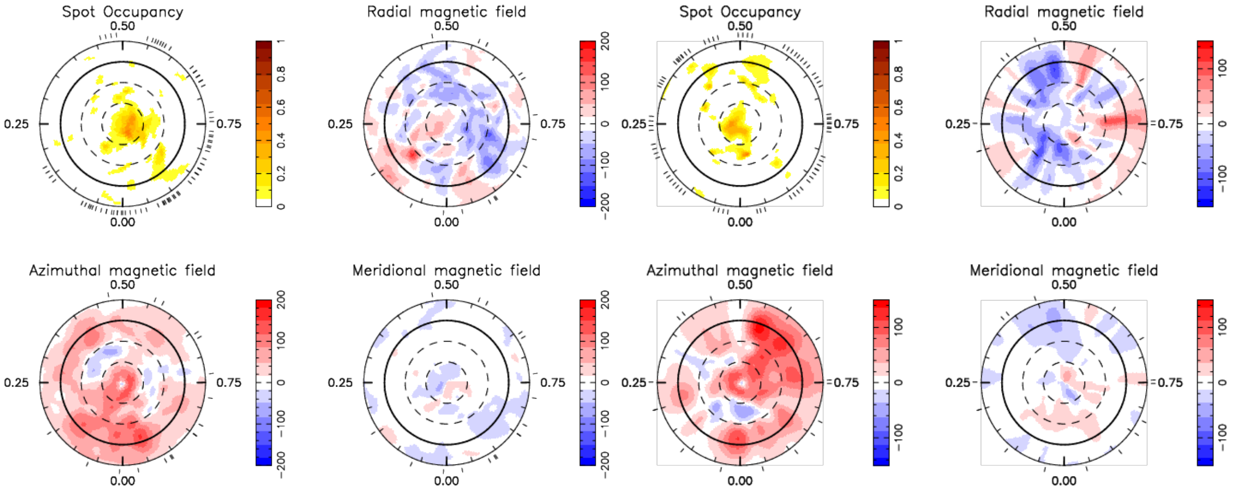

(a) HD 43989 Epoch 2008.94 best rotation period (b) HD 43989 Epoch 2008.94 TESS rotation period

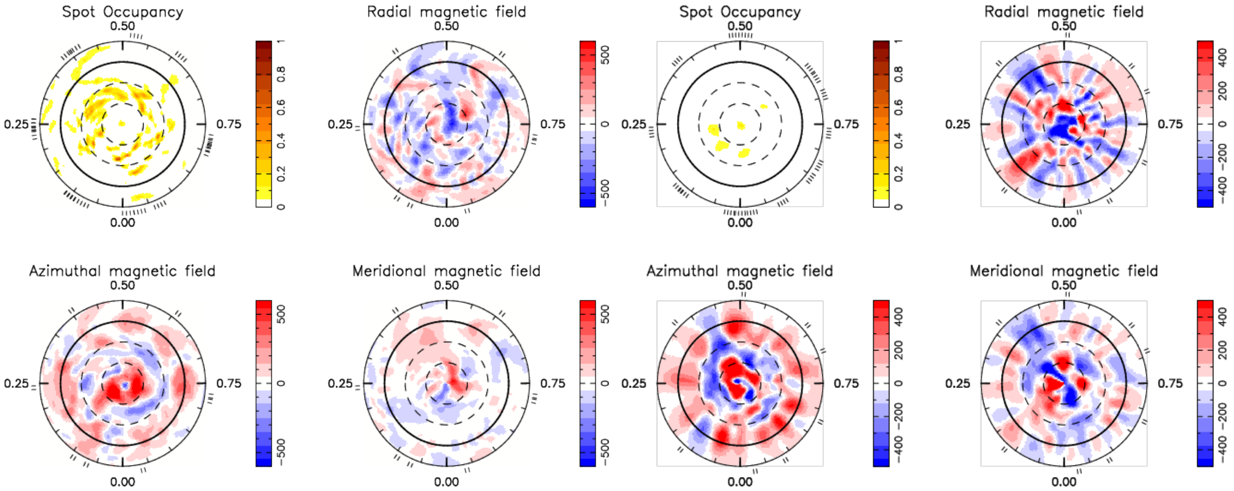

(c) HD 43989 Epoch 2019.06 best rotation period (d) HD 43989 Epoch 2019.06 TESS rotation period

Figure D.0.3: HD 43989 magnetic maps for Epochs 2008.94 and 2019.06, original best fit rotation period side by side with the rotation period derived from the TESS photometric observations. The maps on the left are duplicates of maps in Figures 4.3.4 and 4.3.5 and remain the best statistical fits for both epochs. In order to fit the TESS rotational value to the AAT data in Epoch 2008.94 the χ^2 value had to be raised.

Table D.0.1: Magnetic quantities for HD 43989 derived from maps in Figure 4.3.4 and Figure 4.3.5 placed next to values derived from the TESS rotation rates used to make Figure D.0.3. This table is modified from Table 4.3.3. Magnetic quantities for Epoch 2019.06 using the TESS rotation rate are shown in column 5 (the last column). While these values differ, they still show similar ratios between toroidal and poloidal energies and still support the possibility that a magnetic field reversal was occurring between viewing epochs. Variations for the TESS rotation were not calculated.

Quantity	Epoch 2008.94 original rotation (percent energy)	Epoch 2008.94 TESS rotation (percent energy)	Epoch 2019.06 original rotation (percent energy)	Epoch 2019.06 TESS rotation (percent energy)
Total poloidal	43^{+2}_{-5}	49	51^{+7}_{-11}	53
Total toroidal	57^{+6}_{-1}	51	49^{+11}_{-0}	47
poloidal (*l*=1)	13^{+0}_{-2}	20	4^{+0}_{-1}	2
poloidal (*l*=2)	$7^{+0}_{-1.5}$	5	2^{+0}_{-1}	1
poloidal (*l*=3)	2^{+0}_{-1}	3	1^{+0}_{-1}	1
poloidal (*l*≥4)	20^{+3}_{-4}	20	$45\ ^{+0}_{-10}$	48
toroidal (*l*=1)	34^{+6}_{-1}	32	$6\ ^{+1}_{-0}$	3
toroidal (*l*=2)	4^{+1}_{-1}	4	$2\ ^{+0}_{-1}$	2
toroidal (*l*=3)	2^{+1}_{-3}	2	$0\ ^{+3}_{-0}$	2
toroidal (*l* ≥4)	17^{+12}_{-1}	13	40^{+1}_{-6}	40
axisymetry poloidal	11^{+2}_{-2}	12	$19\ ^{+3}_{-4}$	19
axisymetry toroidal	49^{+1}_{-2}	45	$36\ ^{+10}_{-6}$	27

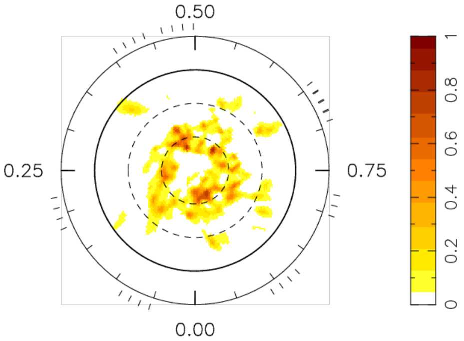

(a) HIP 71933 Epoch 2009.26 best rotation period

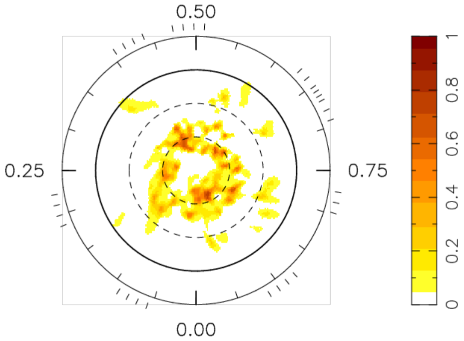

(b) HIP 71933 Epoch 2009.26 TESS rotation period

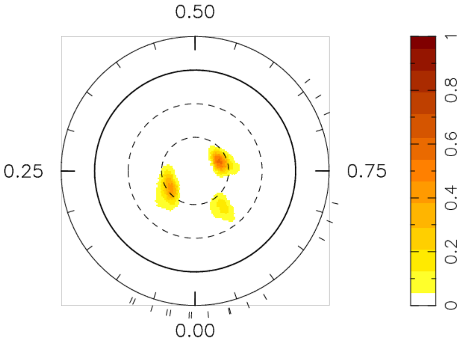

(c) HIP 71933 Epoch 2009.34 best rotation period

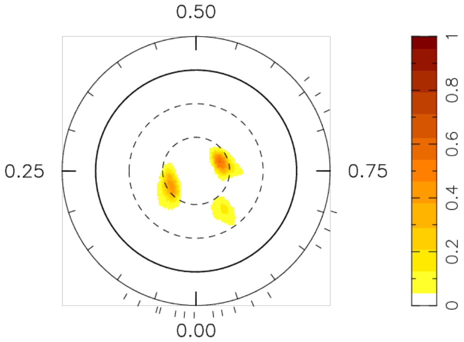

(d) HIP 71933 Epoch 2009.34 TESS rotation period

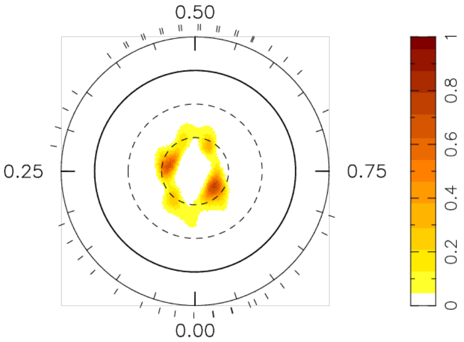

(e) HIP 71933 Epoch 2010.33 best rotation period

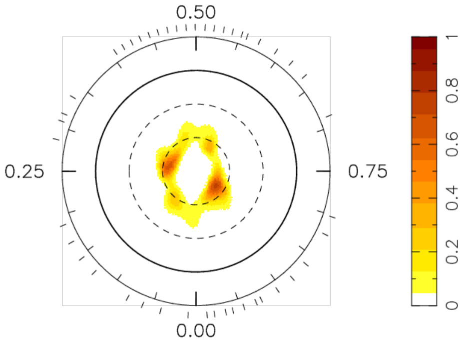

(f) HIP 71933 Epoch 2010.33 TESS rotation period

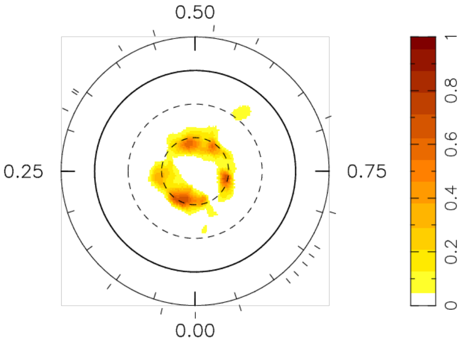

(g) HIP 71933 Epoch 2011.37 best rotation period

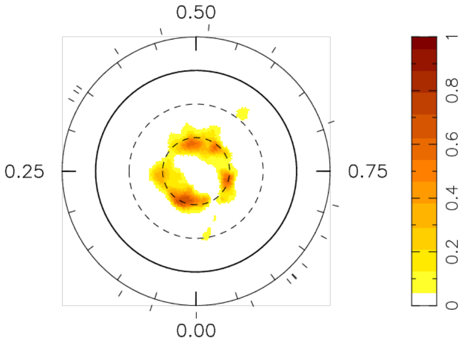

(h) HIP 71933 Epoch 2011.37 TESS rotation period

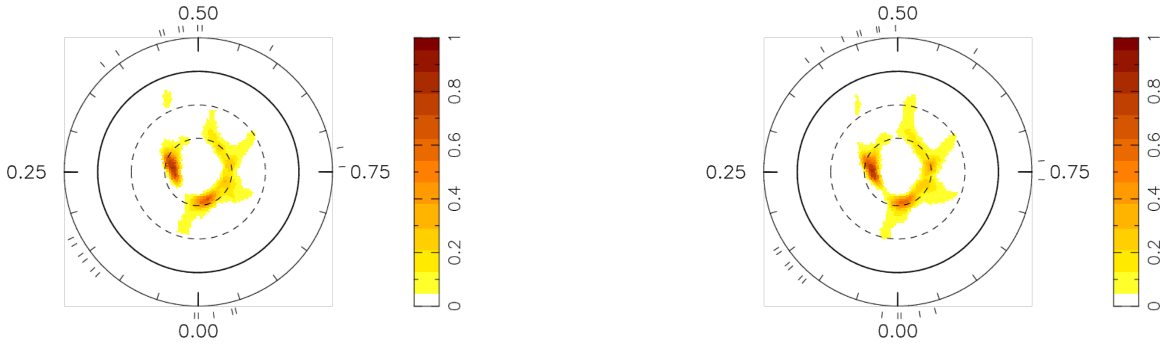

(i) HIP 71933 Epoch 2012.26 best rotation period (j) HIP 71933 Epoch 2011.37 TESS rotation period

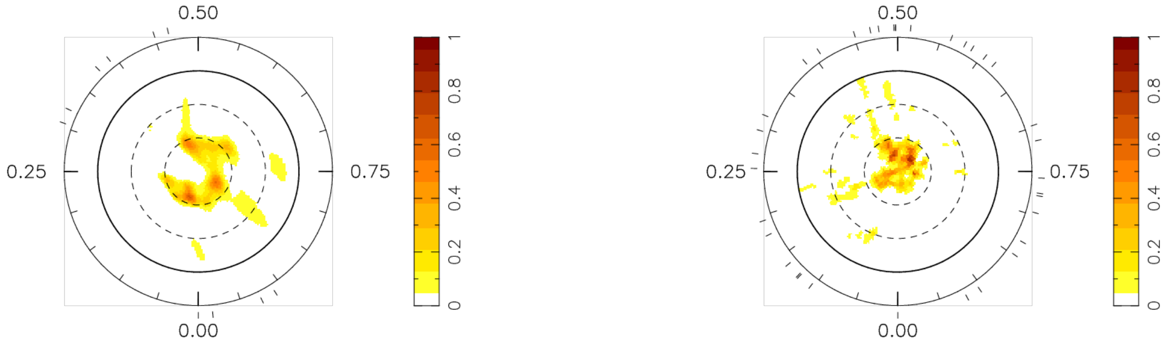

(k) HIP 71933 Epoch 2018.07 best rotation period (l) HIP 71933 Epoch 2018.07 TESS rotation period

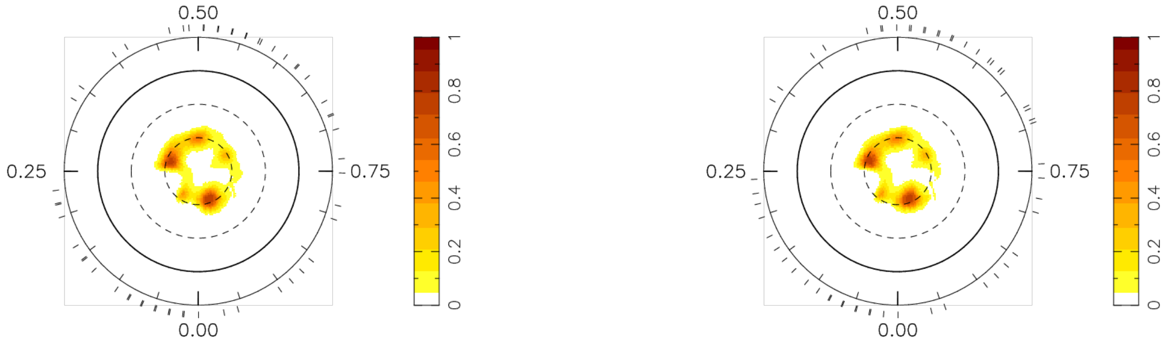

(m) HIP 71933 Epoch 2019.46 best rotation period (n) HIP 71933 Epoch 2019.46 TESS rotation period

Figure D.0.4: HIP 71933 brightness maps for seven Epochs 2009.26, 2009.34, 2010.33, 2011,37, 2012.26, 2018.07, and 2019.46. Brightness maps from original best fit rotation period side by side with the rotation period derived from the TESS photometric observations. The maps on the left are duplicates of maps in Figure 4.4.3 and remain the best statistical fit. The DI derived rotation rate from this study is a close match to the rotation period observed from the TESS photometry, making the graphs from each epoch nearly identical.

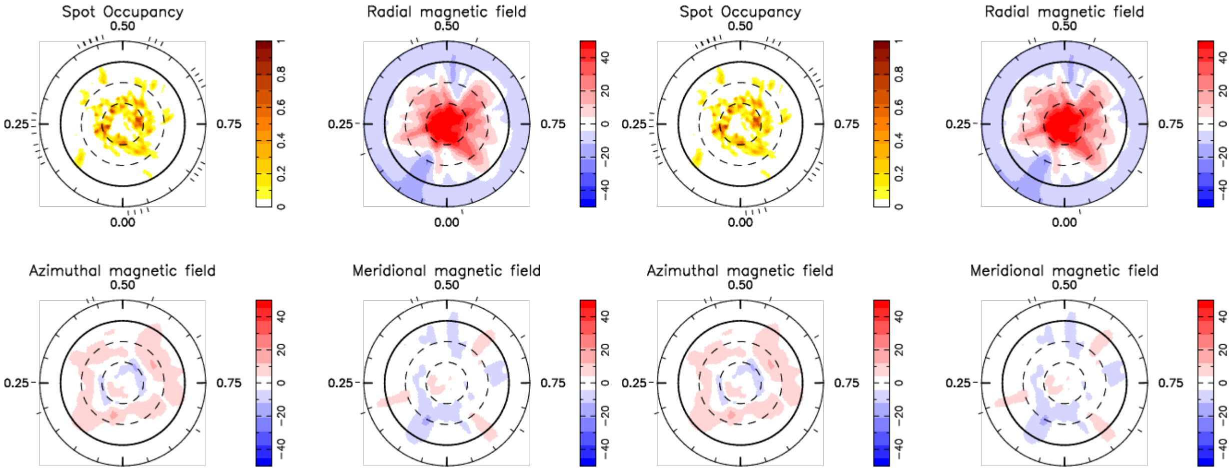

(a) HIP 71933 Epoch 2009.26 best rotation period (b) HIP 71933 Epoch 2009.26 TESS rotation period

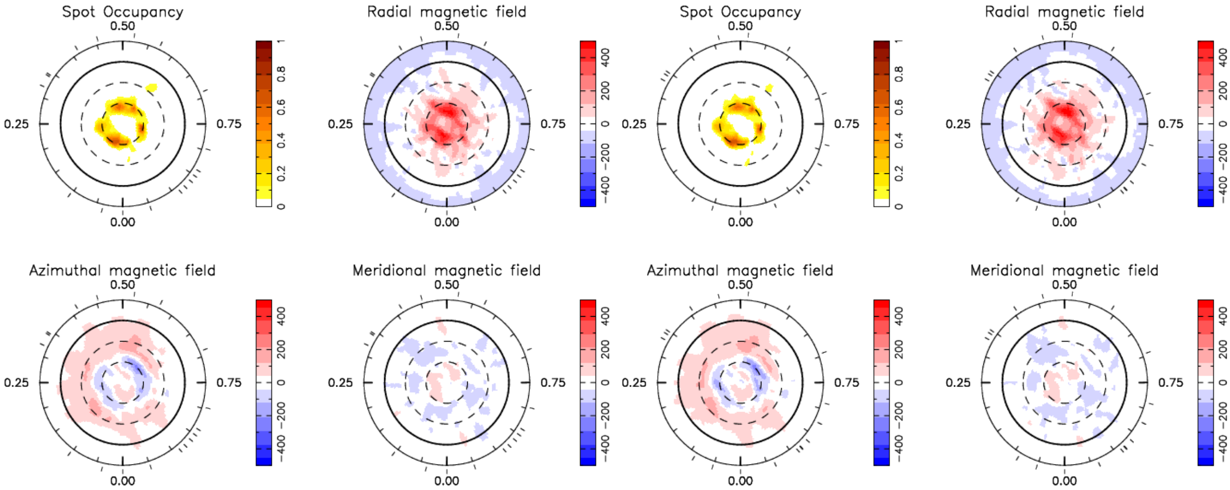

(c) HIP 71933 Epoch 2009.26 best rotation period (d) HIP 71933 Epoch 2011.37 TESS rotation period

Figure D.0.5: HIP 71933 magnetic maps for Epochs 2009.26 and 2011.37, original best fit rotation period side by side with the rotation period derived from the TESS photometric observations. The maps on the left are duplicates of maps in Figures 4.4.4 and 4.4.5 and are the best statistical fits for both epochs. As seen in Figure D.0.4 there is very little difference between the maps from the original rotation rate and the TESS rotation rate because the values are nearly identical.

Table D.0.2: Magnetic quantities for HIP 71933 derived from maps in Figure 4.4.4 and Figure 4.4.5 placed next to values derived from the TESS rotation rates used to make Figure D.0.5. This table is modified from Table 4.4.3. Magnetic quantities calculated using TESS rotation rates are in columns 3 and 5. These values do not differ significantly from the values using the best fit rotation rates as expected because those values were very close. We continue to see a prodominantly poloidal field configuration with the majority of the energy in the lower shells. Variations for the TESS rotation were not calculated.

Quantity	Epoch 2009.26 original rotation (percent energy)	Epoch 2009.26 TESS rotation (percent energy)	Epoch 2011.37 original rotation (percent energy)	Epoch 2011.37 TESS rotation (percent energy)
Total poloidal	94^{+1}_{-0}	95	83^{+2}_{-0}	80
Total toroidal	6^{+0}_{-1}	5	17^{+3}_{-1}	20
poloidal (l=1)	62^{+2}_{-2}	65	50^{+5}_{-5}	45
poloidal (l=2)	14^{+2}_{-1}	12	12^{+1}_{-1}	12
poloidal (l=3)	7^{+1}_{-0}	5	5^{+1}_{-1}	5
poloidal (l≥4)	12^{+1}_{-1}	16	$14\ ^{+2}_{-2}$	16
toroidal (l=1)	2^{+0}_{-0}	2	$5\ ^{+1}_{-1}$	6
toroidal (l=2)	1^{+0}_{-0}	1	$2\ ^{+1}_{-0}$	2
toroidal (l=3)	0^{+0}_{-0}	0	$1\ ^{+1}_{-0}$	1
toroidal (l ≥4)	3^{+0}_{-0}	2	10^{+2}_{-2}	11
axisymetry poloidal	82^{+3}_{-1}	85	$74\ ^{+3}_{-1}$	71
axisymetry toroidal	5^{+0}_{-1}	4	$16\ ^{+2}_{-2}$	17

E LIST OF PUBLICATIONS

These articles were published during the course of my candidature of which I have had authorship.

1. Perugini, G.M.; Marsden, S.C.; Waite, I.A.; Jeffers, S.V.; Piskunov, N. ; Burton, D.M.; Mengel, M.W.; Hughes, J.E.; Hébrard, E.M.; 2021; *Evolution of brightness and magnetic features of young solar-type stars - I. The young G star HIP 89829,* MNRAS, 508, 3304, published September 29, 2021.

2. Hughes, J.E.; Marsden, S.C.; Carter, B.D.; Waite, I.A.; Burton, D.M.; Perugini, G.M.; Hébrard, E.M. ; 2023; *Evolution of brightness and magnetic features of young solar-type stars - II. The young F8 star HIP 71933,* MNRAS, 524, 1757, published March 13, 2023 (This paper covers the results shown in Section 4).

References

Aigrain S., et al., 2012, MNRAS, 419, 3147

Alvarado-Gómez J., et al., 2015, A&A, 582, A38

Ammler-von Eiff M., Reiners A., 2012, A&A, 542, A116

Arlt R., et al., 2016, A&A, 595, A104

Babcock H., 1961, AAS, 133, 572

Babcock H. W., et al., 1955, AAS, 121, 349

Bahcall J. N., Davis R. R., 2000, PASP, 112, 429

Baliunas S., et al., 1995, ApJ, 438, 269

Baraffe I., et al., 2015, A&A, 577, A42

Barnes J., et al., 1998, MNRAS, 299, 904

Barnes J., et al., 2005, MNRAS, 357, L1

Baron D., 2019, arXiv:1904.07248v1

Barrado D., et al., 2001, Astrophys. J. Suppl. Ser. 134, 103 (2001)

Bazot M., et al., 2018, A&A, 619, L9

Beer R., et al., 1972, ApJ, 172, 89

Berdyugina S. V., 1998, A&A, 338, 97

Berdyugina S., 2005, Living Rev. Sol. Phys., 2, 8

Bethe H., 1939, Phys. Rev., 55, 434

Bhalotia V., et al.,, A New Astroseismic Kepler Benchmark Constrains the Onset of Weakened Magnetic Braking in Mature Sun-Like Stars

Böhm-Vitense E., 1992, Introduction to stellar astrophysics Volume 3 Stellar structure and evolution. Cambridge University Press, Cambridge

Boro Saikia S., et al., 2015, A&A, 573, A17

Boro Saikia S., et al., 2022, A&A, 658, A16

Borra E., et al., 1984, ApJ, 284, 211

Borsa F., et al., 2015, A&A, 578, A64

Brandenburg A., 2005, ApJ, 625, 539

Brandenburg A., et al., 1989, A&A, 213, 411

Breton S., et al., 2020, SF2A, 2022, 206

Brown S., et al., 1991, A&A, 250, 463

Brown B. P., et al., 2010, ApJ, 711, 424

Brown E., et al., 2021, MNRAS, 501, 3981

Brown E., et al., 2024, MNRAS, 528, 4092

Budding E., et al., 2002, Commisions 27 and 42 of the IAU Information Bulletin on Variable Stars, 5451

Burton D. M., 2013, PhD thesis, University of Southern Queensland

Cameron P. B., et al., 2015, MNRAS, 454, 593

Cang T.-Q., et al., 2020, A&A, 643, A39

Carrington R., 2021, Observations of the Spots on the Sun From November 9, 1853, to March 24, 1861, Made at Redhill ... LEGARE STREET Press, https://books.google.com/books?id=qIevzgEACAAJ

Carter B., et al., 1996, Astron. Soc. Aust., 13, 150

Carter B., et al., 2015, 18th Cambridge Workshop on Cool Stars, Stellar Systems and the Sun, Proceedings of the conference held at Lowell Observatory, 8-14 June, 2014, pp 209–216

Casas R., Vaquero J., 2014, solphys, 16, 56

Catalano S., et al., 2002, A&A, 394, 1009

Charbonneau P., 2005, Living Rev. Sol. Phys, 2, 1

Charbonneau P., 2014, Ann. Rev. Astron. Astropys., 52, 251

Choudhuri A. R., 2017, Astron.Nachr., 60

Cowling T., 1945, MNRAS, 105, 166

Cox M. A., Rosales-Guzmán 2023, Applied Optics, 62, 7828

Cutispoto G., et al., 2003, A&A, 400, 659

Desch S., Mouschovias T. C., 2001, ApJ, 550, 314

Desidera S., et al., 2015, A&A, 573A, 126

Distefano E., et al., 2016, A&A, 591, A43

Donat J. F., et al., 2003, MNRAS, 345, 1187

Donati J.-F., Brown S., 1997, A&A, 326, 1135

Donati J. F., Cameron A. C., 1997, MNRAS, 291, 1

Donati J., et al., 1992, A&A, 265, 669

Donati J.-F., et al., 1997, MNRAS, 291, 658

Donati J.-F., et al., 1999, MNRAS, 302, 437

Donati J.-F., et al., 2000b, MNRAS, 316, 699

Donati J. F., et al., 2000a, MNRAS, 316, 699

Donati J.-F., et al., 2003, MNRAS, 345, 1145

Donati J.-F., et al., 2006, MNRAS, 370, 629

Dudorov A. E., Khaibrakhmanov S. A., 2015, Adv. Space Res., 55, 843

Dumusque X., et al., 2014, ApJ, 789, 154

Duncan D. K., et al., 1991, ApJ, 76, 383

Eddintgon A., 1920, Nature, 106, 14

Einstein A., 1921, The Meaning of Relativity. Princeton University Press, Princeton, NJ

Erdélyi R., Ballai I., 2007, Astron. Nachr., 328, 726

Espenak F., 1999, NASA Astronomical Ephemeris Data, `https://eclipse.gsfc.nasa.gov/TYPE/ephemeris.html`

FOSCO 2024, Poincaré Sphere, `https://www.fiberoptics4sale.com/blogs/wave-optics/104501958-poincare-sphere`

Frölich H. D., et al., 2012, A&A, 543, A146

GONG 2023, National Solar Observator, Global Oscillation Network Group, `https://gons.nso.edu`

Gaia et al., 2016, Gaia Collaboration et al., Description of the Gaia mission, spacecraft, instruments, survey and measurement principles and operations.

Gaia et al., 2018, Gaia Collaboration et al., Summary of Gaia contents and survey properties.

Gaia et al., 2020, Gaia Collaboration et.al, Summary of Gaia contents and survey properties

Gaia et al., 2022, Gaia Collaboration et.al, Summary of Gaia contents and survey properties

Glassmeier K.-H., et al., 2009, International Journal of Astrobiology, 8, 147

Gontcharov G. A., 2016, Astron. Lett., 32, 759

Gough D., et al., 1996, Science, 272, 1296

Granzer T., et al., 2000, A&A, 355, 1087

Grevesse N., et al., 1984, A&A, 141, 10

Hackman T., et al., 2013, A&A, 553, A40

Hackman T., et al., 2016, A&A, 587, A28

Hackman T., et al., 2024, From convective stellar dynamo simulations to Zeeman-Doppler images, Astronomy and Astrophysics preprint June 2023

Hale G. E., 1908, ApJ, 28, 315

Hall D. B., 1973, An atlas of infrared spectra of the solar photosphere and of sunspot umbrae, in the spectral intervals 4040 cm; 5095 cm; 6700 cm; 7400 cm; 8790 cm. Kitt Peak National Observatory

Hathaway D. H., 2014, The Solar Dynamo, `https://solarscience.msfc.nasa.gov/dynamo.shmtl`

Hathaway D. H., 2022, Solar Physics: The Solar Interior, `https://solarscience.msfc,.nasa.gov/interior.shtml`

Hathaway D., 2024, Solar Cycle Science Discover the Sun, `https://solarcyclescience.com/solarcycle.html`

Haxton W., 2008, PASP, 25, 44

Hendry P. D., Mochnacki S. W., 2000, ApJ, 531:, 467

Herbrick M., Kokkotas K., 2017, MNRAS, 466, 1330

Hirshfeld A., et al., 2000, Sky Catalogue 2000.0 Volume 1 (Sky Catalogue 2000 2nd-ED). Cambridge University Press, Cambridge

Holmgren J., Davis R., 1959, PhRv, 113, 1556

Holzwarth V., 2004, Astron. Nachr., 325, 408

Holzwarth V., Schüssler M., 2002, Astron. Nachr, 323, 399

Hotelling H., 1933, Journal of Educational Psychology, 24, 417

Howe R., 2020, pp 63–74

Hughes J., et al., 2023, MNRAS, 524, 1757

Isik E., et al., 2018, A&A, 620, A177

Järvinen S., et al., 2005, A&A, 440, 735

Järvinen S., et al., 2008, A&A, 488, 1047

Järvinen S., et al., 2015, A&A, 574, A25

Järvinen S., et al., 2018, A&A, 620, A162

Jeffers S., Donati J. F., 2011.

Jeffers S., et al., 2018, MNRAS, 479, 5266

Jetsu L., 2018, MNRAS, arXiv:1808.02221

Jetsu L., et al., 1993, A&A, 282, L9

Katoh N., et al., 2018, Publ. Astron. Soc. Japan, 60, 1

Kochukhov O., et al., 2010, A&A, 524, A5

Kochukhov O., et al., 2020, A&A, 635, A142

Korhonen H., Järvinen S. P., 2006, Binary Stars as Critical Tools and Tests in Contemporary Astrophysics, Proceedings IAU Symposium No. 240

Kriskovics L., et al., 2019, A&A, 627, A52

Küker M., Rüdiger 2005, Astron.Nachr., 326, 265

Küker M., Rüdiger 2007, Astron. Nachr., 328, 1050

Küker M., Rüdiger G., 2008, Journal of Physics: Conference Series, 118

Küker M., et al., 2011, A&A, 530, A48

Kunz M. W., Mouschovias T. C., 2010, MNRAS, 408, 322

Kürster M., et al., 1994, A&A, 289, 899

Kurucz R. L., Bell B., 1995, Atomic Line Data, ATLAS9 Stellar Atmosphere Programs, `https://lweb.cfa.harvard.edu/amp/ampdata/kurucz23/sekur.html`

Landstreet J. D., 1991, in Tuominen I., Moss D., Rüdiger G., eds, The Sun and Cool Stars: activity, magnetism, dynamos. Springer Berlin Heidelberg, Berlin, Heidelberg, pp 342–346

Lavail A., et al., 2020, MNRAS, 497, 632

Le Cunnf A.-L., 2004, The occam's razor fallacy: the simplest solution is not always the correct one, `https://nesslabs.com/occams-razor`

Lehmann L., Donati J.-F., 2022, MNRAS, 514, 2333

Lehmann H., et al., 2020, A&A, 644, A121

Lehtinen J., et al., 2019, A&A, 660, A41

Leighton R. W., 1969, AAS, 156, 1

Leighton R. B., et al., 1961, AAS, 135, 474

Li P., et al., 2024, na, 111

Lightkurve Collaboration et al., 2018, Lightkurve: Kepler and TESS time series analysis in Python, Astrophysics Source Code Library (ascl:1812.013)

Marsden S. C., et al., 2005, MNRAS, 359

Marsden S. C., et al., 2006a, Solar Polarization 4 ASP Conference Series, 358, 401

Marsden S., et al., 2006b, MNRAS, 370, 468

Marsden S., et al., 2011a, MNRAS, 413, 1922

Marsden S., et al., 2011b, MNRAS, 413, 1939

Marsden S., et al., 2021, SF2A-2021 Proceedings of the Annual meeting of the French Society of Astronomy and Astrophysics, pp 284–287

Marsden S., et al., 2023, MNRAS, 522, 792

Marsh T., Horne K., 1988, MNRAS, 235, 269

McDonald I., et al., 2012, MNRAS, 427, 343

Mengel M., 2005, Master's thesis, University of Southern Queensland, https://eprints.usq.edu.au/1474/

Mengel M., 2014b, Doppler Imaging Handbook

Mengel M., 2014a, Using ESpRIT Producing LSD Stokes I and Stokes V Profiles

Mengel M., et al., 2016, MNRAS, 459, 4325

Messina S., Guinan E., 2003, The Future of Cool-Star Astrophysics: 12th Cambridge Workshop on Cool Stars, Stellar Systems and the Sun, pp 941–945

Mestel L., 2012, Steller Magnetism. Oxford University Press

Mizusawa T. F., et al., 2012, ApJ, 144, 135

Montes D., et al., 2001, MNRAS, 328, 45

Moss D., et al., 1995, A&A, 294, 155

Moutou C., et al., 2017, MNRAS, 472, 4563

Munoz-Jaramillo A., et al., 2008, The Solar Dynamo: Toroidal and Poloidal Magnetic Fields, https://svs.gsfc.nasa.gov/cgi-bin/details.cgi?aid=3521

NASA 2012, Layers of the Sun, https://www.nasa.gov/image-article/layers-of-sun

NASA 2013a, Our Sun: Facts, https://www.nasa.gov/sun/facts/

NASA 2013b, The Sun, https://www.nasa.gov/image-article/sun/

NASA 2020b, Lesson: Differential Rotation of the Sun, https:///soho.nascom.nasa.gov/explore/lessons/diffrot9_12.html

NASA 2020a, SOHO Solar and Heliospheric Observatory, https://science.nasa.gov/mission/soho

NCAR H. A. O., 2023, Thomas Harriot, https://www2.hao.ucar.edu/education/scientists/thomas-harriot-1560-1621

NOAA 2024, Current Space Weather Conditions, https://www.swpc.noaa.gov/phenomena/sunspotssolar-cycle

NSO 2023, Mount Wilson Observatory HK Project - NSO, nso.edu/data/historical-data/mount-wilson-observatory-hk-project

NWRA 2024, https://www.cora.nwra.com/~werne/eos/text/dynamo.html

NWS 2024, https://www.weather.gov/news/201509-solar-cycle

Noraz Q., et al., 2024, A&A, 684, A156

O'Neal D., Neff J. E., 1997, Astron. J., 113, 3

O'Neal D., et al., 2001, ApJ, 122, 1954

Ossendrijver M., 2003, 11, 287

Özdarcan O., et al., 2016, A&A, 593, A123

Parker E. N., 1955, ApJ, 122, 293

Parker E., 1993, ApJ, 408, 707

Payne C., 1925, Harvard Observatory Monographs

Pearson K., 1901, The London, Edinburge, and Dublin Philosophical Magazine and Journal of Science, 2:11, 559

Peat C., 2022, Heavens Above, https://heavens-above.com

Perkowitz S., 2022, Phys. World

Perryman M., 2018, Cambridge Univ. Press

Perugini G. M., et al., 2021, MNRAS, 508, 3304

Petit P., et al., 2002, MNRAS, 334, 374

Petit P., et al., 2008, MNRAS, 388, 80

Piskunov N., et al., 2011, The Messenger, 143, 7

Poppenhaeger K., et al., 2014, A&A, 565, L1

Pourbaix D., et al., 2018, A&A, aa1213

Ragulskaya M., 2018, Solar Terrestrial Physics - The Current State and Prospects, 2, 202

Randich S., et al., 2001, A&A, 372, 862

Reiners A., 2006, A&A, 446, 267

Reiners A., Schmitt J., 2003, A&A, 412, 813

Rice J., 2002, Astron. Nachr., 323, 220

Rósen L., 2016, PhD thesis, Uppsala Universitet

STSCI 2024, TESS Aperture Photometry, `https://https://mast.stsci.edu/portal/Mashup/Clients/Mast/Portal.html`

Saar S. H., Donahue R. A., 1997, ApJ, 485, 319

Sanchis-Ojeda R., Winn J. N., 2011, A&A, 743, 61

Sanderson T., et al., 2003, J.Geophys.Res., 108, 1035

Santos N., et al., 2000, 361, 265

Santos N., et al., 2014, A&A, 566, A35

Savanov I., et al., 2019, Contrib. Astron. Obs Skalnaté Pleso, 49, 415

Scheinero R. C.-P., 1651, E-RARA

Schrijver C. J., Title A. M., 2001, ApJ, 551, 1099

Schüssler M., et al., 1996, A&A, 314, 503

Schüussler M., Solanki S., 1992, A&A, 264, L13

Seach J., et al., 2020, MNRAS, 494, 5683

Seach J., et al., 2022, MNRAS, 513, 4278

See V., et al., 2019, ApJ, 876, 118

Semel M., 1989, A&A, 225, 456

Semel M., et al., 1993, A&A, 278, 231

Semel M., et al., 2006, ASP Conference Series Solar Polarization 4, 358, 355

Senavci H., et al., 2021, MNRAS, 502, 3343

Simon T., Landsman W., 1991, ApJ, 380, 200

Skilling J., Bryan R. K., 1984, MNRAS, 211, 111

Snodgrass H. B., 1987, solphys, 110, 35

Soderblom D. R., King J. R., 1997, Solar-Type Stars: Basic Information on Their Classification and Characterization, https://ftp.lowell.edu/www_users/jch/workshop/drs/drs-pl.html

Solanki S., Unruh Y., 2004, MNRAS, 348, 307

Strassmeier K., Bartus J., 2000, Astron. Astrophys, 354, 537

Strassmeier K., Rice D., 1998, A&A, 330, 685

Strassmeier K., et al., 2000, A&A, 142, 273

Strassmeier K., et al., 2003, A&A, 411, 585

TSSC 2024, TESS Aperture Photometry, https://heasarc.gsfc.nasa.gov/docs/tess/Aperture-Photometry-Tutorial.html

Takeda G., et al., 2007, Astrophys. J. Suppl. Ser., 168, 297

Tang S.-Y., et al., 2024, Measuring the Spot Variability of T Tauri Stars Using Near-IR Atomic Fe and Molecular OH Lines, preprint

Temple R. K., 1988, The UNESCO Courier, October, 1988

Terebizh V. Y., Biryukov V., 1994, Astronomical & Astrophysical Transactions, 6, 37

ThorLabs 2020, Using the Poincare Sphere to Represent the Polarization State, https://www.thorlabs.com/newgrouppage9.cfm?objectgroup_id=14200

Torres C. A. O., et al., 2006, A&A, 460, 695

Ulrich R. K., 1970, ApJ, 162, 993

Vasil Geoffrey M., et al., 2024, Nature, 629, 769

Vilela C., et al., 2014, Proceedings of the International Astronomical Union, 302, 347

Vogt S. S., Penrod D., 1983, PASP, 95, 565

Vogt S. S., et al., 1987, ApJ, 321, 496

Waite I., 2013, PhD thesis, University of Southern Queensland

Waite I., et al., 2011, MNRAS, 413, 1949

Waite I., et al., 2015, MNRAS, 449, 8

Waite I., et al., 2017, MNRAS, 465, 2076

Wang Y.-M., 2005, Sol. Phys., 224, 21

Wang K., et al., 2015, ApJ, 805, 22

Willamo T., et al., 2019, A&A, 622, A170

Willamo T., et al., 2022, A&A, 659, A71

Wilson O., 1966, ApJ, 144, 695

Wilson O., 1978, ApJ, 226, 379

Wolff S., Simon T., 1997, PASP, 109, 759

WorldAtlas 2020, What Are the Layers of the Sun, https://www.worldatlas.com/articles/what-are-the-layers-of-the-sun.html

Yamashita M., et al., 2022, Publ. Astron. Soc. Japan (2022), 74, 1295

Zeeman P., 1897, Philosophical Magazine, 43, 226

Zuckerman B., et al., 2011, ApJ, 732, 61

Zuniga-Fernandez S., et al., 2021, A&A, 645A, 30

de Strobel G. C., 1996, Astron. Astrophys Rev, 243, 243